INFORMATION TO USERS

This manuscript has been reproduced from the microfilm master. UMI films the text directly from the original or copy submitted. Thus, some thesis and dissertation copies are in typewriter face, while others may be from any type of computer printer.

The quality of this reproduction is dependent upon the quality of the copy submitted. Broken or indistinct print, colored or poor quality illustrations and photographs, print bleedthrough, substandard margins, and improper alignment can adversely affect reproduction.

In the unlikely event that the author did not send UMI a complete manuscript and there are missing pages, these will be noted. Also, if unauthorized copyright material had to be removed, a note will indicate the deletion.

Oversize materials (e.g., maps, drawings, charts) are reproduced by sectioning the original, beginning at the upper left-hand corner and continuing from left to right in equal sections with small overlaps.

Photographs included in the original manuscript have been reproduced xerographically in this copy. Higher quality 6" x 9" black and white photographic prints are available for any photographs or illustrations appearing in this copy for an additional charge. Contact UMI directly to order.

ProQuest Information and Learning
300 North Zeeb Road, Ann Arbor, MI 48106-1346 USA
800-521-0600

A

Viscous Resuspension and Particle Segregation in Concentrated Suspensions Undergoing Shear

by

Mahesh Tirumkudulu

A Dissertation Submitted to the Graduate Faculty in Engineering in Partial Fulfillment of the Requirements for the Degree of Doctor of Philosophy

The City University of New York

2001

UMI Number: 3008876

Bell & Howell Information and Learning Company
300 North Zeeb Road
P.O. Box 1346
Ann Arbor, MI 48106-1346

This manuscript has been read and accepted for the Graduate Faculty in Engineering in satisfaction of the dissertation requirement for the degree of the Doctor of Philosophy.

2/8/01 — Date

Chairman of Examining Committee

2/8/01 — Date

Executive Officer

Prof. Andreas Acrivos(Mentor)

Prof. Sheldon Weinbaum

Prof. Joel Koplik

Prof. Charles Maldarelli

Prof. Boris Khusid

Supervisory Committee

THE CITY UNIVERSITY OF NEW YORK

Abstract

Viscous Resuspension and Particle Segregation in Concentrated Suspensions Undergoing Shear

by

Mahesh Tirumkudulu

Advisor: Professor Andreas Acrivos

This thesis describes the experimental and theoretical investigation of three different problems, two of which involve the flow of concentrated suspensions undergoing shear and the third relates to rimming flows of viscous particle-free liquids within a partially filled rotating horizontal cylinder. The first deals with the viscous re-suspension of heavy particles in a varying shear flow field, where the particles, although heavier than the suspending fluid, are re-suspended due to the action of shear induced migration. Here, under fully developed flow conditions, we measured the resuspension height, the cup-mixing particle concentration and the velocity profiles across the pipe's cross section. These results were then compared to those computed using a theoretical model based on the theory of shear induced migration (Leighton & Acrivos [1]), as done by Zhang & Acrivos ([2]). Although qualitatively in agreement, quantitative differences were found between the experimental results and the model predictions. The second problem deals with a curious and as yet unexplained phenomenon of particle segregation into regions of high and low concentration in a neutrally buoyant suspension undergoing shear in the presence of a free surface.

Here experiments were performed in two different geometries, viz. a partially filled horizontal Couette device and a partially filled rotating horizontal cylinder. Although it seems likely that the particle segregation phenomenon observed in both the geometries is initiated by particle concentration fluctuations which, in turn, lead to fluctuations in the effective viscosity of the suspension, we have been unable to provide a quantitative explanation for this observation. Finally, the particle segregation experiments motivated us to investigate theoretically the flow of a viscous particle-free liquid in a partially filled rotating horizontal cylinder. We found that, under creeping flow conditions, the addition of the hydrostatic pressure term to the standard lubrication equation leads to film thickness profiles which, over a broad range of parameters, are in close agreement with those obtained experimentally, as well as via the solution to the full Stokes equations.

Preface

This thesis describes the experimental and theoretical investigation of three different problems, two of which involve the flow of concentrated suspensions undergoing shear and the third relates to rimming flows of viscous particle-free liquids within a partially filled rotating horizontal cylinder.

In chapter 1, we study the viscous re-suspension of heavy particles in fully developed laminar flows in a horizontal pipe. Here, we measured the cup-mixing particle concentration, the re-suspension height and, using the technique of Laser Doppler Anemometry, the velocity profile of the suspension across the pipe's cross section. The experimental results were then compared with those computed using a theoretical model based on the theory of shear-induced migration. Although the axial velocity profiles were found to be in good agreement with the model calculations, this was not the case, in general, with the cup-mixing concentration and with the re-suspension height.

The second problem involving particle segregation was first studied experimentally with a neutrally buoyant suspension sheared in a partially filled horizontal Couette device. Here, we identified a new instability in the Couette device where the presence of particles not only alters the fluid dynamics of the system but also leads to a segregation of particles into regions of high and low concentrations all along the length of the Couette device. To further our understanding of this phenomenon, we then performed similar experiments with the neutrally buoyant suspension in a different but a simpler geometry, viz. a partially filled rotating horizontal cylinder (also referred to as rimming flows). Interestingly, we found that in a certain parameter regime the segregation resulted in the formation of high concentration regions interspersed with regions that were completely devoid of particles. These

experimental results motivated us to consider theoretically, the flow within a rotating horizontal cylinder containing a particle-free and very viscous liquid which completely coats the cylinder. We first present in chapter 2, the lubrication problem in the horizontal rotating cylinder where we found that, under creeping flow conditions, the addition of the hydrostatic pressure term to the standard lubrication equation leads to film thickness profiles which, over a broad range of parameters, are in close agreement with those obtained experimentally, as well as via the solution to the full Stokes equations. Here, the experiments were performed in the parameter regime where the fluid flow is everywhere essentially steady and two-dimensional. Next in chapter 3, we describe the results of two sets of experiments performed with, respectively, a particle-free viscous liquid and a neutrally buoyant suspension in the partially filled rotating horizontal cylinder. These experiments, contrary to those reported in chapter 2, were conducted over a broad range of parameters which also included flow states that were unsteady and three-dimensional. We found that in the range of parameter space where the flow of the particle-free liquid was steady and two dimensional, the initially uniform suspension divided into cylindrical bands of high particle concentration separated by regions of essentially particle-free liquid. We also performed experiments to identify the important dimensionless variables affecting the particle segregation phenomenon by systematically varying one of the variables while keeping the rest constant. Finally, in chapter 4, we describe similar results for experiments performed in the partially filled horizontal Couette device. In these latter experiments, which were mostly qualitative, we varied the total particle concentration, the fill level and the rotation rate of the inner cylinder and studied their effect on the particle segregation phenomenon.

Acknowledgement

I would like to express my deepest gratitude to Professor Andreas Acrivos for being a wonderful mentor during the course of my Ph.D. His deep insight into research problems and his single-minded dedication to research will always be a great source of inspiration to me.

I acknowledge the unfailing love, affection and support of my parents, T. R. Subramaniyam and Shantha Subramaniyam. I dedicate this work to them.

I am greatly indebt to Swami Tathagatananda of Vedanta Society of New York for accomodating me at the society. I feel extremely fortunate to have known him. His purity, integrity and large-heartedness will always to be remembered.

During my Ph.D work, I received many valuable suggestions from Dr. Anubhav Tripathi and I am thankful to him.

I would specially like to acknowledge the help that I continuously received from Andy Eng of Chemical Engineering department. I will never be able to forget his goodness and charitable nature. I am also thankful to Mr. Xu, also of Chemical Engineering department, for fabricating many of my experimental set-ups.

Finally, there are many friends who have helped me in many ways. They are : Preeti Lodha, Ravichandra Palaparthi, Nitin Kumar, Chandra Shekar, John Schlenk, Bill Conrad, Richard Murphy, Dora Barbera, Barbara, Jean Brady, Dr. Zhiyong Qiu, Nikolai Markarian, Professor Boris Khusid and many others whose names I cannot recollect.

Contents

List of Tables

List of Figures

Chapter 1

Viscous resuspension of heavy particles in a pressure driven pipe flow: Experiments and Computations

Abstract

Viscous resuspension of heavy particles in fully developed laminar flows in a horizontal pipe was investigated experimentally for various initial particle concentrations and flow rates. The fully developed velocity profiles of the suspension across the pipe's cross section were obtained using the technique of Laser Doppler Anemometry. Also measured were the resuspension height, the pressure drop and the cup mixing particle concentration. These results were then compared to those computed using a theoretical model based on the theory of shear induced migration (Leighton & Acrivos [1]), as done by Zhang & Acrivos ([2]). The resulting mathematical system of equations was solved using finite-element techniques. Although qualitatively in agreement, quantitative differences were found to exist between the experimental results and the model predictions.

1.1 Introduction

It was first pointed out by Eckstein, Bailey and Shapiro([3]) that, in concentrated suspensions undergoing shear, the fluid-mechanical interactions among neighboring particles generate irregular motions akin to a random walk even under conditions of vanishingly small Reynolds number. An important consequence of this irregular particle motion is that it gives rise to a net particle flux from regions of high particle concentration to low and from regions of high shear rates to low (Leighton & Acrivos[1]). This phenomenon, termed shear-induced diffusion, often creates a non-uniform particle distribution in flowing suspensions that were initially well mixed even in Stokes flow. This fact has important implications in the field of viscometry where the interpretation of effective viscosity measurements in concentrated suspensions is subject to serious errors if the shear-induced non-uniformity in the particle concentration within the measuring device is not properly taken in to account. It is also an important factor in many industrial processes of material manufacturing where the performance of the finished product is greatly affected by the degree of solids dispersivity([4]). In addition, shear-induced particle diffusion is responsible for the observed phenomenon of viscous resuspension wherein, under the action of shear, an initially settled bed of particles in contact with a clear fluid above it can be resuspended and the particles kept in suspension even under laminar flow conditions.

In the past, both experiments and theoretical modelling of concentrated suspensions containing neutrally buoyant as well as heavy particles have been performed primarily for unidirectional or quasi-unidirectional flows. The experiments were conducted for a Couette flow ([5],[6]), a channel flow ([7],[8]) and for flow down an inclined plate ([9]). On the theoretical front, Leighton & Acrivos[1] followed by, Phillips et al[10], proposed constitutive equations on the assumption that the suspension could be viewed as a single continuum and that the migration of the particles

in the sheared suspension could be represented by particle fluxes that were proportional to the gradients of the particle concentration and the local shear rate, and in the case of heavy particles, also to the sedimentation velocity. Nott & Brady[11] proposed an alternative approach called the suspension balance model, which differs from the shear-induced particle migration model (also referred to as the diffuxive flux model) of Leighton & Acrivos ([1]) in two notable and closely related ways. The first is in the rheological model for the suspension and the second is in the manner in which particle migration is incorporated. The diffusive flux model employs a Newtonian rheology with a concentration-dependent shear viscosity and postulates a form for the cross-stream flux. The suspension-balance model, on the other hand, employs a non-Newtonian bulk stress with shear-induced normal stresses and relates the cross-stream flux of particles to the variation of the normal stresses.

Experiments with concentrated suspensions involving non-rectilinear flows were conducted for the first time by Altobelli et al[12] in a pressure driven horizontal pipe flow with a suspension containing heavy particles. Here, in contrast to the corresponding suspension flow of neutrally buoyant particles([10],[13]), the existence of an angular dependent density distribution induces a secondary flow within the cross-section of the pipe and hence, even for the fully-developed flow, all three velocity components will be non-zero and will be functions of the two transverse coordinates. This secondary flow generates a convective particle flux along the cross-sectional plane, in addition to the flux due to shear-induced diffusion and gravitational sedimentation. Later, Zhang and Acrivos[2] extended the shear induced migration model to this multidimensional case by taking the effective shear rate in the model equations equal to the square root of the second invariant of the rate of deformation tensor and found good qualitative agreement between their model calculations and the experimental results of Altobelli et al[12].

In our work, we first performed experiments involving the pressure driven flow

of suspensions containing heavy particles in a pipe. As mentioned before, Altobelli et al[12] conducted similar experiments with heavy particles and measured the velocity and concentration profiles for the fully developed flow using the technique of nuclear magnetic resonance imaging(NMRI). But due to the low spatial resolution of the NMR images, their concentration and velocity profiles yielded primarily qualitative results. In addition, the pressure drop across the pipe, which is essential for any comparison with the results of the model predictions, was not measured. In our experiments we used the technique of Laser Doppler Anemometry for making accurate measurements of the axial velocity profiles. We also measured the pressure drop using a digital pressure transducer. We made quantitative measurements of the cup-mixing particle concentration and the resuspension height. We then compared these results with those of model calculations, similar to those performed by Zhang and Acrivos[2]. We first summarize the experimental part of the work. Subsection 1.2.1 deals with the details of the material preparation and their characterization as well as with the description of the techniques used for the experimental measurements. Subsection 1.3 details the various experiments performed and discusses our results in light of Altobelli's experimental findings. Section 1.4 deals with the numerical solution of the momentum and mass conservation equations and the comparison between the computed results and those found experimentally. First of all (c.f. subsection 1.4.1), following Zhang and Acrivos[2], we solved the Navier-Stokes equations together with the particle conservation equation using a regular Galerkin finite element technique along with a uniform mesh. Here, since the unsteady state (in pseudo-time) fully developed flow equations were being solved, it was required that the total average particle concentration across the cross-section of the pipe be conserved throughout the computations. However, we found that, during these computations (also referred to as the time-dependent computations), the total particle concentration did not remain constant and that,

as a result, the computations did not converge. On closer inspection we determined that the high concentration gradients were not accurately captured by the coarse mesh. In order to overcome this difficulty, we used instead a non uniform mesh for our finite element computations such that the node density was higher in the regions of high particle concentration gradients. In addition, we also employed the Petrov-Galerkin weighting functions which have been known to improve the quality of the solutions compared to those using the regular Galerkin weighting functions for problems involving sharp gradients. In section 1.4.3 we compare the results of the time-dependent computations with those of our experiments. In general we found good agreement between the two for the axial velocity profiles and the pressure drop. However, this was not so for the particle cup-mixing concentration and the resuspension height. The discrepancy between the results of the model calculations and those of the experiments prompted us to investigate the possibility of having non-unique solutions. We, therefore, solved the steady state developing flow equations (c.f section 1.5) where, in contrast to the time-dependent calculations, the average mass flux of particles (or the cup-mixing concentration) was conserved and the total average particle concentration changed during the computations (also referred to as the cup-mixing computations). It was found that, for a given set of parameters both the cup-mixing and the time-dependent computations yielded essentially identical solutions. We conclude therefore (section 1.6) that the simple model proposed by Zhang & Acrivos([2]) is not capable of accurately describing the resuspension of heavy particles in a pressure driven pipe flow and is in need of major improvements.

1.2 Experimental Investigation

Before we discuss in detail our experimental findings, we point out some of the deficiencies in the NMRI results obtained by Altobelli et al. ([12]), which

motivated us to conduct the present resuspension experiments. To this end we note that the NMR images obtained by Altobelli et al. consisted of the axial velocity and concentration profiles in the cross section of the pipe, each presented as a 64 by 64 array of numbers. This is seen in figures 1.1 and 1.2 which depict, respectively, the concentration (in %) and velocity(in cm/sec) profiles for the case of a 23% average concentration suspension. It should be noted that the image as represented by the array includes regions lying outside the pipe, which are denoted by the number 0 in both the arrays. Since the particles are heavier than the fluid, the concentration profile shows a region of clear fluid in the top portion of the pipe, where the concentration reads a value of 0. The finite numbers in the array above this region represent the wall of the pipe. Thus, the thickness of the pipe in the vertical(and the horizontal) directions, as inferred from this array, is about 5 numbers. Now, if we look at the corresponding velocity profile (figure 1.2) we find that the image shows finite velocities along the wall of the pipe. For example, at the top of the pipe, the array shows velocities in the range of 1 cm/s to 6 cm/s on the wall of the pipe, under conditions where the maximum velocity at the center of the pipe is 13 cm/s. This amounts to a significant error in the determination of the axial velocities. Also the values for the concentration close to the wall at the bottom of the pipe seem to have the same values as those observed in the region representing the solid wall of the pipe. From these observations we conclude that although the NMRI results of Altobelli et al. are useful in giving us a qualitative picture of the resuspension phenomenon, they are not accurate enough to allow us to make a quantitative comparison with the results of model calculations.

We therefore measured the axial velocity profiles of the suspension across the tube's cross-section at various Reynolds numbers and concentrations using the Laser Doppler Anemometry technique (figure 1.3) and also measured the resuspension height, the pressure drop and the cup mixing concentration for comparison with

those computed from model calculations.

The flow system consisted of a reservoir, a progressive cavity pump and circular pipes (figure 1.4). The reservoir contained the suspension, where the particles were suspended by being mixed continuously with a magnetic stirrer at the bottom plus an agitator at the top to insure a well-mixed suspension. The suspension temperature was controlled by fixing the water temperature in a refrigerated bath/circulator system where the water was circulating through the coils installed inside the tank. Two digital gauges were placed at the ends of the rigid acrylic tubing and were used to measure the system pressure. In addition, a differential pressure gauge was also installed to measure the pressure difference between the ends of the stiff tubing.

1.2.1 Experimental Approach

Material preparation and characterization

Measurement of fluid viscosity

The viscosity of Triton X-100 was measured using a Haake, CV-20N viscometer. The fluid was found to be Newtonian and its viscosity was found to be very sensitive to the temperature (figure 1.5).

Particle sieving and density segregation

The spherical acrylic particles were sieved between screens with openings of 600 μm and 710 μm to obtain fairly monodisperse particles with a mean diameter of 655 μm. The particles were then density segregated using a glycerol and water solution of density 1.16 gm/cc. A few drops of a surfactant (liquid soap) were also added to the solution. This enhanced the surface wetting of the particles and eliminated the possibility that thin air films would form around them, which often led to inefficient segregation.

Experimental measurements

Laser measurements

The particle velocities were measured using a standard LDA technique. This is capable of accurately determining local velocities by directly measuring the frequency shift contained in the light scattered by a particle as it crosses the intersection region of two crossed laser beams. The LDA optical system was obtained from Dantec Inc. It consisted of a 300mW Argon-ion air cooled laser and a single Bragg cell transmission fiber optics. A typical optical system is shown schematically in figure 1.3 where each of its major components is described in the accompanying legend. As shown in this figure, the incoming laser beam was first directed through a beam splitter where it was divided into two beams of equal intensity. One of the beams was then made to pass through the Bragg cell, which shifted its frequency by 40 Mz. The exit beams then entered the Beam Translator module which was used to adjust the separation between the beams. In order to render the size of the measuring volume close to that of the particles, a Beam Expander was placed after the Beam Translator module. The final element before the beams entered the flow system consisted of a plano-convex lens (also referred to as a front lens) with a focal length of $80mm$, which served to focus the two beams onto the same point in space, thereby forming the measuring volume. During the experiments the beam separation was $37mm$, which created a measuring volume of size $d_x, d_y = 12\mu m$ and $d_z = 51\mu m$. A set of close-up lenses connected to a photo multiplier tube termed PM optics by Dantec Inc., was placed in the forward direction and was used for focusing the collected light into a PM tube through a pinhole. In addition, the PM optics also had an adjustable pinhole disc on which the image of an object placed at a distance of $160mm$ to infinity could be observed and focused via an eye piece.

The ouput from the PM tube was connected to an on-line processor with a built-

in FFT chip, developed by Dantec Electronics and called Burst Spectrum Analyzer (BSA). This BSA employed an advanced burst detection scheme to accurately find and validate the burst and was capable of processing signals with a signal to noise ratio as low as -6 dB. A personal computer (Micron pentium 133 MHz) was connected to the BSA via IEEE488 to obtain the data.

The suspension used in this study has a high particle volume fraction. Consequently, for velocity measurements of concentrated suspensions in a tube of diameter of 25.4 *mm*, significant light attenuation had to be anticipated. Therefore, it was necessary to match the fluid and particle refractive indices in order to reduce the turbidity of the suspension. In the present study, the particulate and fluid phases consisted of PMMA particles (n=1.49, density=1.1677 gm/cc) and Triton X-100 (n=1.49, density=1.0609 gm/cc) respectively. It should be noted, however, that the interface in the path between the probe and the measuring region was curved. This distorted the beams' optical path and consequently decreased the accuracy of the velocity measurements. In order to avoid this difficulty, a rectangular box made of Plexiglas, to be filled with Triton X-100, was constructed around the region of the tube where the measurements were taken. Since the refractive indices of the Plexiglas and of the fluid are the same, the beams saw only flat interfaces. However, if one were to move the probe perpendicularly to the tube's axis, the actual distance traversed by the intersection point of the two laser beams would have differed from the physical distance moved by the probe. This difference is due to the refractive index mismatch between the air and the fluid/Plexiglas medium. Therefore, the actual position of the beams (relative to the tube walls) was obtained from the position of the probe on the vernier scale multiplied by a calibration factor.

Fully developed flow conditions

In order to ensure fully developed flow conditions, we constructed rectangular boxes

(as mention in the previous paragraph) around the tube for laser measurements at distances of $3.0m$, $3.7m$ and $4.0m$ from the exit of the pump. We found that, although the velocity profiles at $3.0m$ and $3.7m$ were slightly different, those were essentially identical at $3.7m$ and $4.0m$. All the laser measurements were therefore, made in the box constructed at a distance of $4.0m$ from the pump. In this respect, it should be noted that the cup-mixing concentration measurements, to be described shortly, were performed at a distance of 6 m from the outlet of the pump.

Calibration for the cup mixing measurements

In order to measure the cup mixing concentration, we proceeded as follows: First, a Plexiglas flask was designed to hold a known volume of fluid; the excess was removed through a small vent at center of it's lid. The flask was then calibrated for various concentrations. The calibration curve is shown in figure 1.6 where the x-axis denotes the total weight of the suspension and the y-axis, the total weight of particles in the flask. We can therefore calculate the concentration by,

$$\frac{m_t}{V_t} = \rho_f + \Phi(\rho_p - \rho_f)$$

but since

$$\Phi = \frac{V_p}{V_t}$$

it follows that

$$\Phi = 1 - \frac{m_t - m_p}{m^*}$$

where,

Φ =particle concentration

m_t =total wt. of the suspension

m_p =total wt. of particles in the flask

m^* =total wt. of liquid required to fill the flask completely

ρ_f =density of the pure fluid

ρ_p =density of particles

V_t =volume of the flask

V_p =volume of the total particles

The previous expression can also be written as,

$$\frac{m_t - m^*}{m_p} = 1 - \frac{\rho_f}{\rho_p}$$

which could be used to obtain the average density of the particles given that ρ_f can be measured independently. The value of ρ_p thereby obtained was found to be 1.1677 gm/cc.

Experimental measurement of Φ_{max}

A simple experiment was performed to determine Φ_{max} by settling a known weight of suspension in a beaker. By taking the density of the particles as 1.1677 gm/cc and measuring the settled height of the particles, we calculated the settled bed concentration (after 12 hrs) to lie between 0.59 and 0.61.

Experimental measurement of the average concentration

Altobelli et al. ([12]) computed the average concentration in their experiments by stopping the flow of the suspension and measuring the height of the settled bed after 10 min. We performed a similar exercise on our system for different Reynolds nos. and concentrations and measured the settled height at various times. As can be seen from figure 1.7, the settled height for the 10% and the 20% concentration cases reached a constant value after 10 minutes whereas for the 30% concentration case, it took about 15 minutes.

Flow rate measurements

The flow rate of the suspension was measured by a timed collection procedure. Specifically, the 3-way valve (#6 in figure 1.4), which was at a distance of 6 m

from the outlet of the pump, was used to direct the flow into a measuring cylinder and, in order to maintain the same flow rate, the valve (#8) was tuned to keep the system pressure constant using the pressure gauges (#12) for this purpose. In all the experiments, we noted the time required for collecting $300ml$ of suspension. However, roughly 150-$300ml$($\approx$ 30-$60cm$ tube length) of the suspension was allowed to flow out before starting the stopwatch. This allowed the system to achieve steady state. The flow rate measured was also compared with the flow rate calculated by interpolating the axial velocity profiles obtained from the LDA measurements. The flow rate thereby calculated was on average 4% lower compared to the measured values.

The differential pressure was measured with a differential pressure transmitter. The accuracy of the transmitter was 0.03 inH_2O. The legs of the transmitter were connected to the top of the pipe so as to prevent the particles from entering the legs. A bypass valve with a connecting tube was also connected to the legs. This design enabled us to remove bubbles from the system and also helped in preventing the entry of bubbles into the pressure legs.

Using the above procedure, we checked the accuracy of the pressure transmitter reading for a clear fluid experiment with that calculated using Poiseuille's law from the flow rate measured via the timed collection procedure. The measured mean pressure reading was higher by 7%. However, during the course of the experiment, the pressure transmitter readings fluctuated between -8% and +4.5% about the mean. On closer inspection it was found that the control action of the constant temperature bath caused fluctuations($\pm 1^oC$) in the temperature of the fluid, and thereby affected the viscosity of the Triton fluid. Therefore, during each of the suspension experiments, we took around 125 pressure readings and used their average for comparison with the pressure difference computed from the model.

Resuspension height measurements

The resuspension height was measured using the laser system. When the laser beam intersection was viewed from the top of the observation window, the beams were diffused due to the presence of the particles in the beams' path. However, the beams were sharp when they passed through the clear fluid region. Taking advantage of this observation, we moved the laser beams upward from the bottom of the tube and noted the height when the beams became sharp. This was also confirmed by viewing the suspension layer from the side of the window where we could observe a sharp interface between the particle layer and the clear fluid.

Cup mixing measurements

The procedure which we followed for collecting the suspension for the cup-mixing experiment was similar to that used for the flow rate measurements except that, in this case, the suspension was collected directly into the calibrated Plexiglas flask. We also studied the effect of the system design on the cup mixing measurements in that, instead of letting the suspension flow down through the 3-way valve, we rotated the valve by 180^o so that the suspension would flow upward. This had no effect on the cup mixing measurements.

Effect of suspension concentration on the pump

During our experiments, we found that the pump was able to deliver flow rates corresponding to Re=20 for the 10% and 20% suspensions where the Reynolds number Re is defined in Appendix A. However, for the 30% suspension, we were unable to go beyond Re=9. We felt that, in the case of the 30% suspension, the 3/8 *inch* tube (connecting tube, viz. #2 in figure 1.4, which is connected to the 3-way valve and the tank) was increasing the system pressure to such an extent that the pump was unable to give higher flow rates. We therefore changed the tube to a 1 *inch* tube. Though the system pressure fell drastically (from 17 *psig* to 3 *psig*), there

was no change in the measured flow rate and the cup mixing concentration. This confirmed our earlier assumption that slight changes in the system pressure during the timed collection procedure, did not affect the cup-mixing concentration and flow rate measurements. Also, we were unable to obtain higher Re(Re>9) flows in the case of the 30% suspension with the existing pumps.

1.3 Flow Experiments: Results and Discussion

Clear fluid experiment

The experimentally measured velocity profiles for the clear fluid were in excellent agreement with those predicted theoretically (figure 1.8).

Comparison with Altobelli et al.'s experiments([12])

Table 1.1 contains the complete summary of Altobelli et al.'s and our experiments. In table 1.2, we have tried to arrange the various experiments into different groups so that the experiments in each group have similar values of average concentrations and Reynolds nos. The definitions of the various dimensionless groups have been listed in the Appendix at the end of chapter 4. Table 1.3 contains the details of Altobelli et al.'s system and ours. On comparing our experimental results with those of Altobelli, we see that there is a strong disagreement with respect to the resuspension height at low concentrations ($\approx$10%) and low Reynolds nos. In table 1.2, case B2 of Altobelli et al. ([12]) the resuspension extended upto the midplane (a dimenionless height of 0, see Appendix for the definition) whereas in our experiments (#1 and #4) the dimensionless height was 0.3 and 0.39, respectively, even though our Froude and Reynolds nos. were lower. However if we compare case B3 with our #3 and #6, we get comparable resuspension heights.

Case C2 shows a resuspension height of 0.66, which is in agreement with #7, and #10. Although C2's Reynolds no is lower, both the concentration and Froude

nos. are higher.

Cases B1 and C1 could not be compared with ours since the Reynolds nos. were too low. For all other cases it was not possible to clearly ascertain the resuspension height from Altobelli et al.'s([12]) data.

We can also compare the values for U_{max} (non-dimensional) since Altobelli et al. ([12]) have listed them for each of their experiments. The cases B2 and #1, B3 and #3, C2 and #10 seem to be in good agreement with our respective results.

1.4 Theoretical Investigation

In this section we present a theoretical analysis of the viscous resuspension in a fully developed laminar pipe flow and compare the numerical results with those obtained experimentally and reported in section 1.2. The analysis and the method of solution closely follows that given earlier by Zhang and Acrivos([2]).

1.4.1 Mathematical formualtion

Consider the flow of a suspension of heavy solid spherical particles of radius a in a liquid of viscosity μ_f when the mixture can be modeled as an effective continuum Newtonian fluid with concentration-dependent effective properties. We further suppose that the particle Reynolds number is vanishingly small. The equations of motion for the suspension reduce therefore to the incompressible Navier-Stokes equations in terms of bulk-averaged effective quantities, such as the velocity $\mathbf{u}$ and

$$\rho = 1 + \epsilon\Phi, \text{ with } \epsilon = \frac{\rho_p - \rho_f}{\rho_f} \geq 0, \tag{1.1}$$

where ρ is the effective density divided by ρ_f, the density of the pure fluid, ρ_p is the density of the particles and Φ is their volume fraction. The effective viscosity of

the suspension on the other hand can be represented by a large variety of empirical correlations, among which those used in previous analyses of unidirectional flows are

$$\mu = \left(1 - \frac{\Phi}{\Phi_m}\right)^{-1.82}, \ \Phi_m = 0.68 \tag{1.2}$$

given by Krieger([14]), and

$$\mu = \left(1 + \frac{1.5\Phi}{1 - \frac{\Phi}{\Phi_m}}\right)^2, \ \Phi_m = 0.58 \tag{1.3}$$

proposed by Leighton and Acrivos([15]). Here, μ is the suspension viscosity divided by μ_f, and Φ_m is the solid volume fraction beyond which the suspension can no longer flow.

The particle conservation equation is obtained by balancing the fluxes due to bulk convection, gravitational sedimentation and shear-induced diffusion and by neglecting Brownian diffusion. Next, following a standard approach, we set the settling velocity of a test sphere in the suspension, relative to the bulk velocity, equal to the product of the Stokes settling velocity of an isolated sphere times a monotonically decreasing function of Φ, the so-called hindrance function $f(\Phi)$, which accounts for the reduction in the settling velocity due to particle interactions. Thus, the expression for the sedimentation flux becomes

$$\mathbf{N_G} = \frac{2}{9}\frac{a^2(\rho_p - \rho_f)}{\mu_f}\Phi f(\Phi)\mathbf{g}, \tag{1.4}$$

where, as done previously([5],[6],[16]), we approximate $f(\Phi)$ by the means of

$$f \cong \frac{1-\Phi}{\mu} \tag{1.5}$$

As was mentioned earlier, up to now, the expressions for the flux due to shear-induced particle diffusion have been proposed and tested experimentally only for unidirectional flows in which both the shear and the particle volume fraction are functions of a single position variable. In such cases the particle flux can be expressed as

$$\mathbf{N_d} = -D_c \nabla\Phi - D_s \nabla\dot{\gamma} \tag{1.6}$$

where the scalars D_c and D_s are, respectively, shear-induced diffusion coefficients and $\dot{\gamma}$ is the shear rate. For more general flows, one would expect the expression for the particle flux to be more complicated and the diffusion coefficients to be second-order tensors rather than scalars. However, in order to keep the analysis as simple as possible, we shall proceed with our model by generalizing equation 1.6 and retaining D_c and D_s as scalars. In addition we let the effective shear rate in equation 1.6 be proportional to the square root of the second invariant of the rate of deformation tensor $\mathbf{d}$, i.e.

$$\dot{\gamma} = (2\mathbf{d} : \mathbf{d})^{\frac{1}{2}} \tag{1.7}$$

where $\mathbf{d} \equiv \frac{1}{2}(\nabla\mathbf{u} + \nabla\mathbf{u}^{\mathbf{T}})$. For unidirectional flows, $\dot{\gamma}$ in equation 1.7 is equal to the absolute value of the shear rate.

Based on dimensional analysis and the mechanisms of shear-induced diffusion, it was found([15]) that the coefficient D_c should be proportional to $a^2\dot{\gamma}$ while D_s should be proportional to a^2. The dimensionless form of these coefficients, which are similar to those used by Zhang & Acrivos([2]), is:

$$\hat{D}_c \equiv \frac{D_c}{a^2\dot{\gamma}} = 0.43\Phi + 0.65\Phi^2 \frac{1}{\mu}\frac{d\mu}{d\Phi},\ \hat{D}_s \equiv \frac{D_s}{a^2} = 0.43\Phi^2, \tag{1.8}$$

with equation 1.2 for μ (Phillips et al. [10]).

We now restrict our attention to fully developed pressure-driven flows in horizontal pipes (Poiseuille flows). The flows are two dimensional in the sense that the flow velocity and the particle concentration vary along the cross-section of the pipes. Let us further denote by x_1 and x_2 the coordinates along, respectively, the horizontal and vertical directions within the cross section. Then, by introducing L and U, respectively, as the characteristic length and velocity, we can write the governing equations in dimensionless form(Zhang and Acrivos[2]):

$$\frac{\partial u_j}{\partial x_j} = 0, \tag{1.9}$$

$$Re(1+\epsilon\Phi)(\frac{\partial u_i}{\partial t} + u_j\frac{\partial u_i}{\partial x_j}) = \frac{\partial}{\partial x_j}[-p\delta_{ij} + 2\mu(\Phi)d_{ij}] - \frac{1}{Fr}\Phi\delta_{i2},\ i = 1, 2, \tag{1.10}$$

$$Re(1+\epsilon\Phi)(\frac{\partial u_3}{\partial t}+u_j\frac{\partial u_3}{\partial x_j})=K+\frac{\partial(2\mu(\Phi)d_{3j})}{\partial x_j}, \tag{1.11}$$

and

$$\frac{\partial\Phi}{\partial t}+u_j\frac{\partial\Phi}{\partial x_j}=\lambda\frac{\partial}{\partial x_j}\left[\hat{D}_c(\Phi)\dot{\gamma}\frac{\partial\Phi}{\partial x_j}+\hat{D}_s(\Phi)\frac{\partial\dot{\gamma}}{\partial x_j}+\frac{2}{9Fr}\Phi f(\Phi)\delta_{j2}\right] \tag{1.12}$$

where (and hereafter) the summation convention for repeated indices ($j = 1, 2$) is used and δ_{ij} is the kronecker delta. This system of equations contains 4 control parameters: the Reynolds number $Re \equiv \rho_f UL/\mu_f$, based on the properties of the suspending fluid where U and L to be specified later, are, respectively, the characteristic velocity and length scale; the modified Froude number $Fr \equiv \mu_f U/(\rho_p - \rho_f)gL^2$; the relative density ratio of the suspending particles to the suspending fluid; $\epsilon \equiv (\rho_p - \rho_f)/\rho_f$ and, $\lambda \equiv (a/L)^2$, the square of the ratio of the particle radius to the characteristic length scale. The symbol K in equation 1.11 refers to the pressure drop per unit length along the length of the pipe rendered dimensionless by $(\mu_f U)/L^2$. For our computations, we need to specify either the dimensionless pressure drop per unit length(K) or the total flow rate. As will be seen later, we specified the flow rate and calculated the pressure drop as part of the solution.

To complete the formulation, we now turn to the boundary conditions. The velocity at the walls was taken to be zero. In addition, we require that the particle flux into a boundary be zero, i.e. that

$$(N_G + N_d)_j n_j = 0, j = 1, 2. \tag{1.13}$$

where n_j is the unit normal to each boundary. This zero flux condition applies not only on the solid walls but also on the surface of symmetry. Finally, if transient solutions are required, then obviously initial conditions need to be given.

1.4.2 Numerical methods

The system of equations 1.9-1.12 (henceforth referred to as the time-dependent formulation) differs in two respects from that which applies typically in pure fluids. First, the diffusion coefficient D_c depends not only on the scalar Φ but also on the effective shear rate $\dot{\gamma}$ and, furthermore, there is an additional diffusive term, i.e. the second term on the right-hand side of equation 1.12, which involves third-order derivatives of the flow velocity. Secondly, as seen from equations 1.2, 1.3 and 1.8, the viscosity and the diffusion coefficients are all highly non-linear functions of Φ.

To numerically solve this coupled system of non-linear equations, we chose to use the streamline-upwind/Petrov-Galerkin finite-element method (Brooks and Hughes[17]) with an additional discontinuity-capturing term in the weighting function (Hughes, Mallet and Mizukami[18]). Since in our resuspension experiments, the *Re* values were low or moderate, we adopted the penalty formulation (c.f. Baker[19]) for equation 1.9 and equation 1.10 of the secondary flow. Since these secondary flows were very weak, we neglected the inertial term and solved the Stokes equations in equation 1.10. In this formulation, the suspension is supposed to be slightly compressible, and the pressure is defined by

$$p = -\alpha_n Re\mu \frac{\partial u_j}{\partial x_j} \tag{1.14}$$

with the parameter α_n being a large positive constant (Hughes et al.[18]). The pres-

sure, therefore, is no longer a primary field variable. This is important for reducing the computational requirements if a large number of nodal points are being used for solving the equations. Now, substituting equation 1.14 into equation 1.10, multiplying by a weighting function w and then integrating over the cross section Ω, we obtain the weak form of equation 1.10:

$$\int_\Omega w(1+\epsilon\Phi)\left(\frac{\partial u_i}{\partial t}\right)\mathrm{d}x + \frac{1}{Re}\int_\Omega \mu\frac{\partial w}{\partial x_j}\left(\frac{\partial u_i}{\partial x_j}+\frac{\partial u_j}{\partial x_i}\right)\mathrm{d}x$$
$$+\alpha_n\int_\Omega \mu\frac{\partial w}{\partial x_i}\frac{\partial u_j}{\partial x_j}\mathrm{d}x = -\frac{1}{FrRe}\int_\Omega w\,\Phi\,\delta_{i2}\,\mathrm{d}x,\quad i,j=1,2, \tag{1.15}$$

where the divergence theorem has been used. Similarly, for 1.11, we have:

$$\int_\Omega w(1+\epsilon\Phi)\left(\frac{\partial u_3}{\partial t}+u_j\frac{\partial u_3}{\partial x_j}\right)\mathrm{d}x + \frac{1}{Re}\int_\Omega \mu\frac{\partial w}{\partial x_j}\frac{\partial u_3}{\partial x_j}\mathrm{d}x = \frac{K}{Re}\int_\Omega w\mathrm{d}x \tag{1.16}$$

We require that the weighting function w in 1.15 and 1.16 vanish on that portion of the boundary where the velocity is prescribed. Similarly, multiplying equation 1.12 with the weighting function w and integrating over the cross section Ω, we have

$$\int_\Omega w\left(\frac{\partial\Phi}{\partial t}+u_j\frac{\partial\Phi}{\partial x_j}\right)\mathrm{d}x+\lambda\int_\Omega\frac{\partial w}{\partial x_j}\left[\hat{D}_c(\Phi)\dot{\gamma}\frac{\partial\Phi}{\partial x_j}+\hat{D}_s(\Phi)\frac{\partial\dot{\gamma}}{\partial x_j}+\frac{2}{9Fr}\Phi f(\Phi)\delta_{j2}\right]\mathrm{d}x=0, \tag{1.17}$$

where the boundary condition 1.13 has been applied.

It has been noted by Zhang and Acrivos([2], henceforth also referred to as ZA)

that the solution of equation 1.12 varies sharply within a thin layer adjacent to the suspension-clear fluid interface. In addition, the location of this interface, which is moving in a time dependent simulation, must be found as a part of the solution. In order, to solve these equations, ZA([2]) adopted the regular Galerkin finite element method along with a uniformly spaced finite element mesh. As an initial condition ZA chose a suspension having uniform concentration, $\bar{\Phi}$, and the corresponding parabolic velocity profile of a single phase fluid. As the computation progressed in time, the particles started settling thereby creating an upper region free of particles and a sharp interface between the suspension and the clear fluid. Simultaneously, this interface kept moving down as the particles settled and became sharper with high gradients of concentration across it. As a result of such steep gradients, the numerical calculations often led to very small negative concentrations in the region just above the interface. ZA found that the concentration equation is highly unstable to the presence of these negative concentration values and tried to circumvent this difficulty by setting the concentration above the interface equal to zero if the computed value was below a predefined small number. But since the grid used by ZA was not sufficiently refined to capture these sharp gradients, the filtering procedure mentioned above often led to a constant increase in the total concentration. Thus ZA's numerical procedure did not conserve the total particle concentration during the computations and as a result the computations did not converge successfully.

In our computations we did not use a uniform mesh. Instead we refined the mesh locally in the upper half of the pipe where high gradients of concentration were expected(fig. 1.9). Secondly, although we used a filtering procedure similar to that employed by ZA, we did not solve for the concentration equation in the region of the clear fluid. These two steps essentially conserved the total particle concentration to a great extent leading to converged solutions.

During our calculations, we used the streamline upwind/Petrov Galerkin (SUPG)

finite element formulation with an additional discontinuity-capturing term in the weighting function (Hughes et al.[20]) for the concentration equation and the regular Galerkin finite element method for the momentum equations. This new term (i.e. the discontinuity-capturing term) has a form that acts in the direction of the solution gradient(in our case, the concentration gradient) rather than in the direction of the flow. Numerical computations, in the past, have shown significant improvement over SUPG without the discontinuity-capturing term on problems involving sharp layers. This method requires one to define a characteristic velocity, a characteristic diffusion coefficient and the sharply varying variable for the calculation of the weighting function. In our calculations, since the secondary flows are weak, we chose, in equation 1.12, the characteristic velocity to be $(2/9)(f(\Phi)/Fr)$, the characteristic diffusion coefficient as D_c and Φ as the sharply varying variable. However, we did not find any quantitative difference between the solutions of the regular Galerkin and the SUPG(with additional discontinuity-capturing term) finite element formulation. The solutions presented in this chapter have been obtained by using the aforementioned SUPG formulation.

In addition to the above computations, we also performed simulations where we neglected the secondary flows (henceforth referred to as the 2D simulations), and solved equations, 1.9, 1.11 and 1.12, the aim being to ascertain the influence of the secondary flows on the shear-induced resuspension phenomenon. Here the SUPG formulation was also employed. However, we had to use a much finer mesh than that required for the 3D simulations since, the absence of secondary flows in the 2D simulations, led to extremely steep concentration gradients. As a result these computations were more difficult to converge.

In the spatial discretization of 1.15-1.17 we used the isoparametric, quadrilateral, Lagrangian quadratic elements (c.f Reddy[21]). Thus, the dependent variables in equations 1.15-1.17, were interpolated in terms of the quadratic shape functions ψ_k,

i.e.

$$u_i = \psi_k U_{ik},\ \Phi = \psi_k \Phi_k,\ i = 1, 2, 3, \tag{1.18}$$

where U_{ik} and Φ_k denote the values of, respectively, the velocity components and the concentration at the nodal points k. Then, these interpolations were substituted into 1.15-1.17, and the resulting integrals were calculated by means of a second-order Gaussian quadrature. However, a first order quadrature was used in evaluating the penalty term in equation 1.15 in order to maintain numerical stability.

Similar to the method adopted by Zhang and Acrivos([2]), we also defined $\dot{\gamma}$ as a primary variable and computed it from the algebraic equation 1.7. The gradients of the velocities at each node required for its calculation was computed via the least squares finite element algorithm and were smoothed by using arithmetic averages. Once the value of $\dot{\gamma}$ was computed at each node, it was again smoothed by the aforementioned procedure.

All our numerical computations were time-dependent and, whenever a steady solution was required, it was obtained as the time-asymptotic result of transient solutions. All the four equations (1.15-1.17) of the time-dependent formulation were solved simultaneously with the concentration equation and the axial velocity momentum equation discretized in time by the finite difference Crank Nicholson method, and the other two momentum equations discretized (in time) by the finite difference fully implicit method. The Gauss-Elimination method was used for inverting the matrix and the successive substitution method was used to iterate at each given time step. We were forced to use the Gauss-Elimination method for the 3D simulations since other faster methods of matrix manipulations have been found to be unstable for the penalty method. On the other hand, since we did not have

to solve for the secondary flows in the 2D simulations, we used a variant of the conjugate gradient method for solving sparse matrices.

1.4.3 Numerical results of the Time dependent formulation and Comparison with Experiments

Based on the algorithms described in the last section, we developed a finite-element code from a library of C++ finite element subroutines called DIFFPACK(version 3.0)[22] developed by Numerical Objects Inc., Norway. We then applied it to the fully developed, pressure driven, steady suspension flow within a circular pipe. For this flow, we chose as the characteristic length and velocity, respectively, the radius of the pipe, R, and Q/R^2, where Q is the volumetric flow rate. Since the dimensionless pressure (K) is only a function of the axial coordinate (x_3), we modified equation (1.11) slightly by dividing it throughout by K and substituting u_3^+ for u_3/K. Then, in our computations, the dimensionless pressure gradient was determined by,

$$\int_\Omega u_3^+ \, \mathrm{d}x = \frac{1}{K} \tag{1.19}$$

which is equivalent to the flow rate conservation equation given by,

$$\int_\Omega u_3 \, \mathrm{d}x = 1, \tag{1.20}$$

with the domain of integration Ω extending over the entire cross sectional area. In addition, because the vertical diameter of the circular cross section is now a symmetric surface, solutions over only a half of the circle are needed. Figure 1.9 shows the finite-element mesh used for most of the results given hereafter. During

the construction of this mesh, every effort was made to reduce the distortion of the elements.

We computed the steady solution, as mentioned earlier, as the time-asymptotic results of time-dependent solutions using as initial conditions the parabolic velocity profile of a single-phase fluid and a uniform concentration $\bar{\Phi}$. Because, as can be seen by integrating equation 1.12 over the cross section of the pipe, the mean concentration within the cross section, i.e.

$$\bar{\Phi} = \frac{1}{\Omega} \int_{\Omega} \Phi \, \mathrm{d}x \tag{1.21}$$

must remain unchanged at any time step, we used this condition as one of the tests of computational accuracy in our simulations. In fact, in all of our simulations, $\bar{\Phi}$ remained unchanged up to the time when the clear fluid appeared at the top the pipe. Beyond this point the filtering procedure described in the last section was employed. At convergence, the total concentration in the 3D simulations had decreased by less than 3%. However, this decrease in the total concentration was too small to affect the convergence. On the other hand, in the 2D simulations, the total concentration increased rather than decreasing. But again, since the mesh was refined to capture the steep gradients, the increase in $\bar{\Phi}$ at the end of the simulations was less than 3%.

In the special case when the suspension is neutrally buoyant ($\epsilon = 0$), the pipe flow is unidirectional and axisymmetric. An analytical solution of this reduced problem is available (Phillips et al.[10]) and was used in testing our code. Figure 1.10 shows the concentration profile in the radial direction of the cross section for $\bar{\Phi} = 0.2$, where the solid curve represents our numerical results obtained with 285 nodes and the dashed curve is the analytical solution. The numerical solution almost coincides with

analytical profile, except near the center line of the pipe where the analytical solution predicts that Φ should equal its maximum value Φ_m so that the local viscosity is infinitely large, and where the concentration gradient is discontinuous. It is obvious that, in order to have the numerical results converge to the exact solution in the vicinity of this singular point, the local mesh resolution must be infinitely high.

We now present our results for both the 2D and the 3D simulations for the flow of suspensions containing heavy particles and compare them to our experimental findings. Although table 1.1 contains 14 experiments, these correspond to essentially 7 different cases. We therefore have chosen 7 of the 14 experiments, viz. experiment nos. #4 to #9 and #13 for comparison with computations. This comparison for the 3D simulation is made in figs. 1.11-1.24, 1.27-1.28(c) and 1.29-1.30 where, for each case, we show the axial velocity profiles at four sections (i.e. at different values of x_1), the concentration profile at the same four sections, the secondary flow velocity vectors and a color plot of the concentration profile in the cross sectional plane of the pipe. The results for the 2D simulations computed for one of the cases is shown in figures 1.25-1.26, 1.28(d). In all the plots, the variables X and Y represent, respectively, the coordinates x_1 and x_2. Table 1.4 compares the cup mixing concentrations, pressure drops and the resuspension heights. In our computations, the cup-mixing concentration was calculated as,

$$\Phi_{cup} = \frac{\int_\Omega u_3 \Phi \, \mathrm{d}x}{\int_\Omega u_3 \, \mathrm{d}x} \ .$$

On comparing the 2D simulations(figs. 1.26, 1.28(a)) with the 3D simulations(figs. 1.20, 1.28(d)) for the case of $\bar{\Phi}$=20% and Re=13.09, we find that there is a significant difference in the concentration profiles, in that whereas there exists a highly concentrated core close to the center of the pipe for the 2D simulations, such a feature is absent for the 3D simulation. This implies that one cannot neglect the secondary flows in the computations and therefore our experimental results should

be compared with those computed by the 3D simulation. For all the cases, it can be seen that the calculated velocity profiles at the four cross sections seem to be in good agreement with those obtained experimentally, including the extent of skewness. However, some disagreement is seen in the profiles furthest from the center. Also at the higher concentrations, especially at 30%, the experimental velocity profiles are blunt at the center, a noticeable feature missing in the profiles predicted by the model. On the other hand, the dimensionless pressure drops predicted by the model are in close agreement with the experiments, with the 3D simulations predicting a slightly higher pressure drop than observed experimentally except for case #4. In the caption of table 1.4, we have also listed the dimensionless pressure gradient for the case when, for the same average concentrations, the particles are distributed uniformly in the cross section of the pipe (Poiseuille flow). It is interesting to note that in all but one case (average concentration of 30%), the computed pressure drops for the 3D simulations were greater than those calculated for the Poiseuille flow. Figures 1.29-1.30 also contain the velocity vectors of the secondary flow in the plane of the cross section. The complicated fluid motion resulting from the spatially varying density shows a number of weak eddies in the plane. For all cases, the concentration profiles show that, under the action of gravity, a region of clear fluid ($\Phi \equiv 0$) appears at the top of the pipe, and this region becomes smaller when the flow rate and/or the mean concentration increase, illustrating the enhancement of the resuspension with increasing of Q and $\bar{\Phi}$. In all cases but one, the resuspension heights predicted by the model seems to be lower than those found experimentally. Also, the cup mixing concentrations as obtained from all the model calculations are much lower than those observed in the experiments.

1.5 Cup-mixing formulation and the corresponding numerical results

In the last section, it was seen that in all cases the model calculations underpredicted the cup-mixing concentration. It is important to note, however, that the constraint of conserving the area-averaged particle concentration (eq. 1.21) does not apply to flow systems such as ours since, in reality, it is the average mass flux of particles (or the cup-mixing concentration) that remains constant at each cross-section as the suspension flows along the pipe ([23]). The discrepancy between the results of the model calculations and those of the experiments could therefore be due to the presence of multiple solutions to the equations for the fully developed velocity and concentration profiles for a given set of parameters.

Consequently, we investigated the possibilty of having a non-unique solution by solving a simplified set of equations for a developing concentration and flow profile. In order to reflect the constraint of constant average mass flux, the concentration balance equation (eq. 1.12) can be written as,

$$\frac{\partial(u_3\Phi)}{\partial x_3} + \frac{\partial(u_j\Phi)}{\partial x_j} = \lambda\frac{\partial}{\partial x_j}\left[\hat{D}_c(\Phi)\dot{\gamma}\frac{\partial\Phi}{\partial x_j} + \hat{D}_s(\Phi)\frac{\partial\dot{\gamma}}{\partial x_j} + \frac{2}{9Fr}\Phi f(\Phi)\delta_{j2}\right] \qquad (1.22)$$

where, as before, we have neglected the derivative of Φ with respect to x_3 on the right hand side of equation 1.22 since diffusion in the axial direction is negligible compared to the convective term $\partial(u_3\Phi)/\partial x_3$. In addition, since the secondary flow in the cross sectional plane of the pipe is driven by the shear-induced migration flux as well as the gravitational sedimentation flux, both of which are proportional to the square of the particle radius, we have that, $u_3 \sim \mathcal{O}(1)$ and $u_{i=1,2} \sim \mathcal{O}(\lambda)$. In addition, since $x_{i=1,2} \sim \mathcal{O}(1)$, we have, on account of equation 1.22 that $x_3 \sim \mathcal{O}(\lambda^{-1})$. In our experiments, since the value of λ was small ($\sim 10^{-5}$) we neglect all terms of

$\mathcal{O}(\lambda^2)$ and higher in the momentum equations. Therefore, in addition to the particle balance equation 1.22 and the continuity equation,

$$\frac{\partial u_j}{\partial x_j} + \frac{\partial u_3}{\partial x_3} = 0, \quad j = 1, 2, \tag{1.23}$$

we have that

$$0 = \frac{\partial}{\partial x_j}\left[-p\delta_{ij} + 2\mu(\Phi)d_{ij}\right] + \frac{\partial}{\partial x_3}\left[\mu\frac{\partial u_3}{\partial x_i}\right] - \frac{1}{Fr}\Phi\delta_{i2}, \; i, j = 1, 2, \tag{1.24}$$

and,

$$Re(1 + \epsilon\Phi)\left[u_j\frac{\partial u_3}{\partial x_j} + u_3\frac{\partial u_3}{\partial x_3}\right] = K(x_3) + \frac{\partial}{\partial x_j}\left[\mu\frac{\partial u_3}{\partial x_j}\right], \quad j = 1, 2. \tag{1.25}$$

In addition, we neglect the L.H.S. terms in equation 1.25 all of which are $\mathcal{O}(\lambda)$ and retain only the R.H.S. terms which are $\mathcal{O}(1)$. Finally, since we are primarily interested in determining the fully developed velocity profile, we have chosen to ignore all the terms in equations 1.23-1.25 that involve derivatives with respect to x_3 in order to simplify the calculations. Although, admittedly, there is no justification for neglecting the term $\partial u_3/\partial x_3$ in the continuity equation, this should not affect the solutions for the fully developed flow state.

There is no change in the boundary conditions from those applied for the time-dependent formulation except for the value of the velocities on the wall of the pipe. This is apparent from equation 1.22, which shows that the computations will diverge when calculating the particle concentration on the wall if the boundary condition

of no-slip is used for the three components of velocity. We, therefore, assigned a small but finite value (0.05% of the maximum velocity) to u_3 at the wall to ensure convergence. As before, we applied a filtering procedure to eliminate negative concentrations in the clear fluid region.

It should be noted that solving these equations was not a trivial exercise. When we naively discretized and solved the above set of equations, it was found that the cup-mixing concentration could not be conserved during the course of the computations. On closer inspection it became apparent that the discretization and the subsequent linearization of equation 1.25 required that the values of u_3 be taken from the previous iteration. As a result, it seems that a small error was being introduced at every time step in the calculation of the cup-mixing concentration. We circumvented this difficulty by substituting Φ with q/u_3 in eq. 1.22 and then solving the above set of equations in conjunction with,

$$\Phi = \frac{q}{u_3} \tag{1.26}$$

It is important to keep in mind that the difference between the time-dependent and the cup-mixing formulation lies in the fact that, whereas in the former, we introduced a pseudo time derivative of the primary variables (three components of velocity and particle concentration) in their respective steady state fully developed flow equations and then iterated in pseudo time to achieve a converged solution, in the latter case, we solved the steady state developing flow equations by iterating along the axial direction (or pipe length) to arrive at a converged fully developed flow solution. Thus, the cup-mixing formulation is in fact equivalent to following the development of the suspension's velocity and concentration profiles along the

pipe's length from its initial uniform particle distribution across the pipe's cross section (together with a parabolic axial velocity profile) to its final fully developed flow state.

During the course of the simulation it was observed that as the computations progressed in x_3, the particles kept settling and consequently the concentration at the bottom of the tube kept increasing. After a certain value of x_3, which depended on the coarseness of the grid (especially at the bottom of the pipe), the concentration at the bottom wall of the pipe increased suddenly to maximum packing, resulting in the divergence of the computations. On refining the grid at the bottom of the pipe, the computations diverged at higher values of x_3. Therefore, in order to achieve convergence, the finite element grid in our computations, which had 480 nodes initially, was refined successively till a grid of 983 nodes was reached. Any further refinement led to extremely large computation times. Also, as in the case of the time-dependent computations, the coupled set of momemtum and particle conservation equations was solved simultaneously. Specifically, the momentum equations are coupled to the particle conservation equation through the viscosity term in that changes in the concentration profile affect the velocities through the concentration dependent viscosity function. We found that the computations could be carried to higher values of x_3 by decoupling the equations by calculating the viscosity term from the concentrations computed at the previous time step.

Although, we were not able to eliminate the numerical instability completely with the final grid (983 nodes) and by decoupling the equations, we obtained profiles that were very similar to those obtained from the computations (converged solutions) in the time-dependent formulation.

Figures 1.31-1.32 show, respectively, the velocity and the concentration profiles obtained for a cup-mixing concentration of 23% at a Froude number of 0.44 and a Reynolds number of 13.1 (#8). In table 1.5 we compare these results with those

obtained from experiments as well as from the time-dependent computations. As mentioned before, whereas, during the time-dependent computations the total average concentration was constant (and equal to the experimental value of 20%), here, the cup-mixing concentration remained constant (and close to the experimental value of 22.7%) during the computations. We find that in both the computations (table 1.5), the average concentration is higher than the cup-mixing concentration which is contrary to the trend found experimentally.

Both the concentration and the velocity profiles (figs. 1.31-1.32) look similar to those obtained on solving the equations of the time-dependent formulation(figs. 1.19-1.20). This shows that for a given set of parameters (Re, Fr etc.) the numerical computation for both the time-dependent and the cup-mixing formulation appear to converge to the same solution. The solutions of the cup-mixing formulation also show that the model underpredicts the particle resuspension since, for the same value of the cup-mixing concentration, the computations predicted a much higher value of the average particle concentration as compared to that measured experimentally.

1.6 Conclusions

The numerical results indicate that the model underpredicts the extent of particle resuspension because, for a fixed average concentration (time-dependent calculations), most of the particles are present at the bottom leading to low values of the cup mixing concentration. Similarly, the numerical results obtained on solving the cup-mixing formulation show that for a given cup-mixing concentration, the model overpredicts the average concentration as compared to that observed experimentally. In other words, the shear-induced flux, as given by the model, is insufficient in supporting the downward flux of particles due to gravity. The high values of the cup-mixing concentration (in comparison with the results obtained from time-dependent calculations) observed in our experiments seem to be in qualitative agreement with

the observations made by Altobelli *et al.* ([12]) who noticed regions of local maxima in the particle concentration slightly above the center of the pipe. Such features were completely absent in all our concentration profiles obtained via computations (except for the 2D simulation).

To check this, we solved the steady state momentum equation in only the axial direction for a special case where the particle concentration was zero above the pipe's mid-plane and had a finite and a constant value below it (step profile). In figure 1.33, we show the concentration and the computed normalized axial velocity profile (normalized with K, i.e. u_3/K) at the central section of the pipe ($x_1 = 0$) for the average concentrations of 10.3%, 15.4% and 20.6%. These correspond to cases where the particle concentration below the mid-plane was, respectively, 20%, 30% and 40%. It can be seen that the computed cup-mixing concentration in all the three cases is lower than the corresponding average concentration. This is in agreement with the results of our computations. In additon, the figure also includes the computed values of the dimensionless pressure gradient (K) as well as those calculated for the case of Poiseuille flow ($K_{uniform} = (8/\pi)\mu(\Phi)$) where the particles are distributed uniformly through out the cross section of the pipe. On comparing the two solutions, we observe that the computed pressure gradients for the step profiles are higher than those calculated for the Poiseuille flow. Again, these results are similar to those obtained from the computations of the time-dependent and the cup-mixing formulations and they seem to indicate that for a given average concentration, one would obtain higher values of cup-mixing concentration if the particles are concentrated close to the center of the pipe (where the suspension axial velocity is maximum) such as those observed by Altobelli *et al.* ([12]). In this respect, we can see from table 1.4 that for the 2D simulations, where a concentrated core was present close to the center of the pipe for high concentrations and high Re, we obtained cup-mixing concentrations that were higher than those obtained via 3D

simulations.

We also performed computations with concentration dependent viscosity function and diffusion coefficients proposed by Leighton and Acrivos ([1]) and found that they under predicted resuspension as compared to those reported in this chapter (which utilized coefficients proposed by Phillips *et al.* ([10])).

We also checked our experimental results by repeating all the experiments. In this respect it should be noted that although it may appear that the flow system is disturbed while collecting the suspension for the cup-mixing and flow rate measurements, we found a difference of less than 4% (c.f. section 1.2.1) between the values of the flow rate obtained from the timed collection procedure and those obtained by integrating the velocity profiles from the LDA measurements.

Finally, we investigated the possibility that an entrance length of 6 m (about 470 pipe radii), which was the distance between the pump and the 3-way valve, was insufficient for achieving fully developed flow conditions. In this respect, an estimate for the entrance length L_Φ, required for the establishment of a fully developed particle concentration profile, can be obtained readily by balancing the convective flux and that due to sedimentation ([8]). Consequently,

$$\frac{L_\Phi}{R} \sim \frac{\mu(\Phi)\, Fr}{\lambda}.$$

For a suspension with average concentration of 20% and $Fr \sim 0.4$, L_Φ/R is about 1130 which is larger than that present in the experiments. However, the computations for case#8 with the cup-mixing formulation show that the average concentration during the transient stages reached a minimum value of about 22.5% and then increased to a final value of 24% at the fully developed stage. This shows that even if fully developed flow conditions were not achieved in the experiments, the cup-mixing concentration predicted by the computations under transient conditions also disagree with those obtained in the experiments. Also, it does not appear that

the transient results would have been very different if the continuity and momentum equations were to be solved exactly.

These results indicate that although the simple model proposed by Zhang and Acrivos ([2]) predicts velocity and concentration profiles that are in qualitative agreement with those observed experimentally, significant quantitative differences remain between the theoretical predictions and the experimental observations which require further investigation.

Expt. No.	Init. Avg. Conc. (%)	Mean Conc. (%)	Cup Mixing (%)	Q (cc/s)	K	Re	Fr.	Resusp'n height	Umax (dim.less)
1	10.5		10.3	25.7	3.82	7.74	0.26	0.30	0.67
2	10.5		10.9	40.2	3.57	12.09	0.41	0.42	0.65
3	10.5	10.2	10.0	53.7	3.44	16.14	0.55	0.46	0.63
4	10.0		10.0	26.5	3.82	7.95	0.27	0.39	
5	10.0	10.6	11.0	41.4	3.53	12.45	0.42	0.45	
6	10.0		10.5	55.3	3.47	16.61	0.56	0.46	
7	20.0	20.0	21.8	26.3	5.01	7.91	0.27	0.51	
8	20.0	20.2	22.7	43.6	4.77	13.09	0.44	0.62	
9	20.0		23.9	52.3	4.71	15.71	0.53	0.67	
10	20.1		24.1	26.1	5.05	7.86	0.27	0.54	0.59
11	20.1		22.8	37.4	4.73	11.23	0.38	0.57	0.59
12	20.1	21.9	23.1	45.0	4.51	13.52	0.46	0.59	0.57
13	30.0	29.9	37.9	23.8	6.81	7.16	0.24	0.69	0.51
14	30.0		36.7	29.0	7.45	8.72	0.30	0.82	
Altobelli et. al.'s (1991) results									
B1	9.0			20.7		3.72	0.20	-0.18	0.74
B2	9.0			52.7		9.46	0.51	0.00	0.68
B3	9.0			97.8		17.50	0.95	0.45	0.65
C1	23.0			18.1		3.25	0.18	0.50	0.63
C2	23.0			35.6		6.39	0.35	0.66	0.59
C3	23.0			113.0		20.30	1.10		0.56
D1	39.0			8.5		1.53	0.08		0.52
D2	39.0			35.7		6.41	0.35		0.43
D3	39.0			88.2		15.80	0.86		0.44

Table 1.1: A complete summary of Altobelli et. al's results([12]) and those of our experiments.

Case/#	Avg. Conc.	Reynolds no.	Froude no.	Resusp'n ht.	dim.less Umax
1	10.45	7.735	0.26	0.30	0.67
4	10.00	7.948	0.27	0.39	
B2	9.00	9.46	0.51	0.00	0.68
2	10.45	12.09	0.41	0.42	0.65
5	10.00	12.45	0.42	0.45	
3	10.45	16.14	0.55	0.46	0.63
6	10.00	16.61	0.56	0.46	
B3	9.00	17.5	0.95	0.45	0.65
7	20.00	7.91	0.27	0.51	
10	20.10	7.85	0.27	0.54	0.59
C2	23.00	6.39	0.35	0.66	0.59
8	20.00	13.09	0.44	0.62	
11	20.10	11.23	0.38	0.57	0.59
9	20.00	15.71	0.53	0.67	
12	20.10	13.52	0.46	0.59	0.57
13	30.00	7.15	0.24	0.69	0.51
14	30.00	8.72	0.3	0.82	
B1	9.00	3.72	0.2	-0.18	0.74
C1	23.00	3.25	0.18	0.50	0.63
C3	23.00	20.3	1.1		0.56
D1	39.00	1.53	0.083		0.52
D2	39.00	6.41	0.35		0.43
D3	39.00	15.8	0.86		0.44
Note	*The cases B1, B2 .. etc. refer to Altobelli's experiments and the no.s 1,2.. etc refer to our experiments.*				

Table 1.2: Comparison of Altobelli et al.'s results with ours.

COMPARISON OF SYSTEM PROPERTIES

	Our's	Altobelli et. al.
fluid density (gm/cc)	1.0609	0.875
particle density (gm/cc)	1.1677	1.03
ε	0.10067	0.177
avg. dia of particles (mm.)	0.655	0.762
fluid viscosity (P)	2.78	3.84
tube dia. (mm.)	25.4	25.4

Table 1.3: Details of the system properties of Altobelli et al.'s and our experimental set-up.

Expt.	Init. Avg.	Re	Fr	Cup mixing (%)			Pressure drop(K)			Resuspension height		
No.	Conc.(%)			Expt.	Theory (2D)	Theory (3D)	Expt	Theory (2D)	Theory (3D)	Expt	Theory (2D)	Theory (3D)
4	10.00	7.948	0.270	9.99	6.74	6.04	3.82	3.77	3.75	0.39	0.00	-0.05
5	10.00	12.45	0.423	11.00	8.28	6.70	3.53	3.57	3.65	0.45	0.05	0.00
6	10.00	16.61	0.564	10.45	8.50	7.22	3.47	3.56	3.57	0.46	0.20	0.10
7	20.00	7.906	0.268	21.76	18.74	16.53	5.01	4.88	5.21	0.51	0.40	0.35
8	20.00	13.09	0.444	22.74	21.17	18.71	4.77	4.7	4.86	0.62	0.50	0.55
9	20.00	15.71	0.533	23.92	21.77	19.10	4.71	4.54	4.83	0.67	0.55	0.60
13	30.00	7.155	0.243	37.90	31.22	28.77	6.81	6.37	7.2	0.69	0.70	0.70

Table 1.4: Comparison of our experimental results with numerical simulations. The dimensionless pressure gradients for the case of Poiseuille flow ($= (8/\pi)\mu(\Phi)$) are 3.40, 4.80 and 7.34 when the average concentration in a uniformly distributed suspension equals, respectively, 10%, 20% and 30%.

Expt.	Avg. Conc (%):			Cup mixing (%)			Pressure drop(K)			Resuspension height		
No.	Expt.	Theory (time-dep)	Theory (cup-mix)	Expt.	Theory (time-dep)	Theory (cup-mix)	Expt	Theory (time-dep)	Theory(3D) (cup-mix)	Expt	Theory (time-dep)	Theory (cup-mix)
8	20.00	20.00	24.01	22.74	18.71	23.03	4.77	4.86	5.64	0.62	0.50	0.70

Table 1.5: Comparison of the experimental result for an average concentration=20%, Re=13.1 and Fr=0.444 (case # 8) with numerical simulations of time-dependent and cup-mixing formulations.

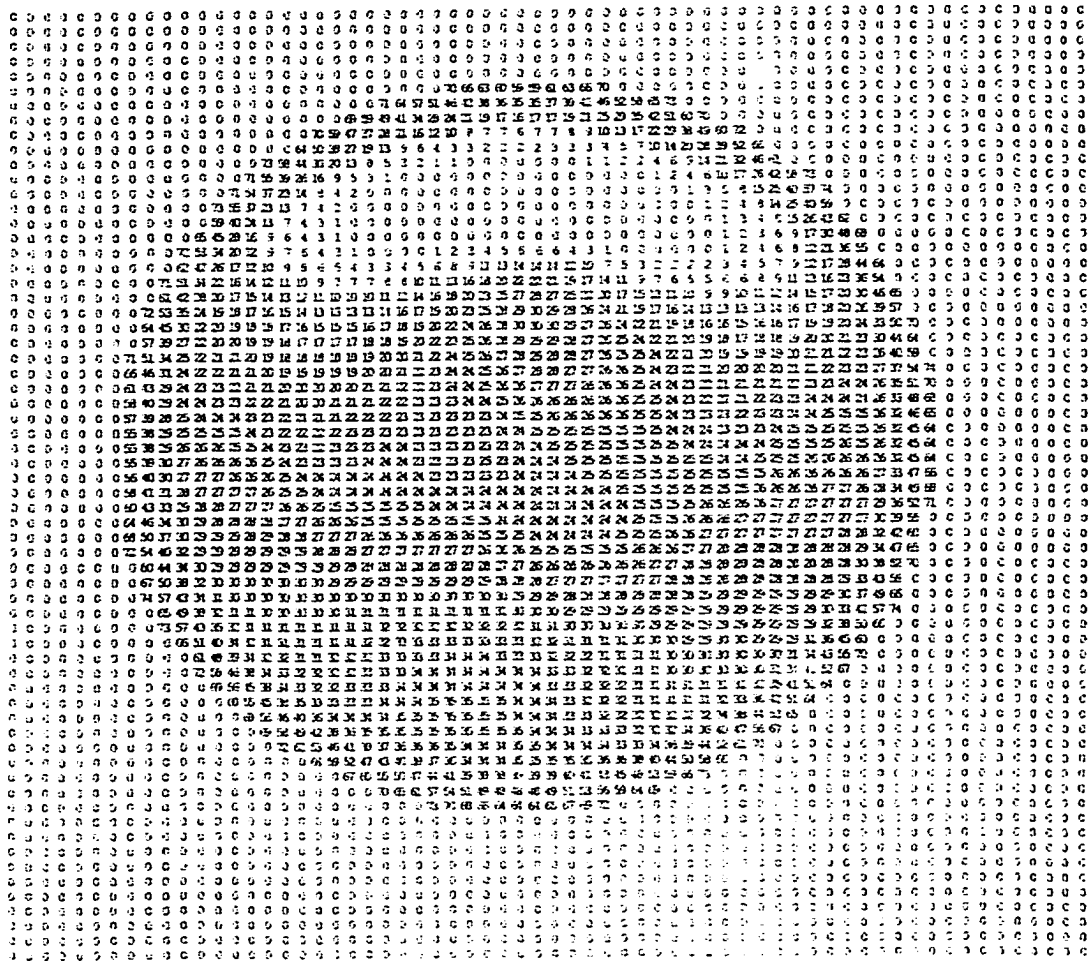

Figure 1.1: This figure shows an 64x64 array of numbers representing the concentration profile for the case of a 23% concentration suspension from the NMRI results of Altobelli et al.([12])

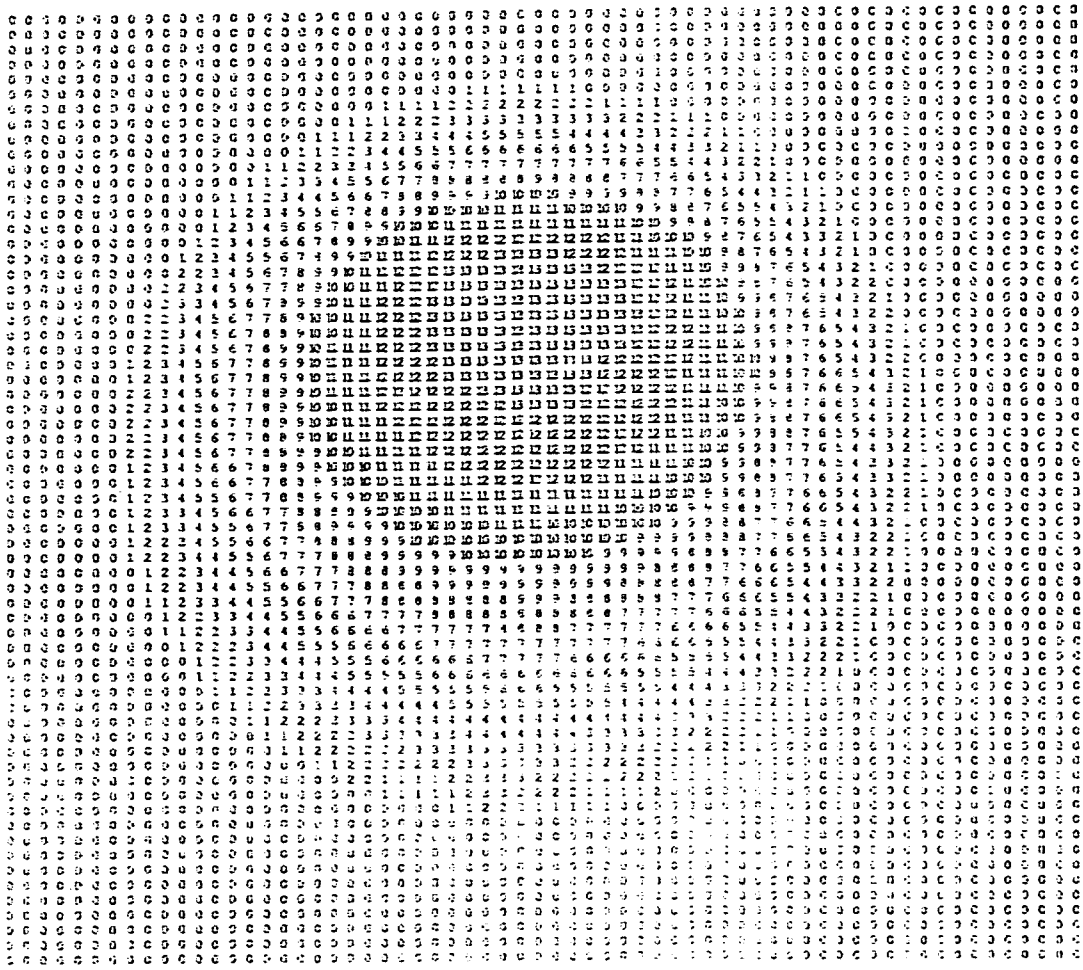

Figure 1.2: This figure shows an 64x64 array of numbers representing the velocity profile(in cm/s), for the case of a 23% concentration suspension from the NMRI results of Altobelli et al.([12])

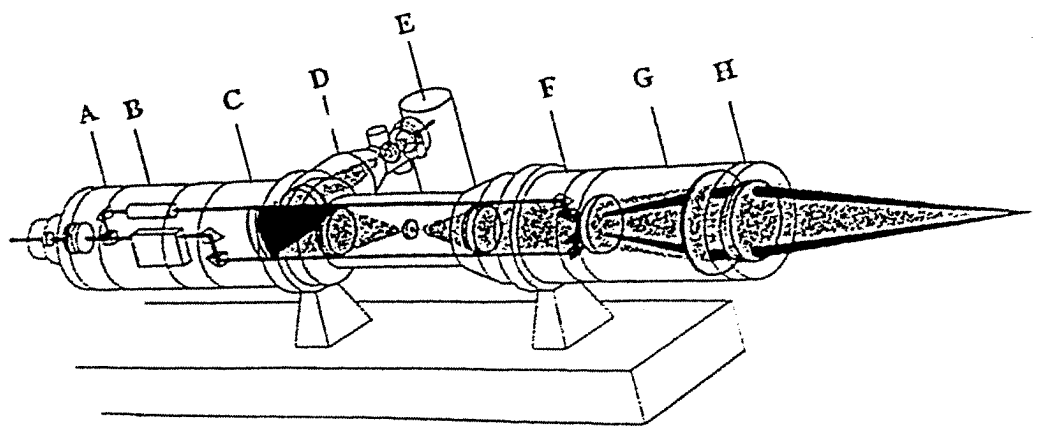

A: Beam Splitter
B: Bragg Cell Section
C: Back Scatter Section
D: PM Optics
E: PM tube
F: Beam Translator
G: Beam Expander
H: Front Lens

Figure 1.3: The optical layout of a typical Dantec Laser Laser Doppler Anemometer

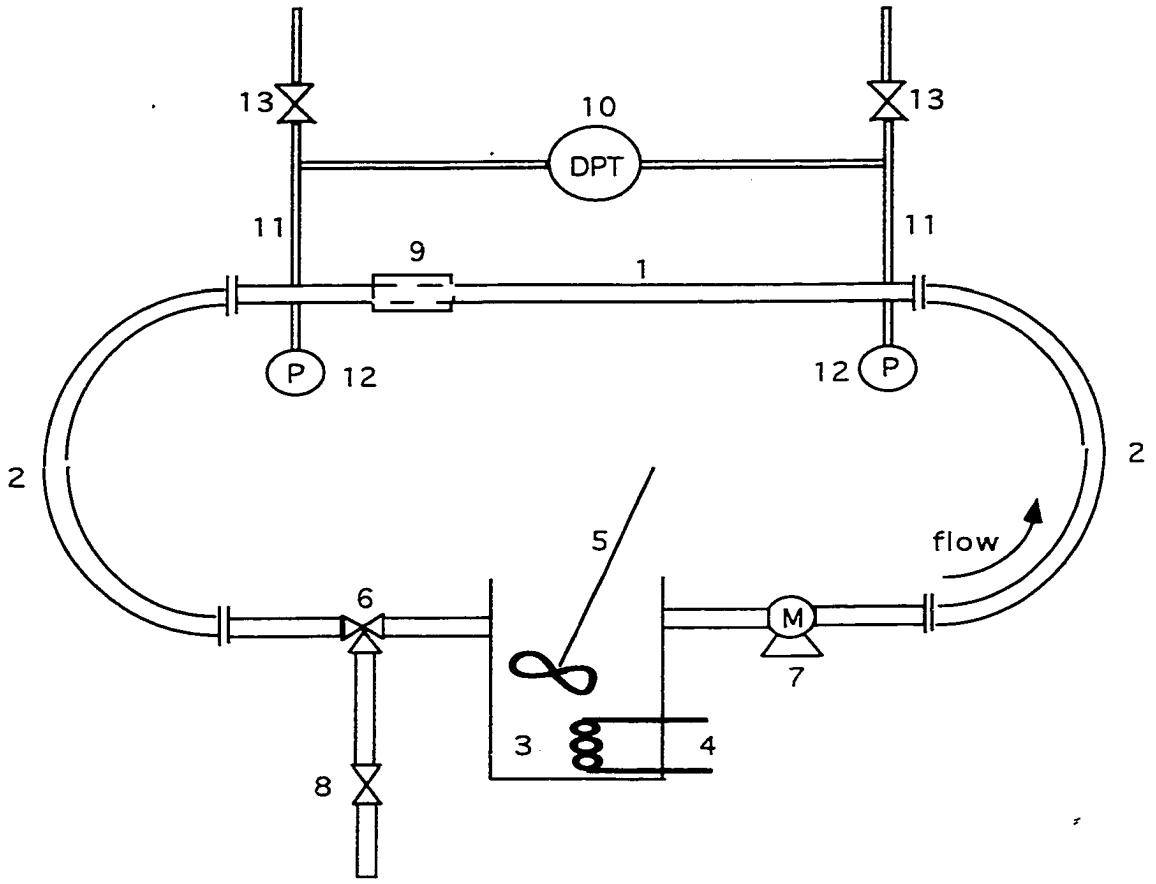

1. Acrylic tubing
2. Flexible tubing
3. Mixing tank
4. Temperature controlled bath
5. Mixer
6. 3 way valve
7. Progressive cavity pump
8. Valve for cup-mixing measurement
9. Test section
10. Differential Pressure transmitter
11. Connection to DPT
12. Pressure gauge
13. By-pass valve with connecting tube

Figure 1.4: The pressure driven flow system

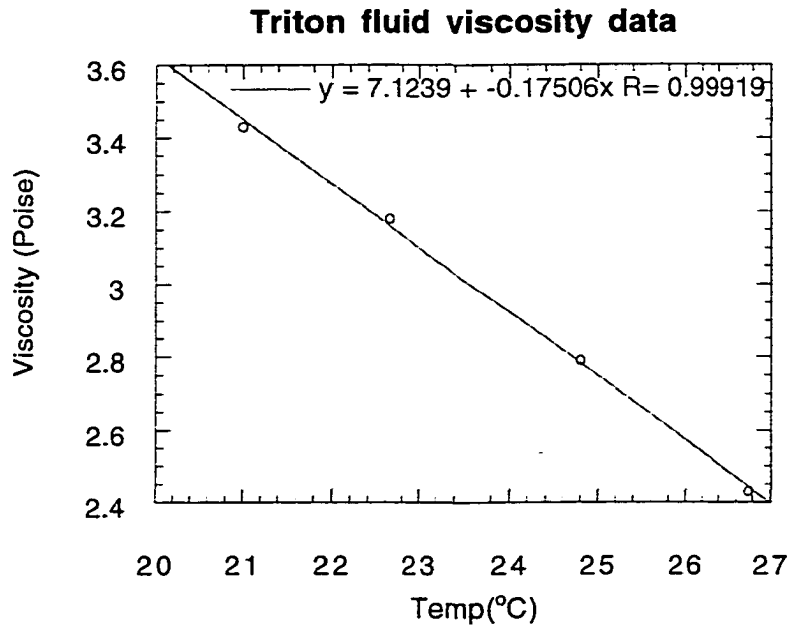

Figure 1.5: The variation of the Triton X-100 fluid viscosity with temperature

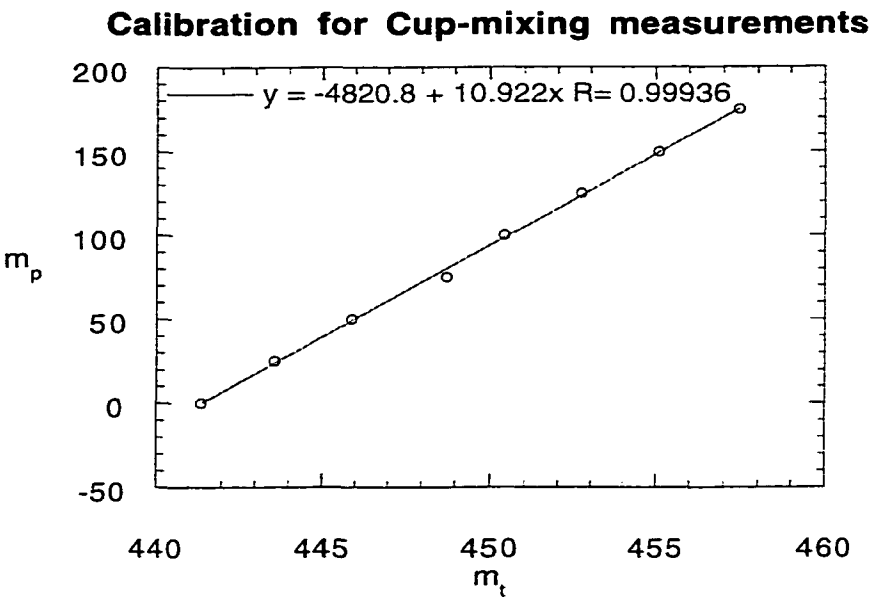

Figure 1.6: This figure shows the calibration curve used for the cup mixing concentration

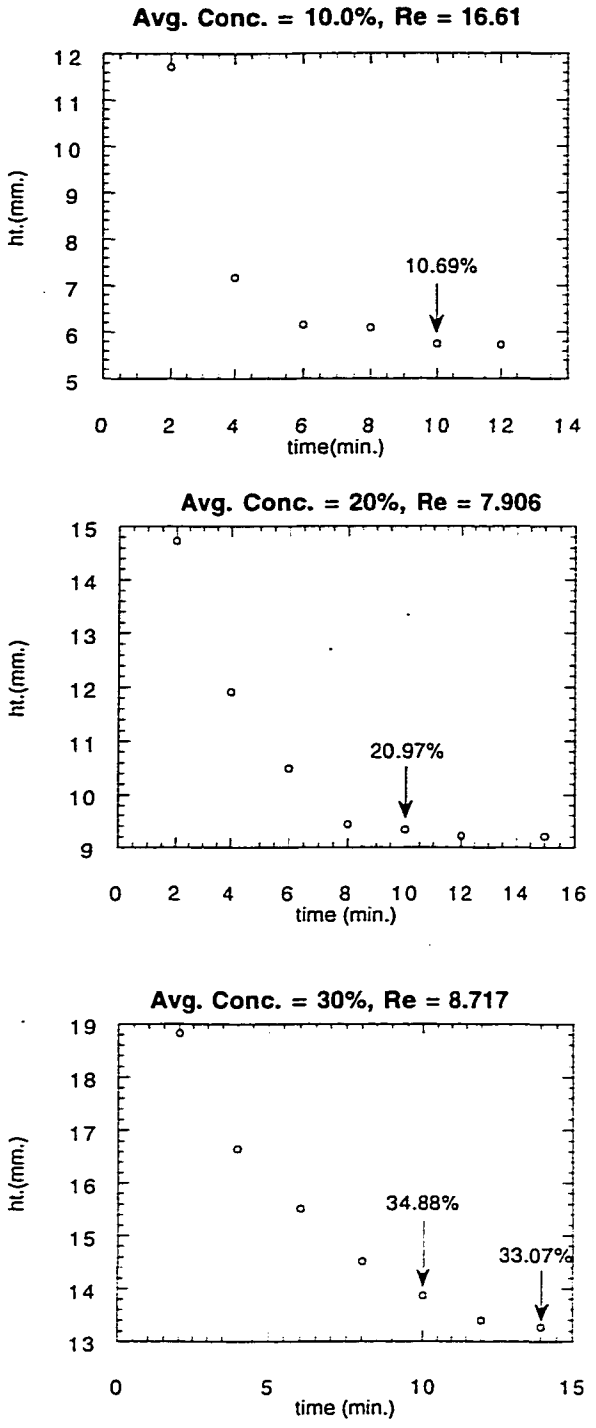

Figure 1.7: Calculation of the average concentration

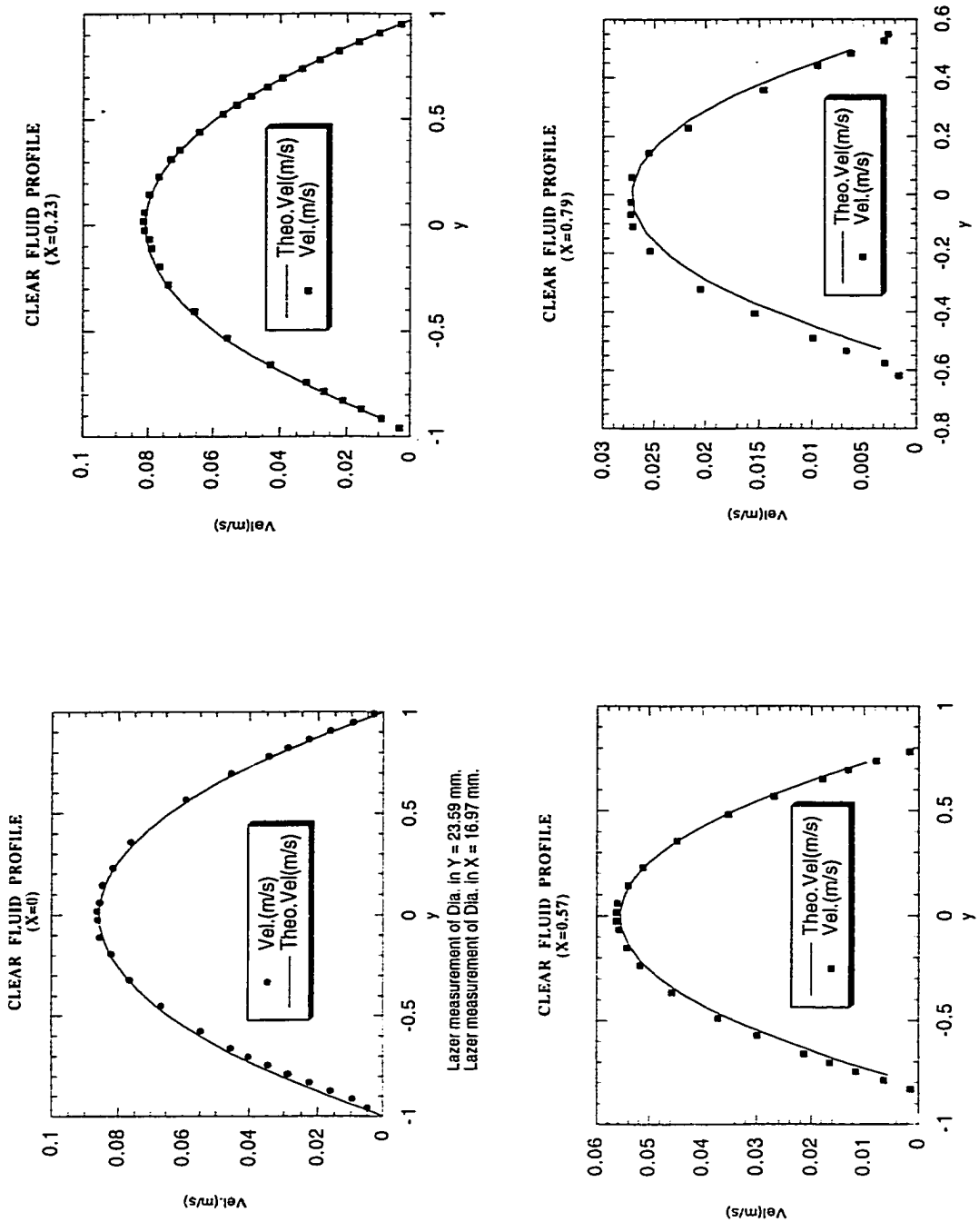

Figure 1.8: LDA velocity measurements for the pure fluid.

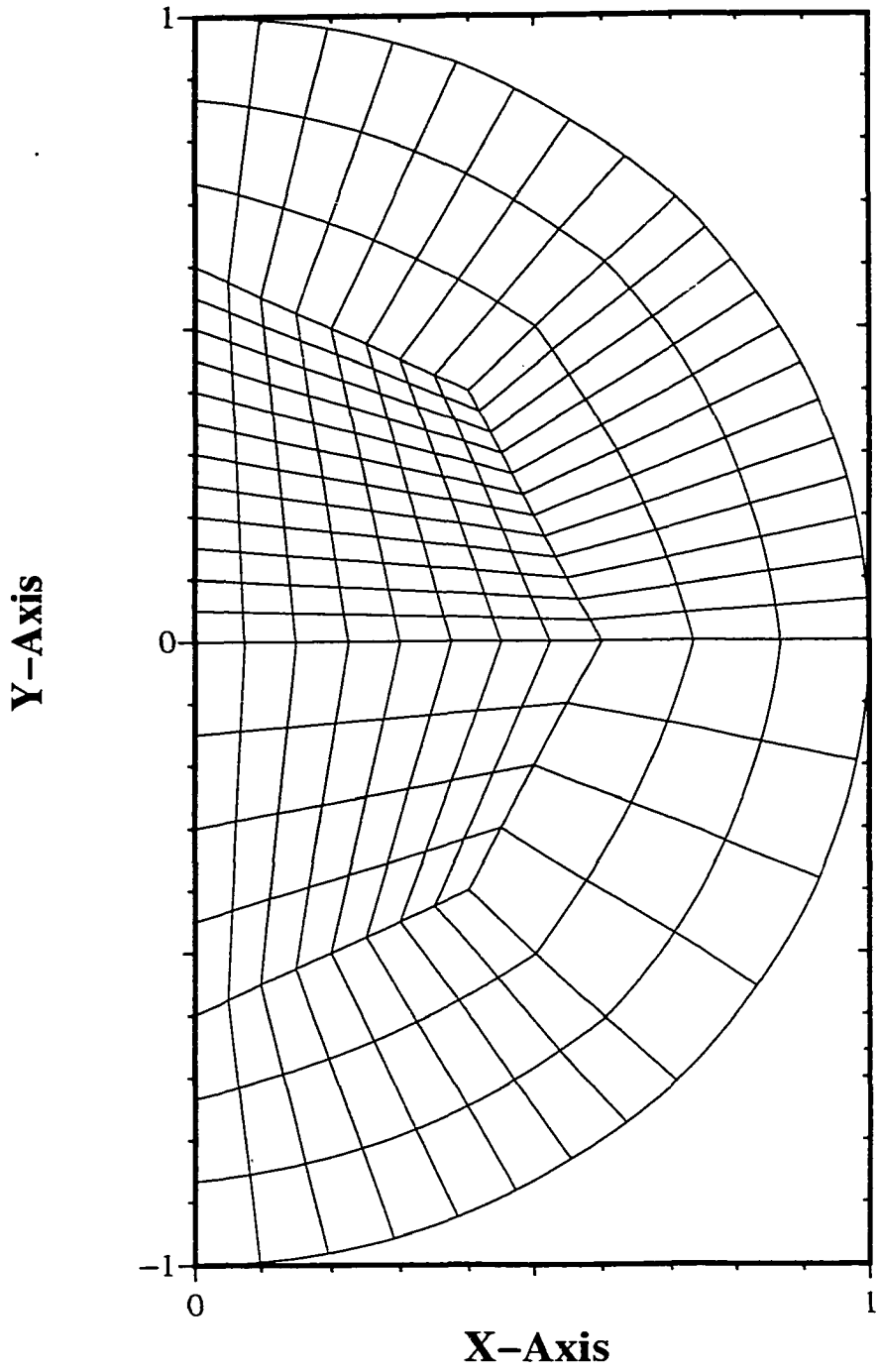

Figure 1.9: A finite element mesh with 224 elements, 9 element nodes and 951 global nodes

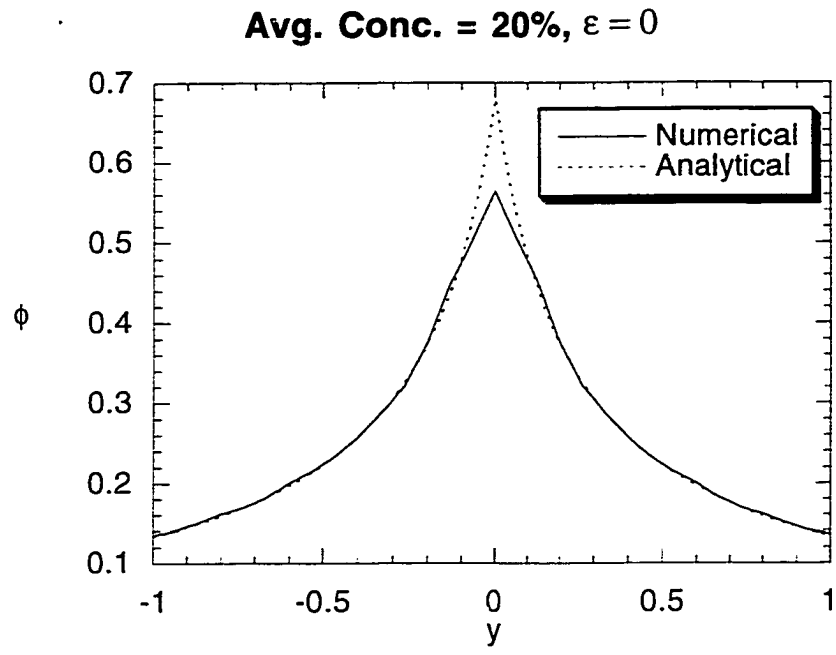

Figure 1.10: A comparison of the axisymmetric concentration profiles between the analytical solution given by Phillips et al. ([10]) and the numerical solution using a uniform grid with 285 nodes

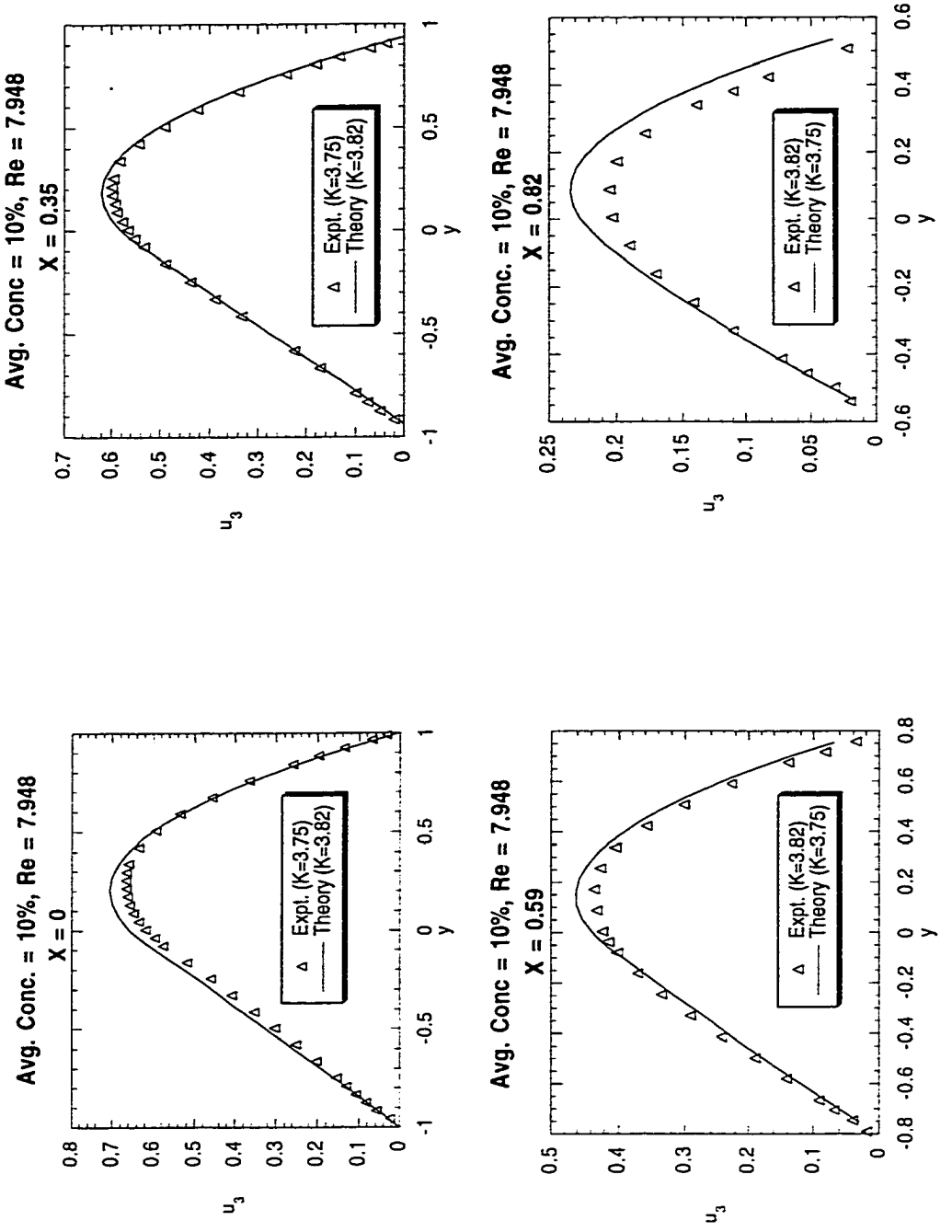

Figure 1.11: This figure shows the comparison of the experimental axial velocity profiles with theory at four cross-sections for the case of average concentration=10%, Re=7.95.

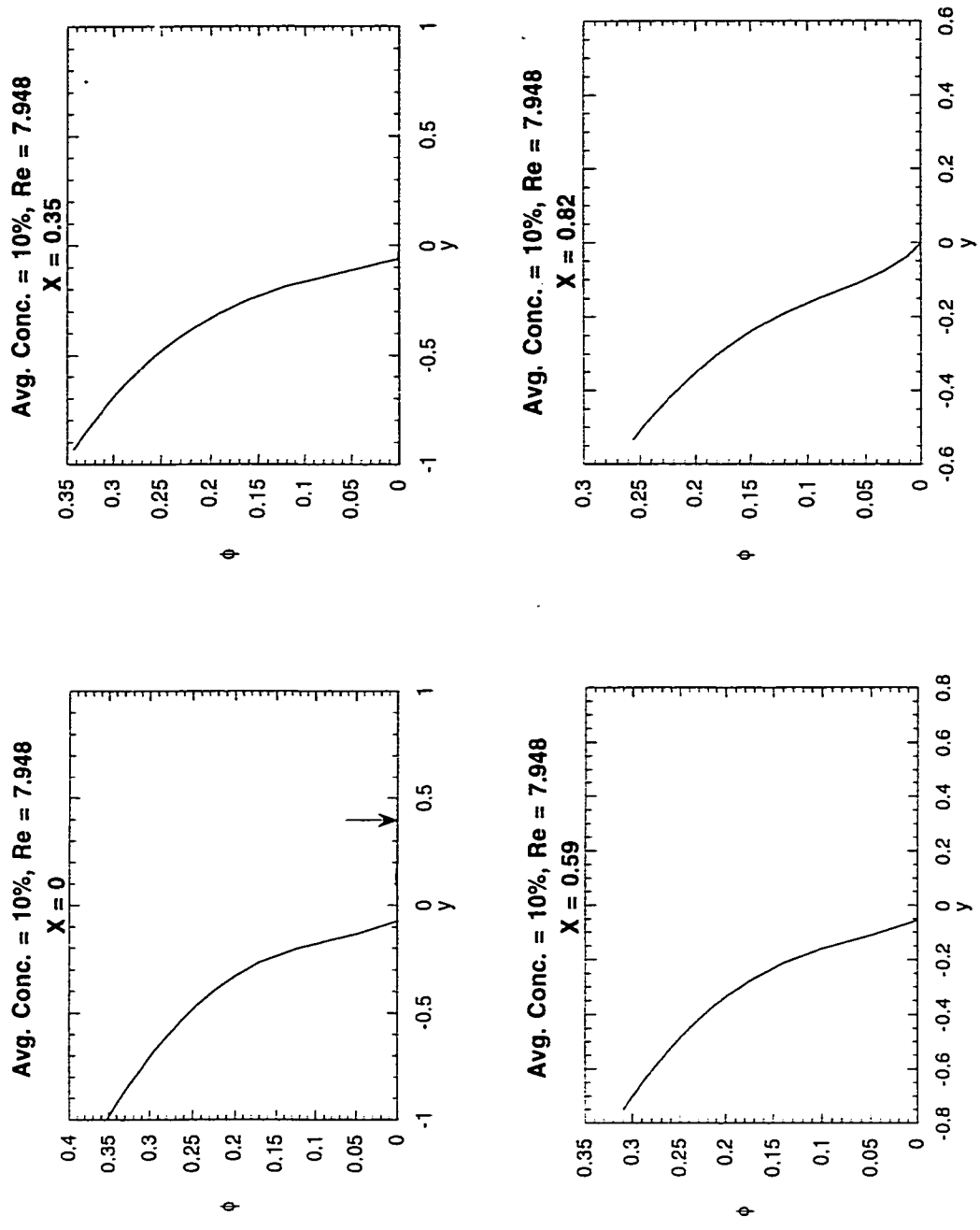

Figure 1.12: This figure shows the theoretically predicted concentration profiles at four cross-sections for the case of average concentration=10%, Re=7.95. The arrow shows the resuspension height observed experimentally.

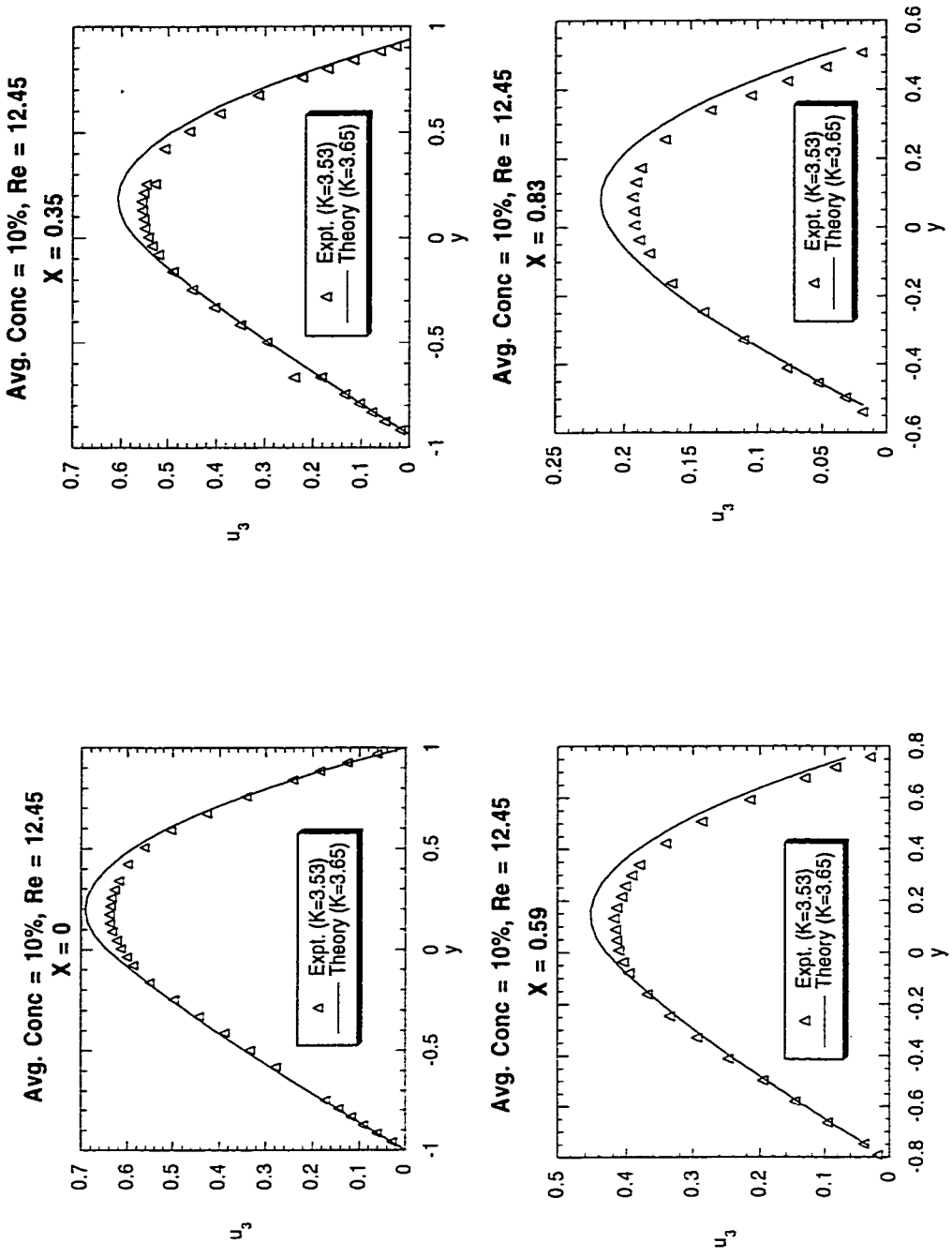

Figure 1.13: This figure shows the comparison of the experimental axial velocity profiles with theory at four cross-sections for the case of average concentration=10%, Re=12.45.

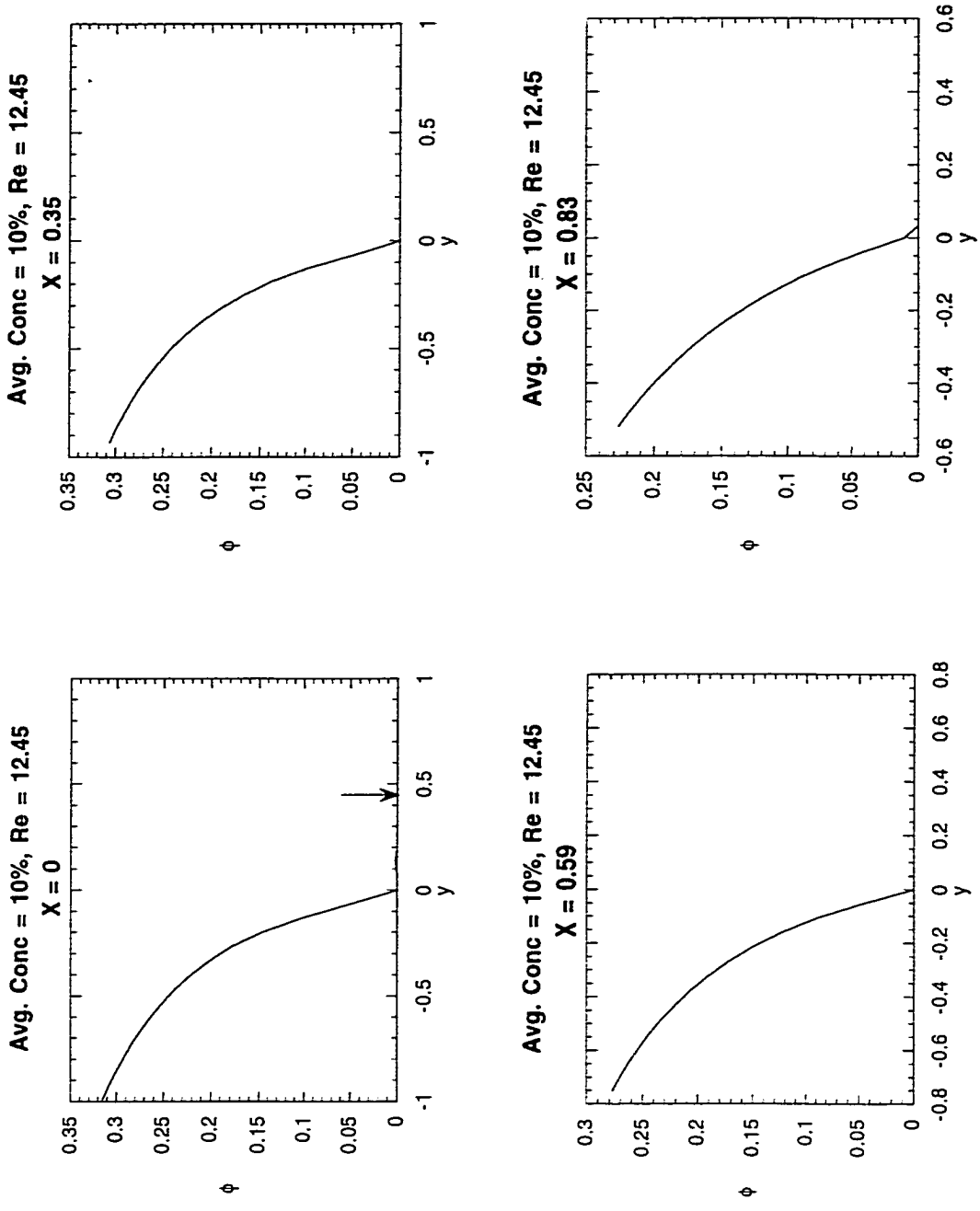

Figure 1.14: This figure shows the theoretically predicted concentration profiles at four cross-sections for the case of average concentration=10%, Re=12.45. The arrow shows the resuspension height observed experimentally.

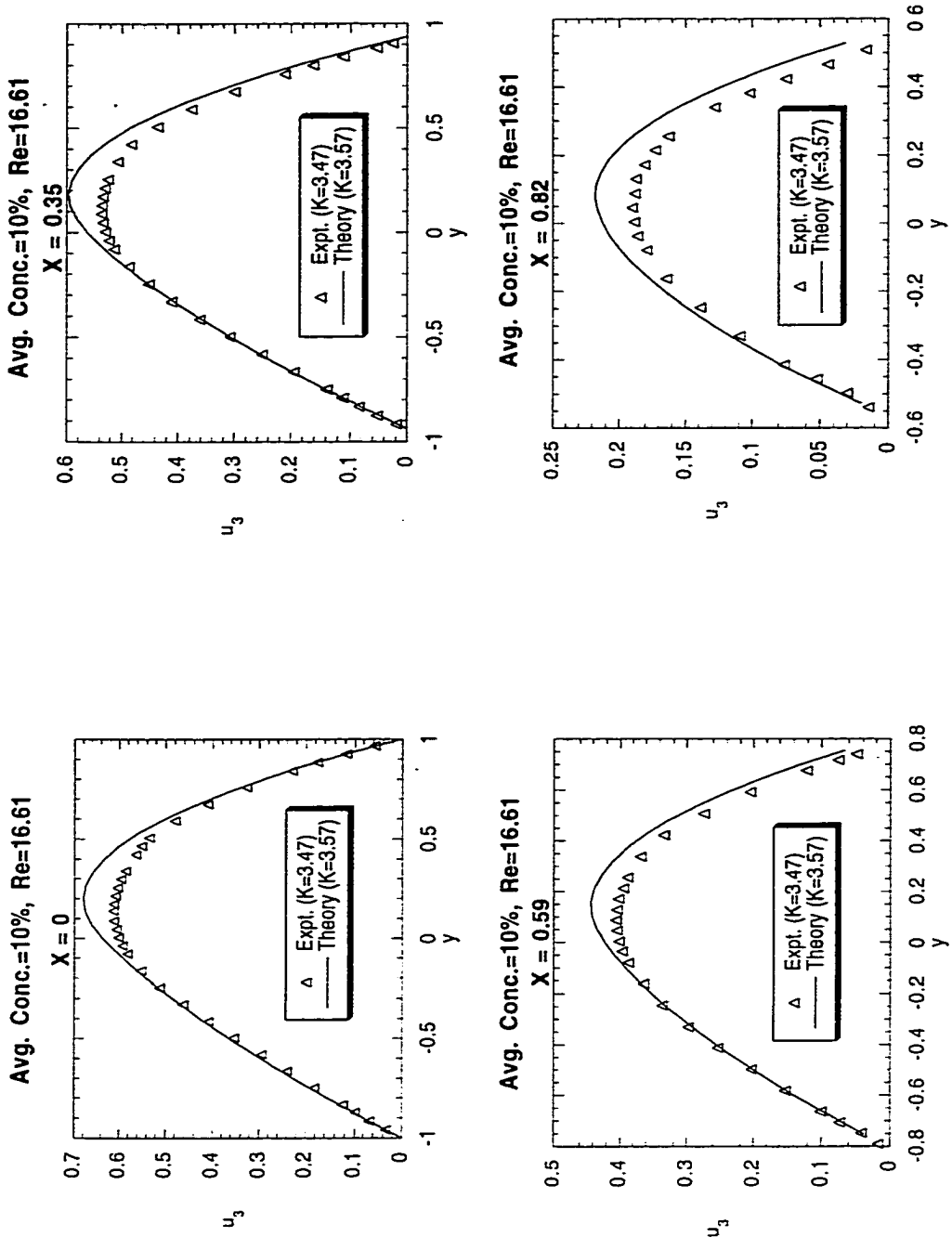

Figure 1.15: This figure shows the comparison of the experimental axial velocity profiles with theory at four cross-sections for the case of average concentration=10%, Re=16.61.

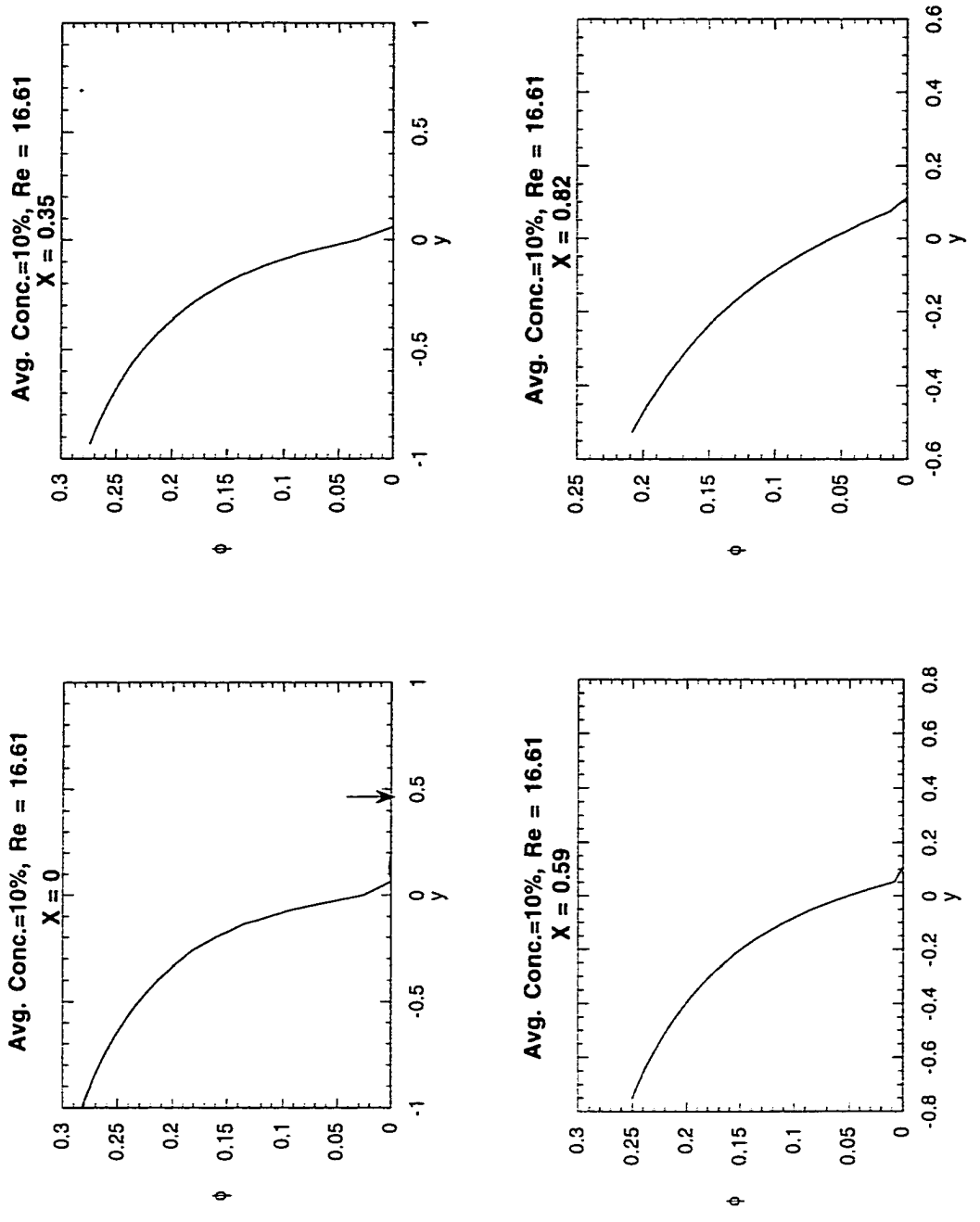

Figure 1.16: This figure shows the theoretically predicted concentration profiles at four cross-sections for the case of average concentration=10%, Re=16.61. The arrow shows the resuspension height observed experimentally.

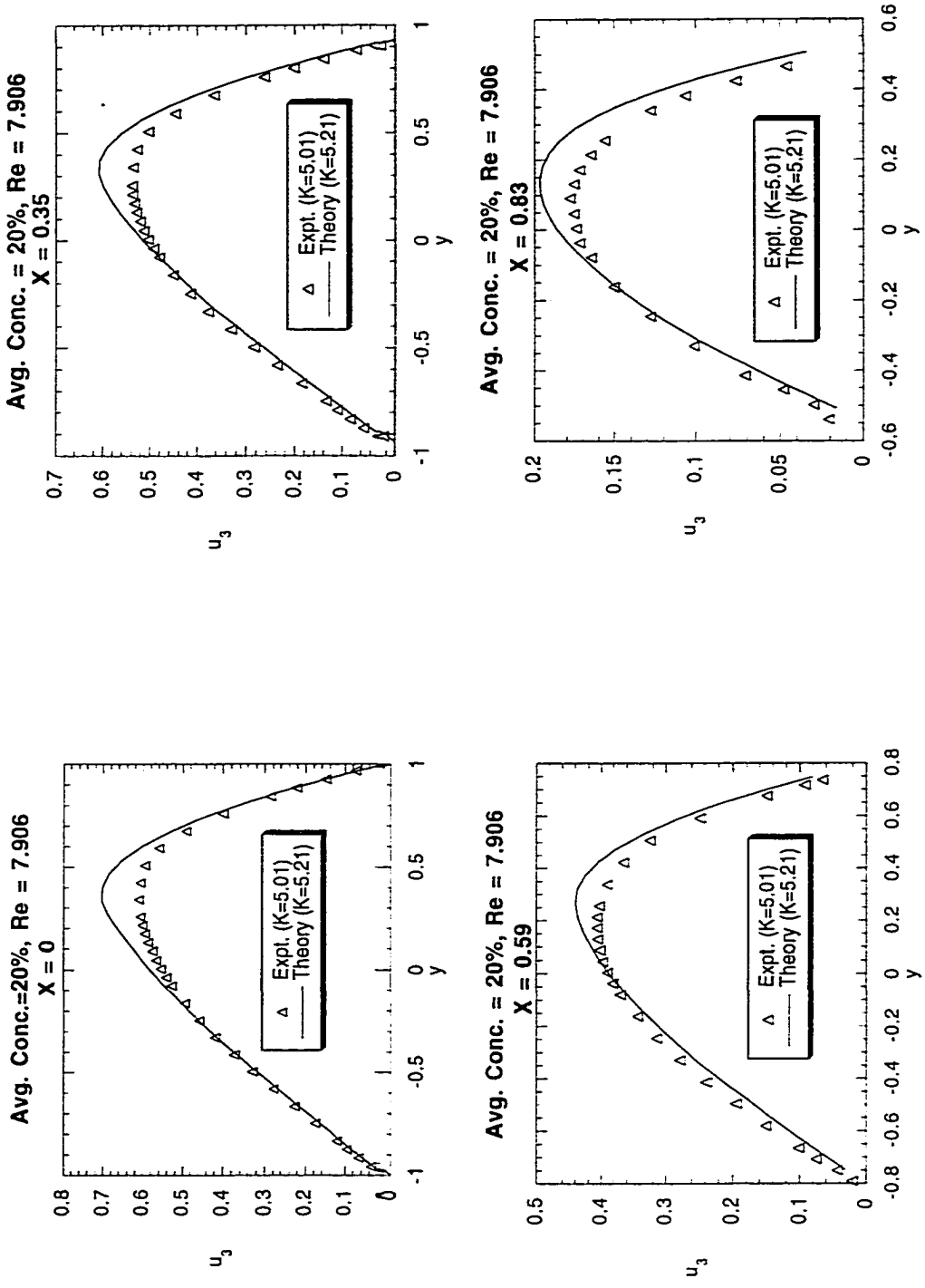

Figure 1.17: This figure shows the comparison of the experimental axial velocity profiles with theory at four cross-sections for the case of average concentration=20%, Re=7.91.

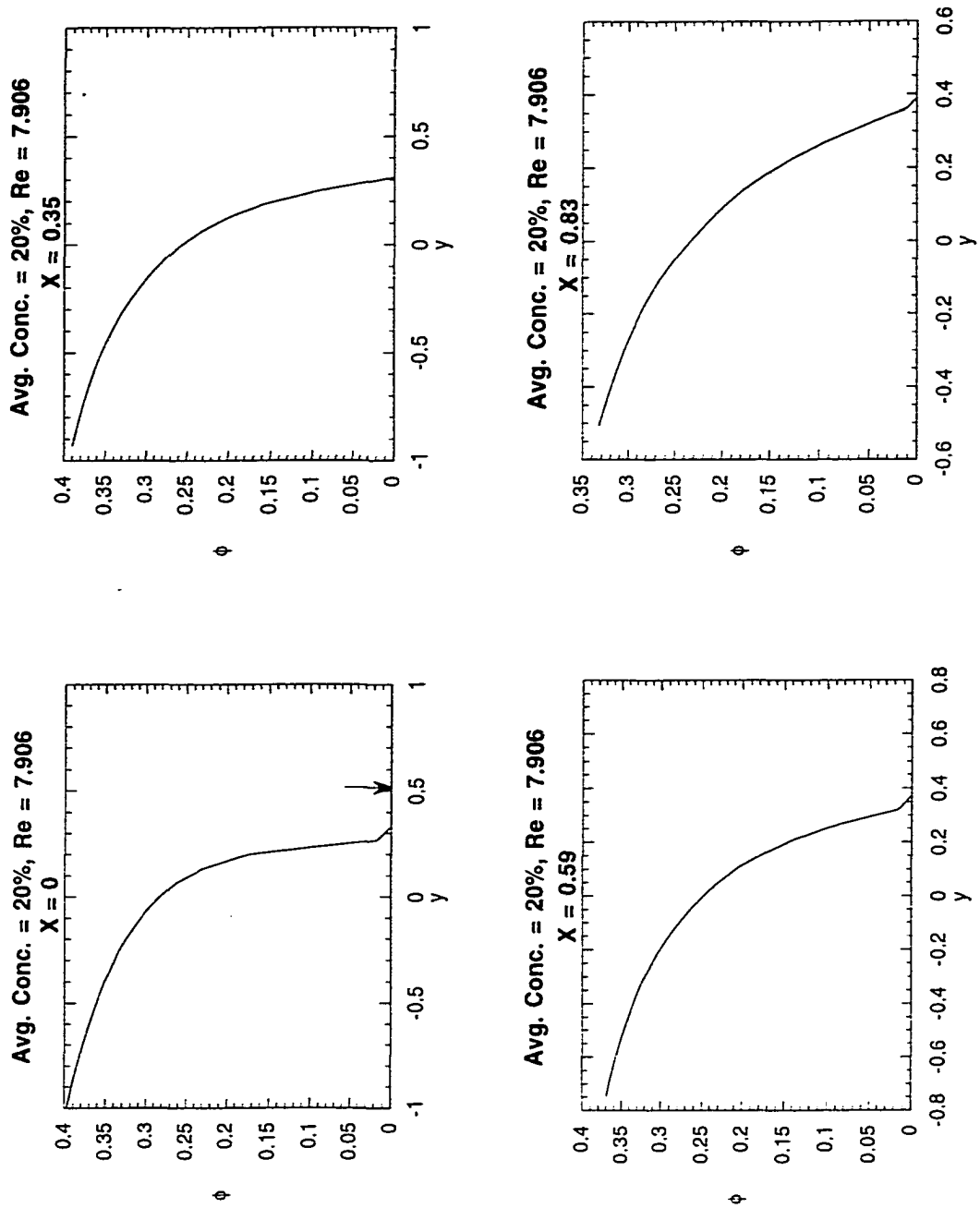

Figure 1.18: This figure shows the theoretically predicted concentration profiles at four cross-sections for the case of average concentration=20%, Re=7.91. The arrow shows the resuspension height observed experimentally.

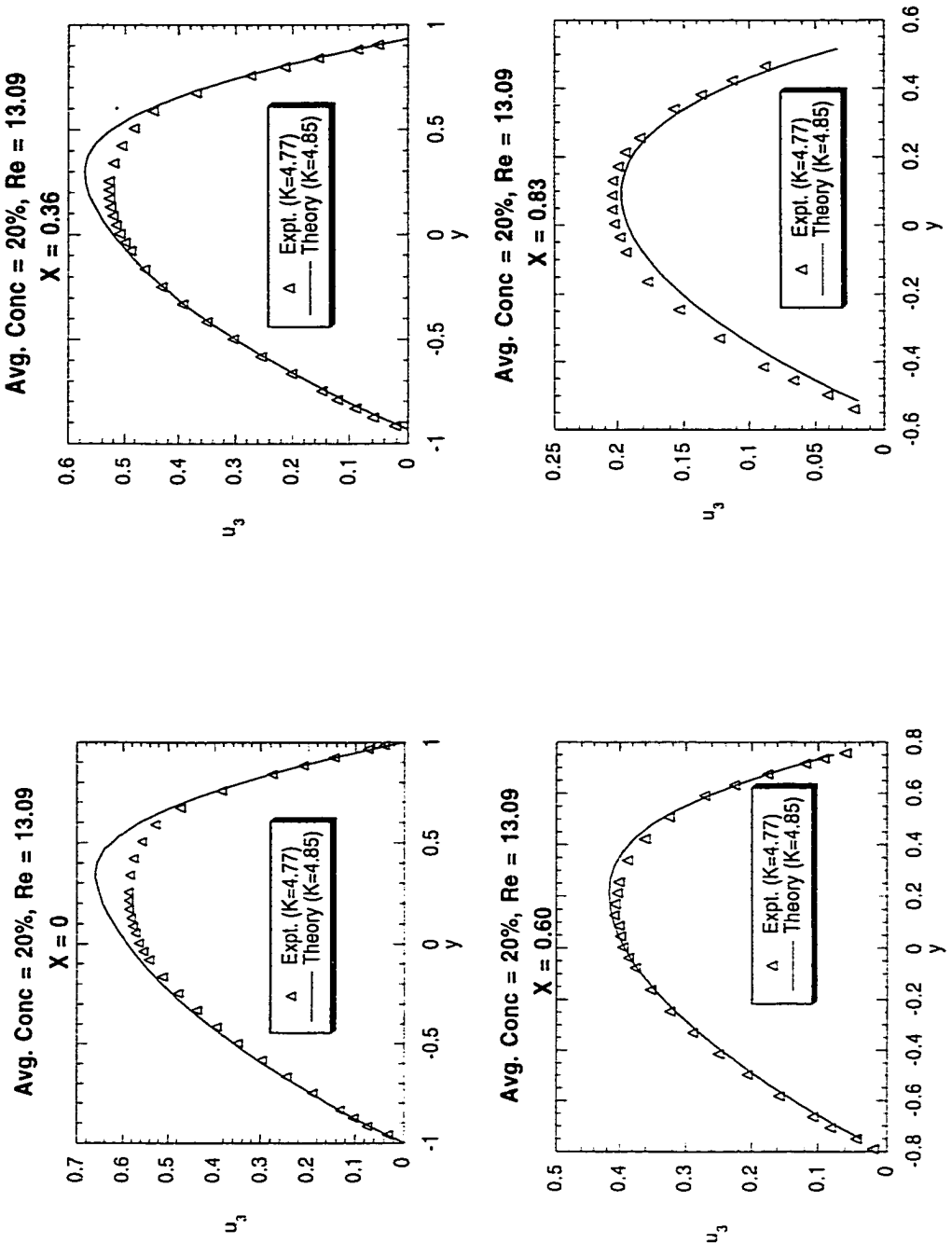

Figure 1.19: This figure shows the comparison of the experimental axial velocity profiles with theory at four cross-sections for the case of average concentration=20%, Re=13.09.

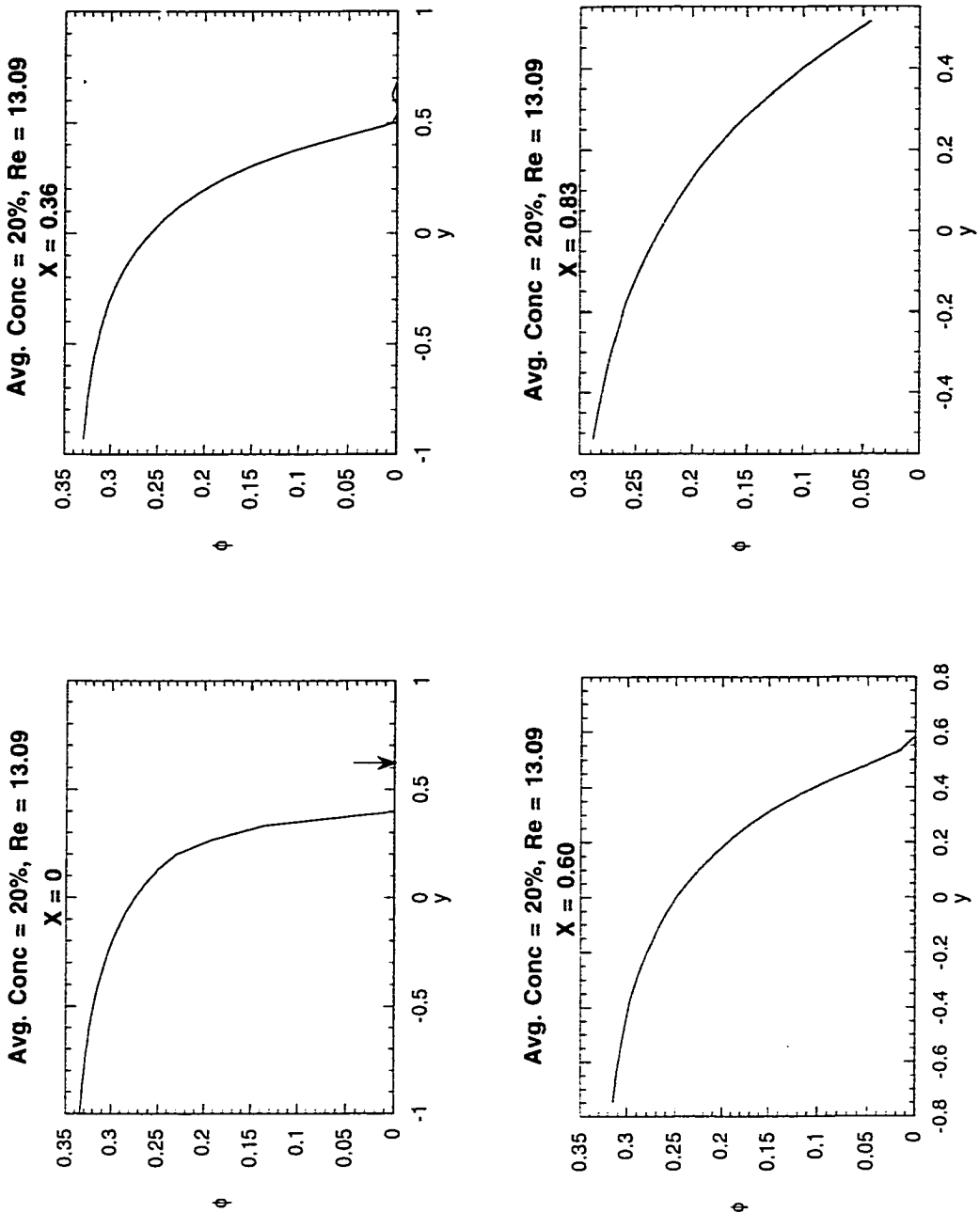

Figure 1.20: This figure shows the theoretically predicted concentration profiles at four cross-sections for the case of average concentration=20%, Re=13.09. The arrow shows the resuspension height observed experimentally.

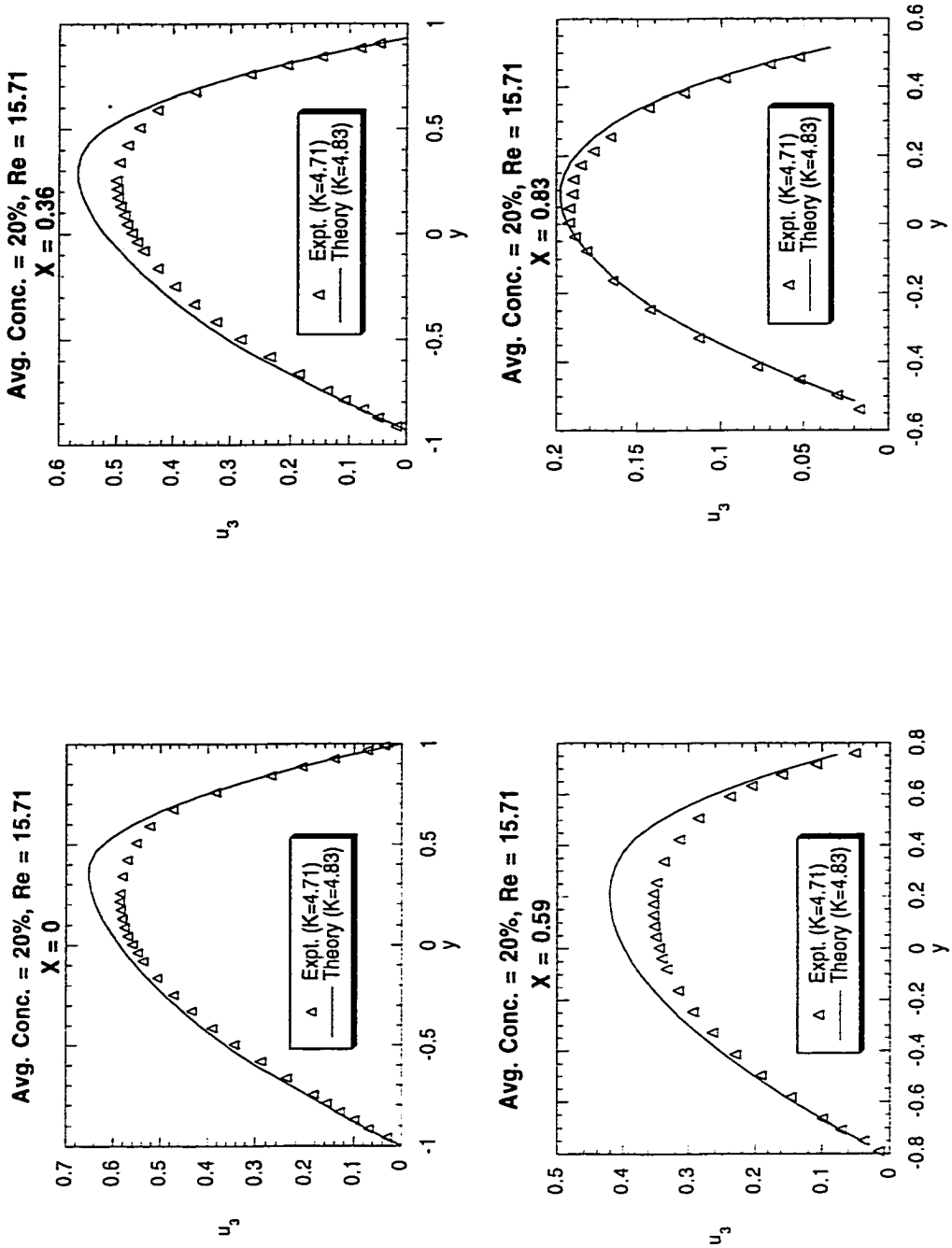

Figure 1.21: This figure shows the comparison of the experimental axial velocity profiles with theory at four cross-sections for the case of average concentration=20%, Re=15.71.

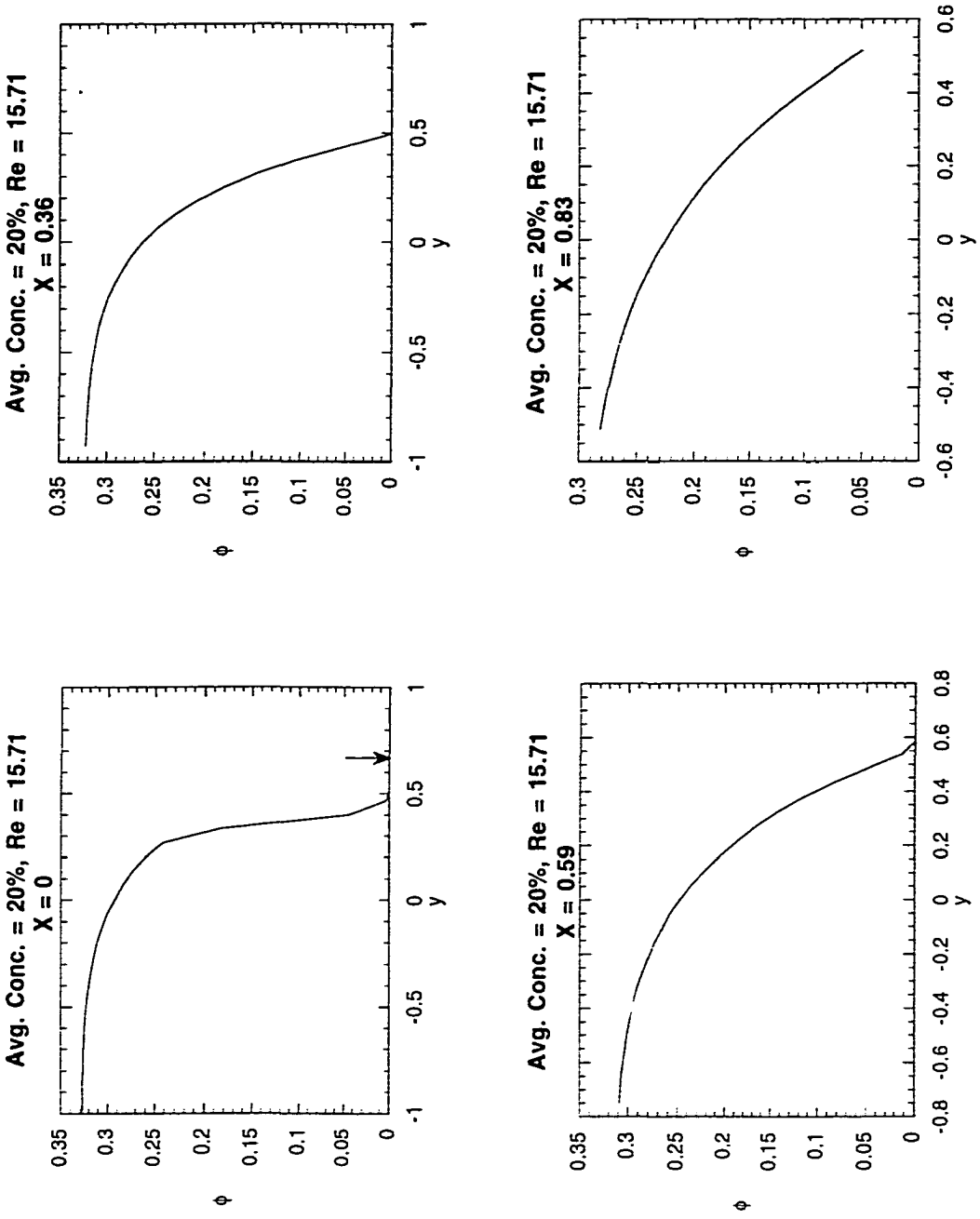

Figure 1.22: This figure shows the theoretically predicted concentration profiles at four cross-sections for the case of average concentration=20%, Re=15.71. The arrow shows the resuspension height observed experimentally.

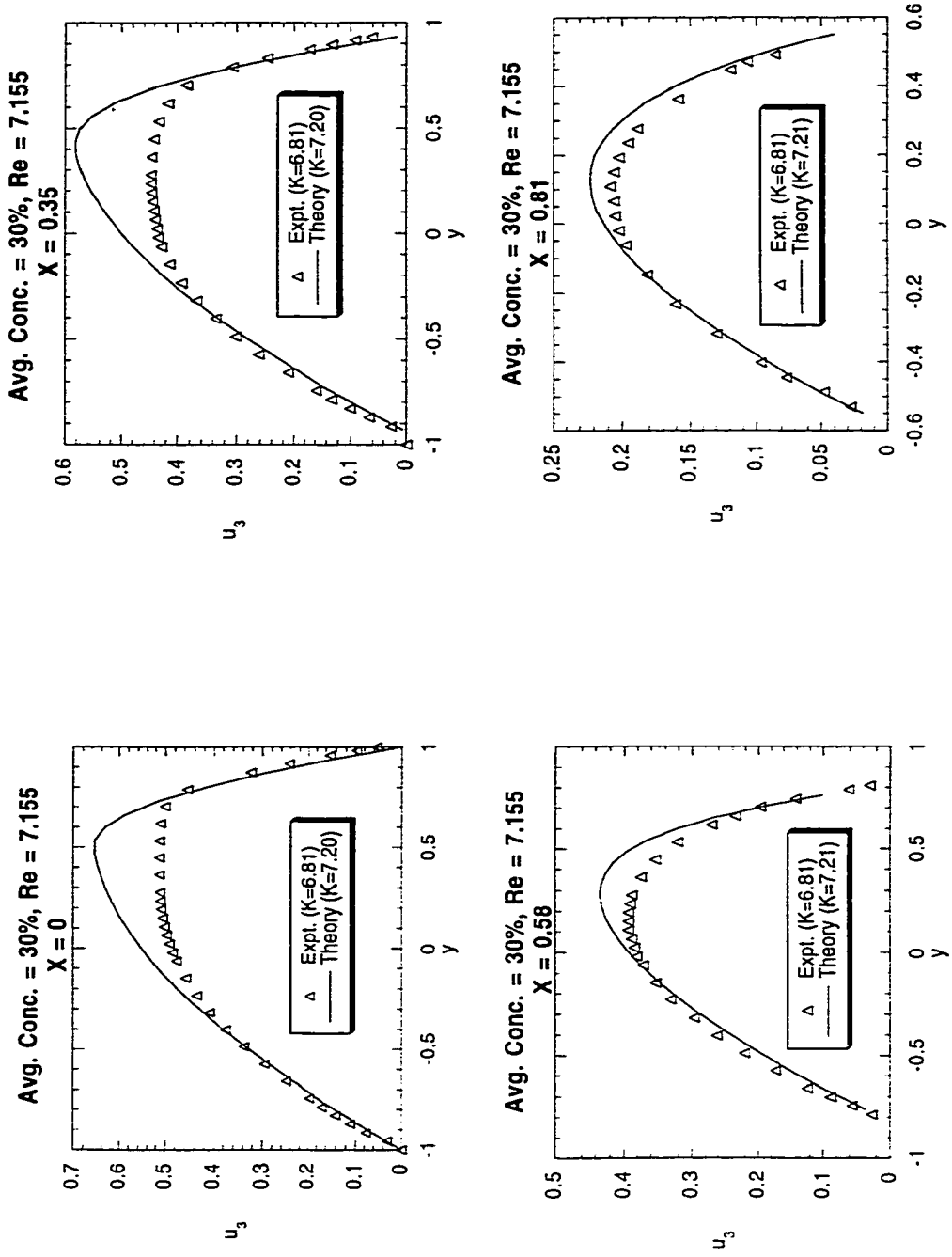

Figure 1.23: This figure shows the comparison of the experimental axial velocity profiles with theory at four cross-sections for the case of average concentration=30%, Re=7.16.

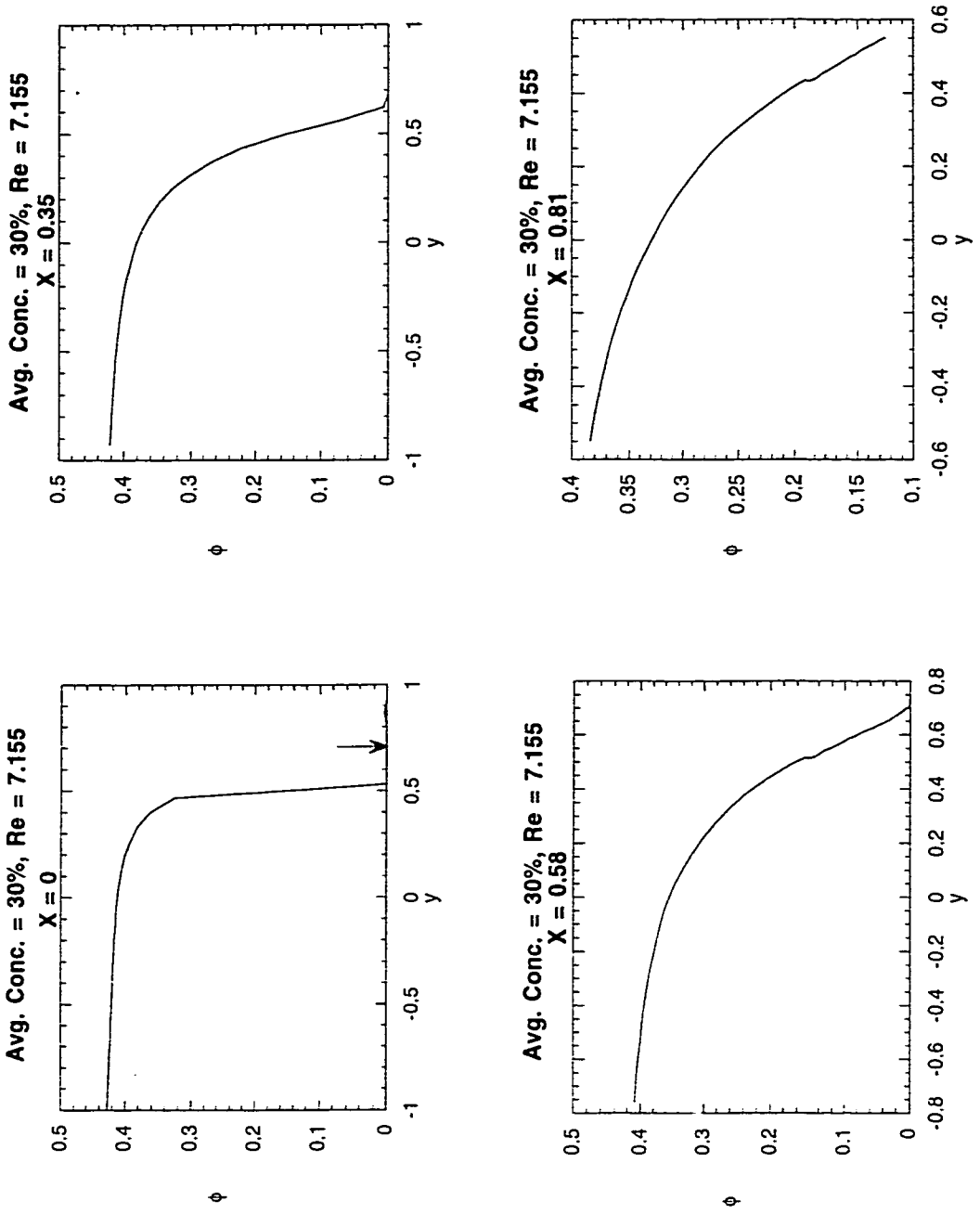

Figure 1.24: This figure shows the theoretically predicted concentration profiles at four cross-sections for the case of average concentration=30%, Re=7.16. The arrow shows the resuspension height observed experimentally.

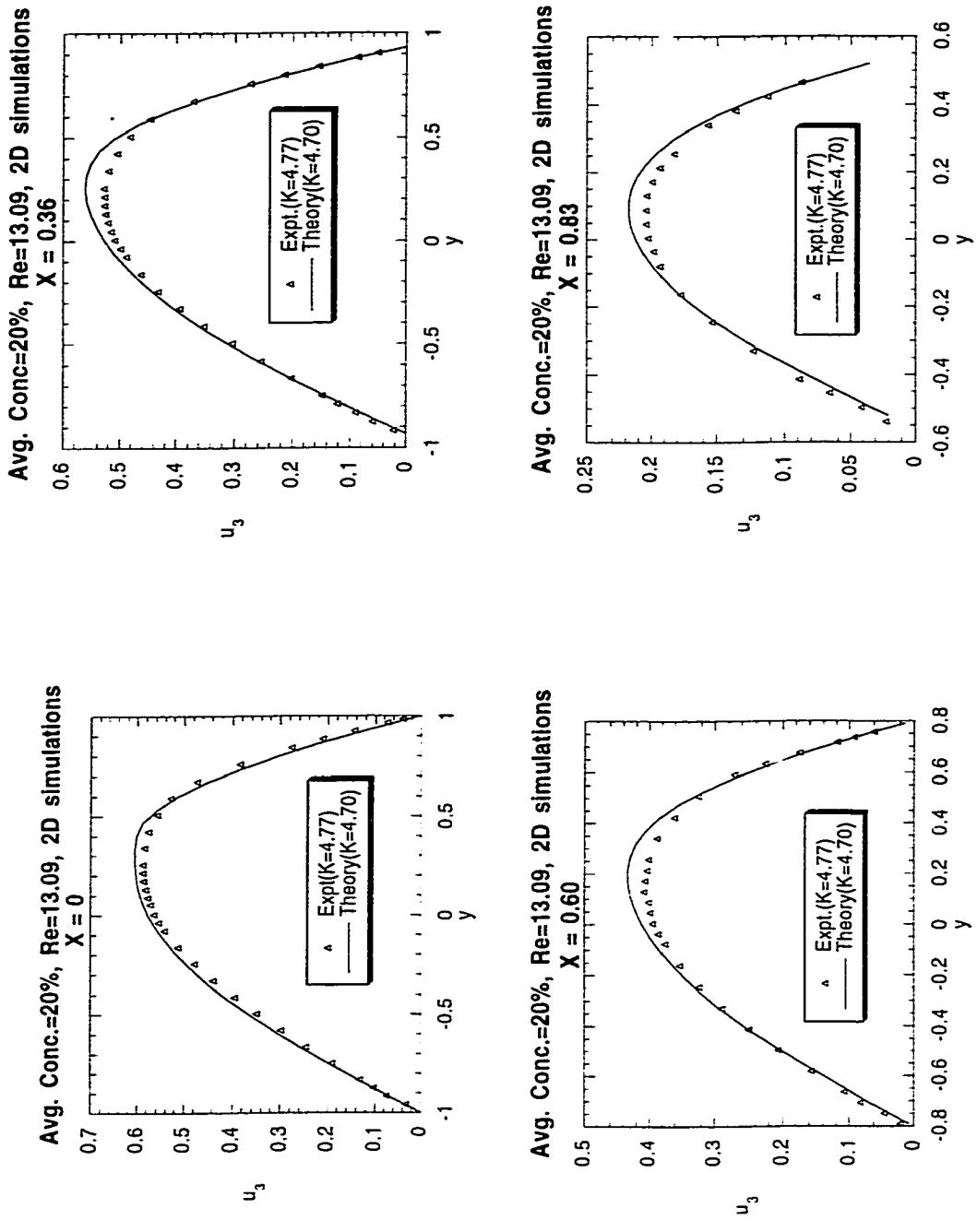

Figure 1.25: This figure shows the comparison of the experimental axial velocity profiles with theory at four cross-sections for the case of average concentration=20%, Re=13.09. Here the 2D equations have been solved

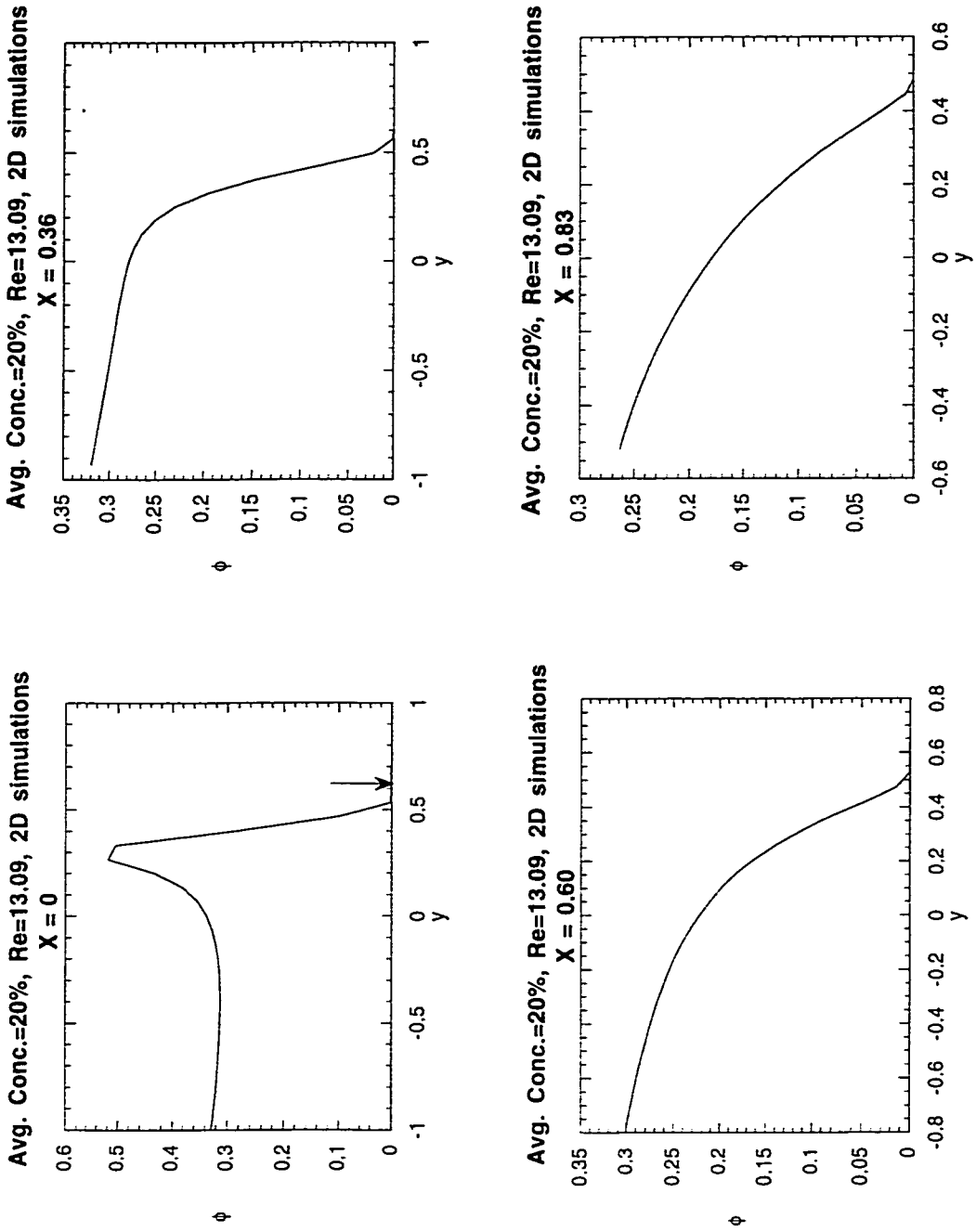

Figure 1.26: This figure shows the theoretically predicted concentration profiles at four cross-sections for the case of average concentration=20%, Re=13.09. Here the 2D equations have been solved. The arrow shows the resuspension height observed experimentally.

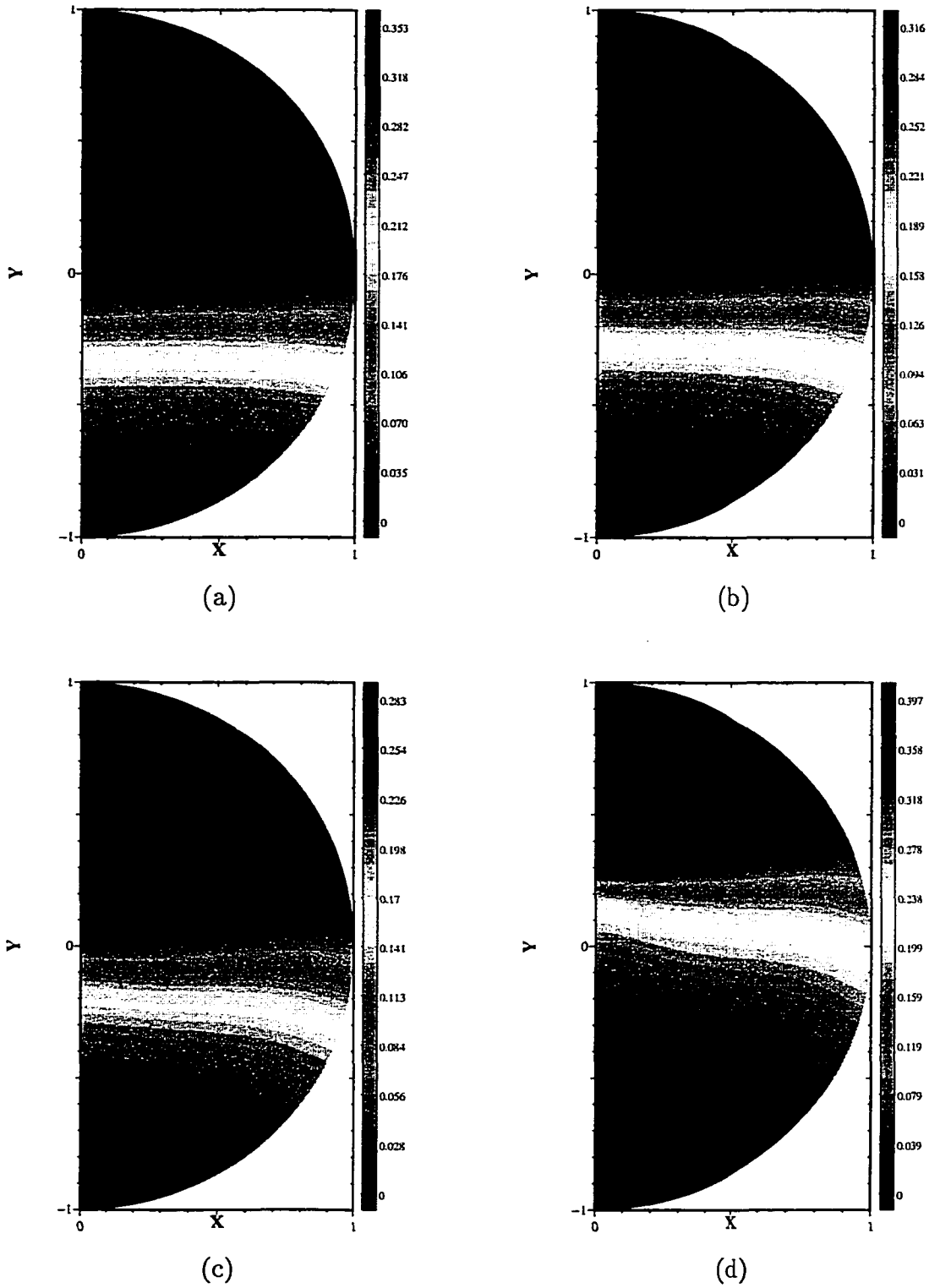

Figure 1.27: The theoretically predicted concentration profiles (3D time-dependent formulation) for (a) $\bar{\Phi} = 10\%$, $Re = 8.0$, $Fr = 0.27$ (b) $\bar{\Phi} = 10\%$, $Re = 12.5$, $Fr = 0.42$ (c) $\bar{\Phi} = 10\%$, $Re = 16.6$, $Fr = 0.56$ and (d) $\bar{\Phi} = 20\%$, $Re = 7.9$, $Fr = 0.27$.

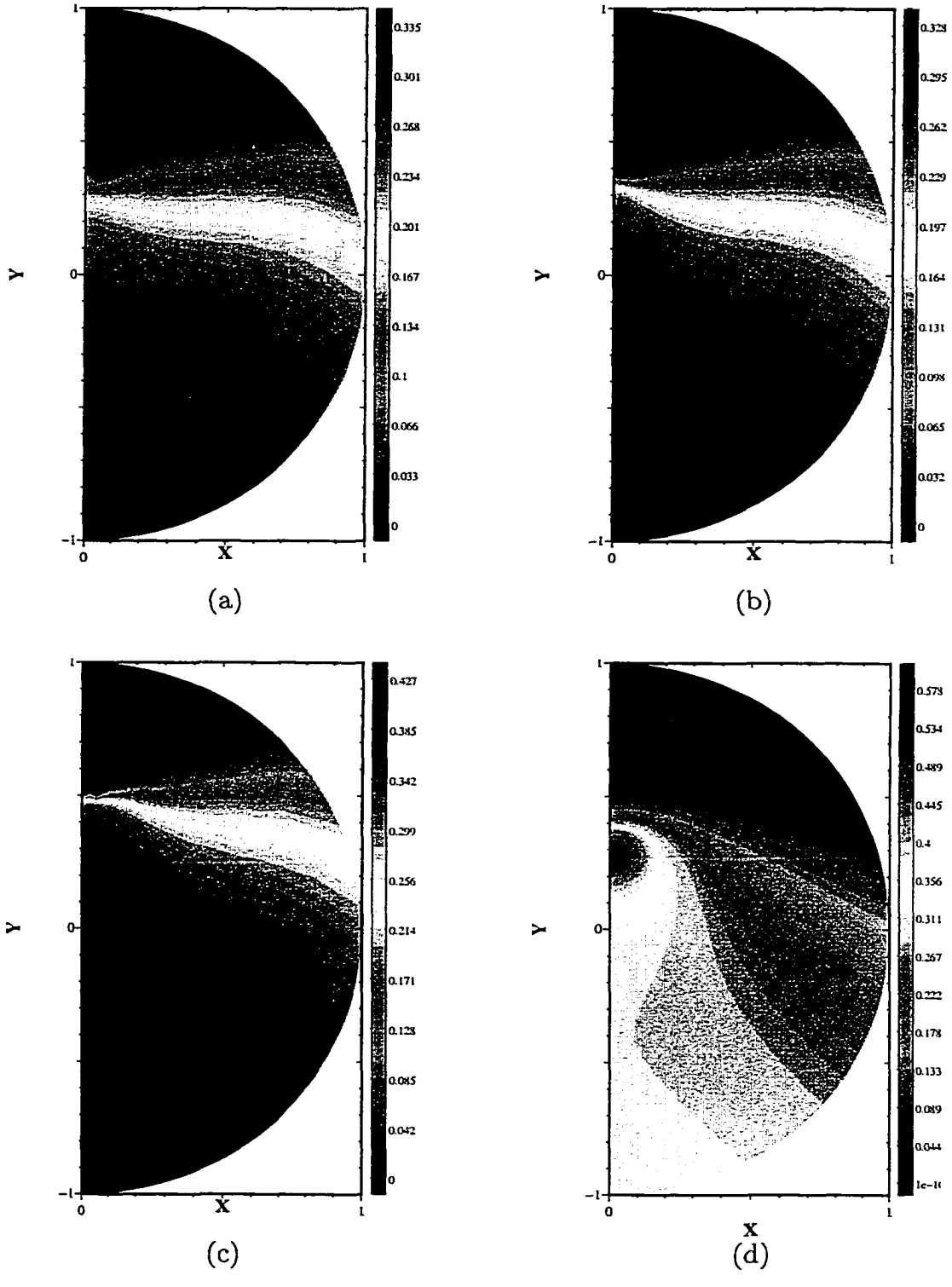

Figure 1.28: The theoretically predicted concentration profile (time-dependent formulation) for (a) $\bar{\Phi} = 20\%$, $Re = 13.1$, $Fr = 0.44$ (3D), (b) $\bar{\Phi} = 20\%$, $Re = 15.7$, $Fr = 0.53$ (3D), (c) $\bar{\Phi} = 30\%$, $Re = 7.2$, $Fr = 0.24$ (3D), and (d) $\bar{\Phi} = 20\%$, $Re = 13.1$, $Fr = 0.44$ (2D).

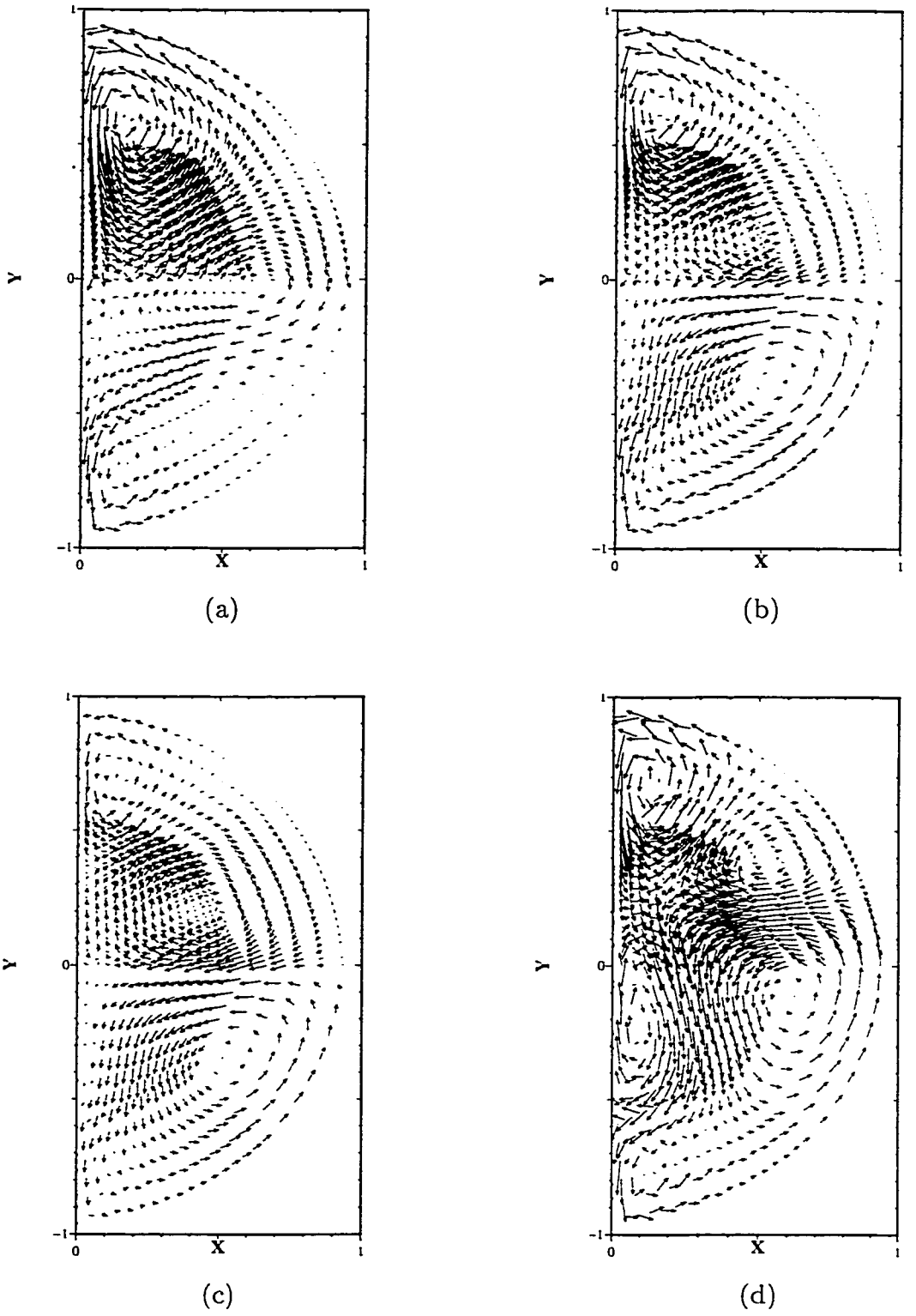

Figure 1.29: Secondary flow profile (3D time-dependent formulation) for (a) $\bar{\Phi} = 10\%$, $Re = 8.0$, $Fr = 0.27$ (b) $\bar{\Phi} = 10\%$, $Re = 12.5$, $Fr = 0.42$ (c) $\bar{\Phi} = 10\%$, $Re = 16.6$, $Fr = 0.56$ and (d) $\bar{\Phi} = 20\%$, $Re = 7.9$, $Fr = 0.27$.

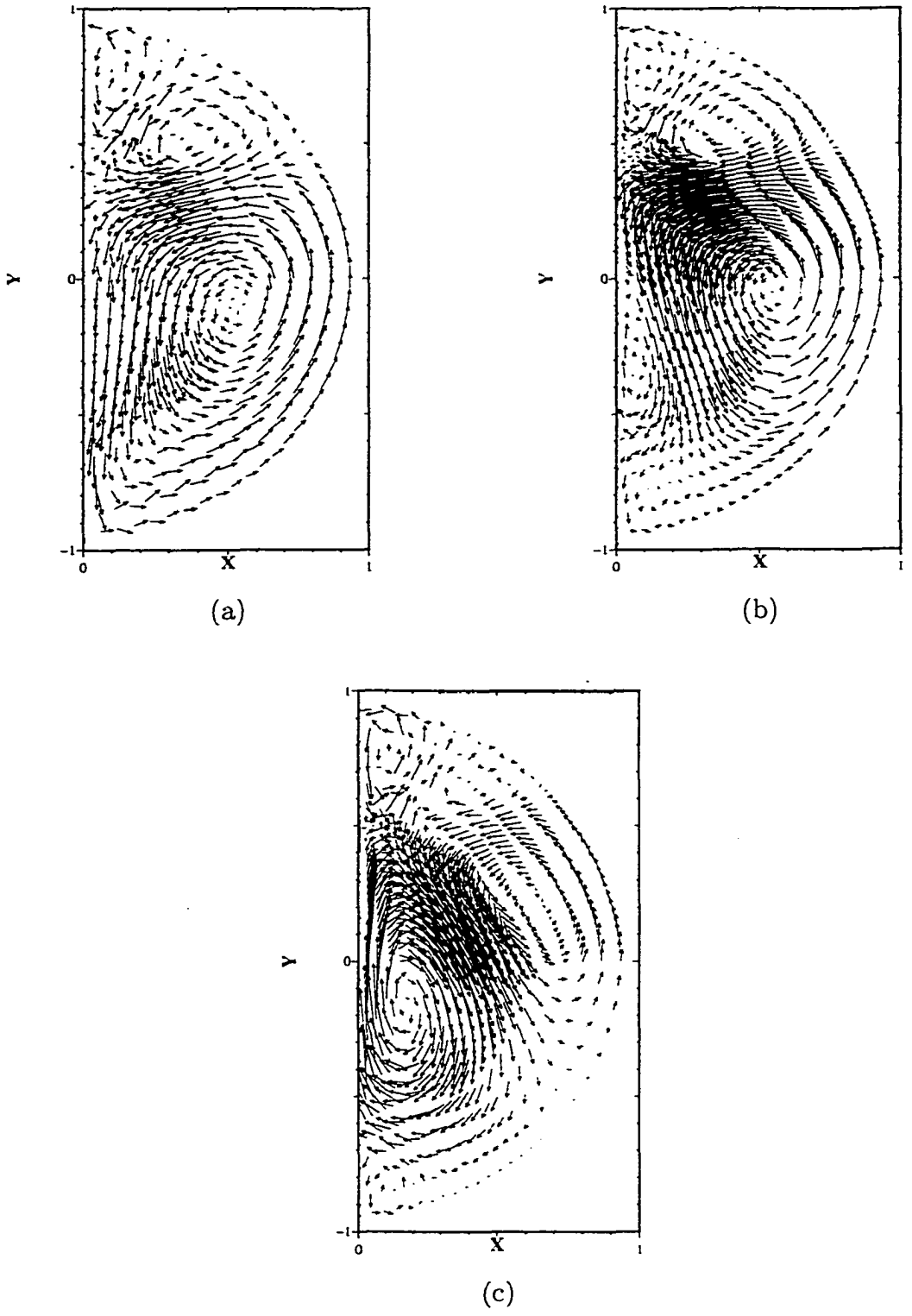

Figure 1.30: Secondary flow profile (3D time-dependent formulation) for (a) $\bar{\Phi} = 20\%$, $Re = 13.1$, $Fr = 0.44$. (b) $\bar{\Phi} = 20\%$, $Re = 15.7$, $Fr = 0.53$. (c) $\bar{\Phi} = 30\%$, $Re = 7.2$, $Fr = 0.24$.

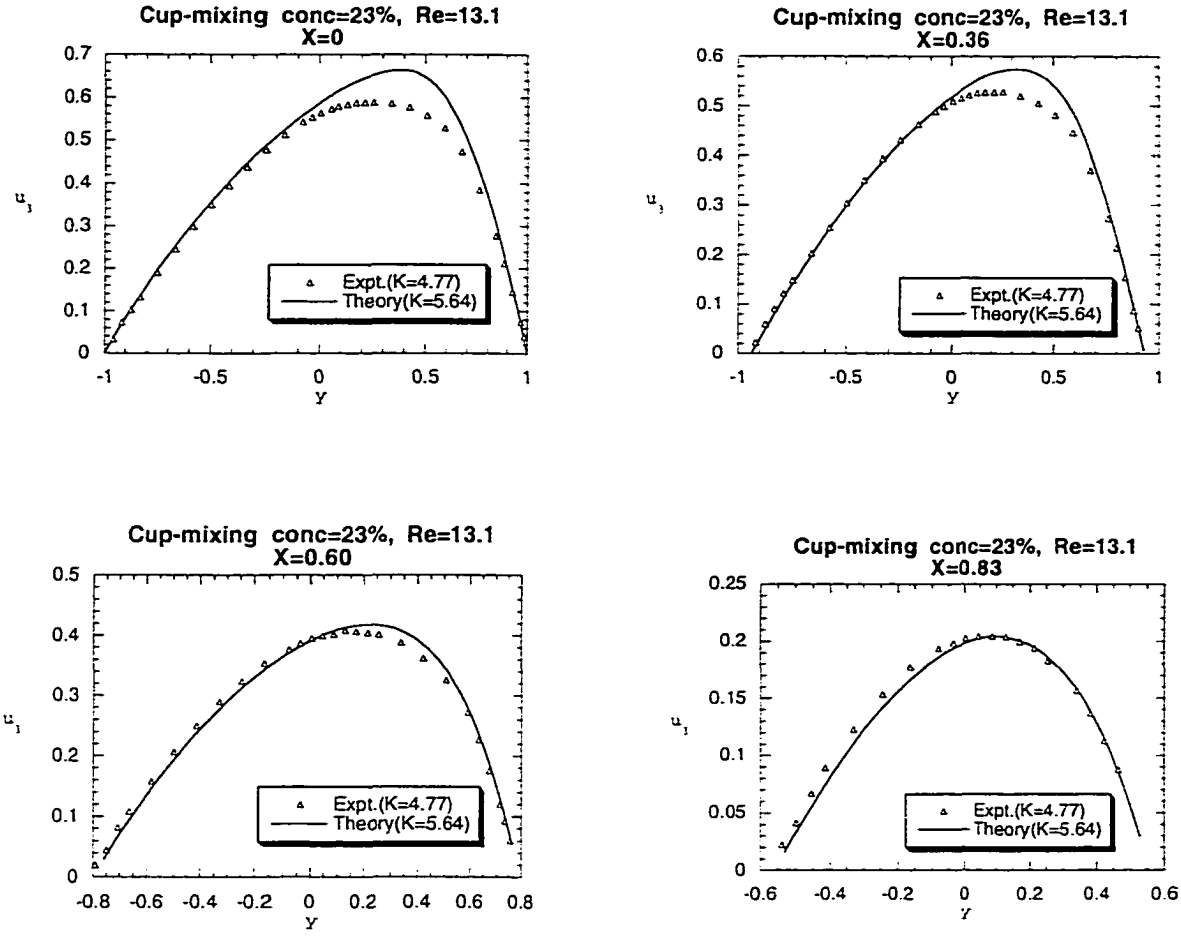

Figure 1.31: This figure shows the comparison of the experimental axial velocity profiles with theory at four cross-sections for the case of the cup-mixing concentration=23%, Re=13.09. Here the cup-mixing formulation has been used and solved.

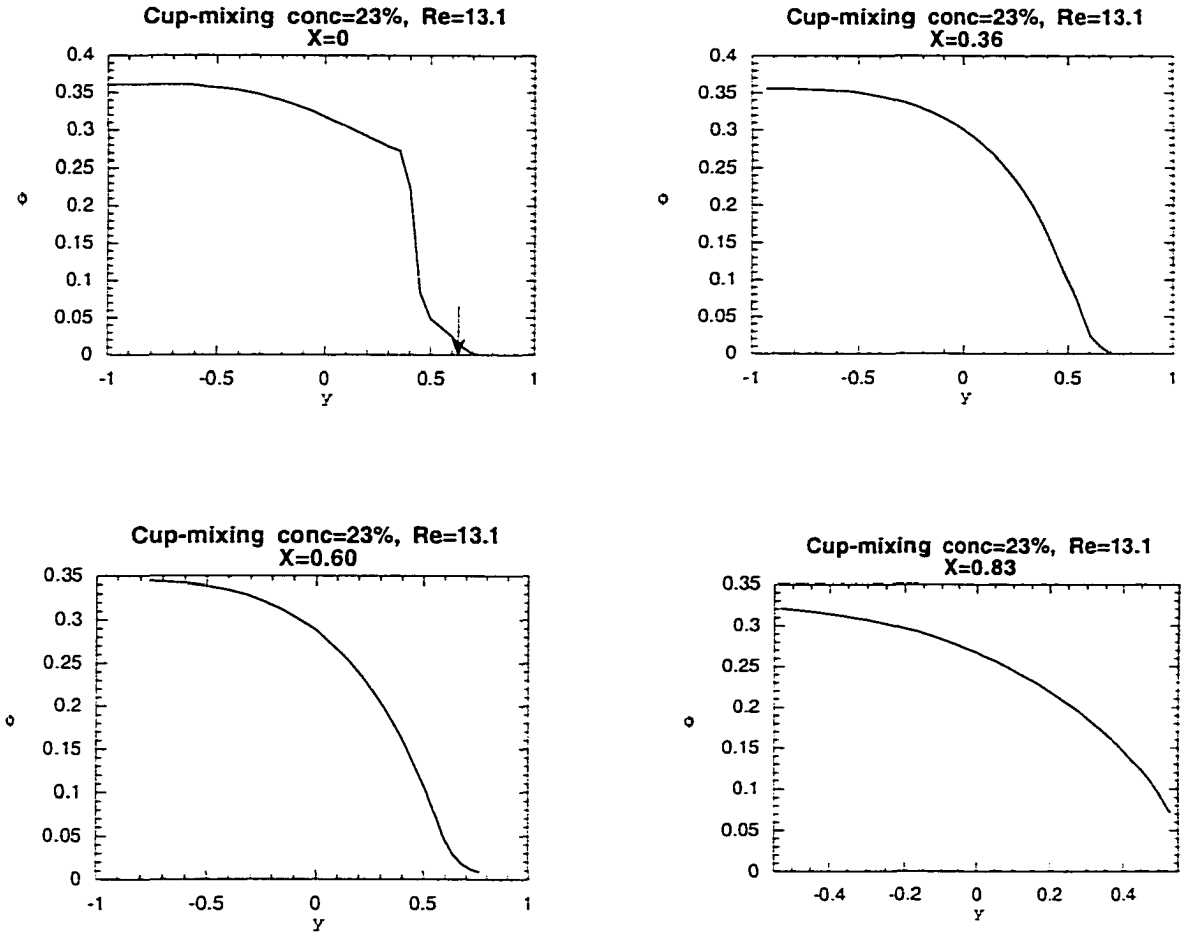

Figure 1.32: This figure shows the theoretically predicted concentration profiles at four cross-sections for the case of the cup-mixing concentration=23%, Re=13.09. Here the cup-mixing formulation has been used and solved. The arrow shows the resuspension height observed experimentally.

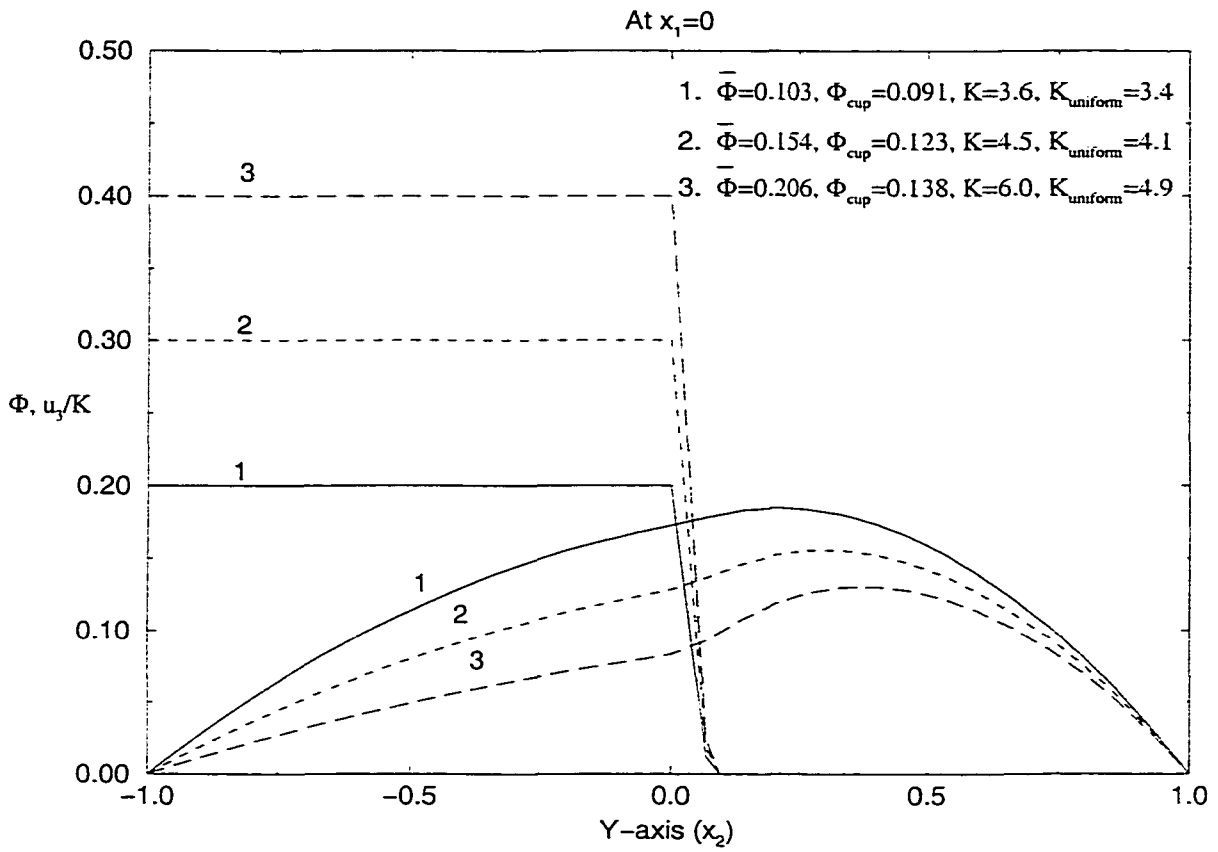

Figure 1.33: This figure presents the computed normalised axial velocity profiles and the corresponding step concentration profiles for average concentrations ($\bar{\Phi}$) of 10.3%, 15.4% and 20.6%. Here, K is the computed non-dimensional pressure gradient and $K_{uniform}$ represents the pressure gradient obtained on solving Poiseuille flow equation (uniform particle concentration) for the same average concentrations.

Chapter 2

Coating flows within a rotating horizontal cylinder: Lubrication analysis, numerical computations and experimental measurements

Abstract

We consider the flow within a rotating horizontal cylinder containing a small amount of a very viscous liquid which completely coats the cylinder surface. We show that, under creeping flow conditions, the addition of the hydrostatic pressure term to the standard lubrication equation leads to film thickness profiles which, over a broad range of parameters, are in close agreement with those obtained experimentally, as well as via the solution to the full Stokes equations (see also Tirumkudulu & Acrivos ([24])).

2.1 Introduction

Coating flows inside a rotating horizontal circular cylinder give rise to a variety of patterns which have been examined by numerous investigators([25]-[32]). Here we consider the special case of steady flows in which gravity is balanced by viscous forces, with inertia and surface tension effects being negligible ([32]-[35]). Under these conditions, the number of independent dimensionless groups reduce to two, viz. the fill ratio F, i.e. the ratio of total volume of liquid to the volume of the cylinder, and $\alpha \equiv (\Omega\nu/gR)^{1/2}$, where Ω is the angular velocity of the rotating cylinder, R is its radius, ν is the kinematic viscosity of the liquid and g is the gravitational constant. Furthermore, if $F \ll 1$, the film thickness profile $h(\theta)$, where θ refers to the angular coordinate (cf. fig 1), is small everywhere compared to R, hence the equations of motion simplify using standard lubrication theory. The solution([32]-[36]) of the corresponding momentum equation along the θ direction,

$$\frac{\partial^2 v}{\partial z^2} - \cos\theta = 0 \tag{2.1}$$

gives then the first approximation to the velocity profile,

$$v = 1 - \left(\eta z - \frac{z^2}{2}\right)\cos\theta \tag{2.2}$$

where v is the velocity component along θ rendered dimensionless with ΩR. Also,

$$\eta \equiv \frac{h}{R\alpha} \text{ and } z \equiv \frac{R-r}{R\alpha}, \tag{2.3}$$

with r being the radial coordinate. This expression for v satisfies no slip at $z = 0$ and, to first order in the lubrication analysis, the zero shear stress condition at $z = \eta$.

On integrating v across the film we therefore obtain that.

$$q = \eta - \frac{\eta^3}{3}\cos\theta \tag{2.4}$$

where $q \equiv \int_0^\eta v\,\mathrm{d}z = Q/\Omega R^2\alpha$ with Q being the total volumetric flow rate within the film per unit axial distance. At steady state, the dimensionless flow rate q is, of course, independent of θ but its value is unknown a priori. The remaining condition arises from the requirement that the volume of liquid be conserved. In the thin film approximation this becomes,

$$F = \frac{1}{\pi R}\int_{-\pi}^{\pi} h(\theta)\,\mathrm{d}\theta \equiv \alpha\beta \text{ where } \beta \equiv \frac{1}{\pi}\int_{-\pi}^{\pi}\eta\,\mathrm{d}\theta \tag{2.5}$$

hence, in this case, the initially two independent parameters, F and α, combine into one, viz. $\beta \equiv F/\alpha$, the value of which implicitly determines q and, therefore, the dimensionless film thickness profile $\eta(\theta)$.

Equation (2.4), subject to (2.5), has already been studied in detail by several investigators ([32]-[36]), who have shown that, if $0 < q < 2/3$, the cubic equation (2.4) has only one root $\eta(\theta)$ which is everywhere real and positive. A typical such profile, which is symmetric about $\theta = 0$ with $\eta'(0) = 0$, where $\eta' \equiv \mathrm{d}\eta/\mathrm{d}\theta$, is shown schematically in fig.1(a) and an example of such a profile obtained by solving eq.(2.4) for $q = 0.6275(\beta = 1.3009)$ is shown in fig.2. When $q = 2/3$, a symmetric continuous profile still exists, also shown in fig.2, with, however, a discontinuous slope at the origin, $\eta'(0) = \pm 1/\sqrt{6}$. The corresponding value of β equals 1.4142. When $q > 2/3$, none of the roots of equation (2.4) are physically acceptable in the sense of being everywhere real and positive. Also, for $q = 2/3$ and $\beta > 1.4142$, no continuous profile exists satisfying equations (2.4) and (2.5). On the other hand since, for $q = 2/3$, two of the roots of eq.(2.4) are positive in the interval $-\pi/2 < \theta \leq 0$ and coincide at $\theta = 0$, we can construct ([32],[34],[35]) an asymmetric discontinuous solution by following the symmetric profile from $\theta = \pi$ to $\theta = 0$, continuing along the larger of the two roots from $\theta = 0$ to $\theta = \theta^*$, where $-\pi/2 < \theta^* < 0$, and then reverting back to the symmetric profile from $\theta = \theta^*$ to $\theta = -\pi$, with θ^* being determined implicitly by the given value of β. Such a discontinuous profile is

shown schematically in fig.1(b) and an example of such a profile obtained by solving eqs (2.4) & (2.5) for $\theta^* = -\pi/4$, corresponding to $\beta = 1.5$, is shown in fig.2. (In principle, there exists a similar asymmetric solution of equations (2.4) and (2.5), with the discontinuity being located at $0 < \theta^* < \pi/2$, but the resulting thickness profile is unstable ([32]) on mathematical as well as, obviously, physical grounds). When $\theta^* = -\pi/2$, corresponding to $\beta = 2.2135$, the film thickness becomes unbounded but integrable as $\theta \to -(\pi/2)+$ and is of the form ([32]),

$$\eta \to \left(\frac{3}{\frac{1}{2}\pi + \theta}\right)^{\frac{1}{2}} - \frac{1}{3} + \mathcal{O}\left(\left[\frac{1}{2}\pi + \theta\right]^{\frac{1}{2}}\right).$$

When $\beta > 2.2135$, no physically acceptable solution to equations (2.4) and (2.5) can be shown to exist.

The origin of the breakdown of the lubrication analysis as β approaches this second critical value 2.2135 becomes apparent when one examines the streamlines according to equation (2.2). It can be shown that, in the range $1.5862 < \beta < 2.2135$, eq.(2.2) predicts that a region of reverse flow, or puddle, will exist near the bottom of the cylinder containing that portion of the liquid which cannot be carried over along the ascending part of the flow beyond $\theta = 0$. Recall that, according to the lubrication analysis and as also seen in fig.2, outside the range $\theta^* < \theta < 0$, where $-\pi/2 < \theta^* < 0$, the dimensionless film thickness and, consequently, the dimensionless velocity profiles remain independent of β when the latter exceeds 1.4142. Moreover, since this region of reverse flow will increase in size with an increase in β which, for a given α, corresponds to an increase in the filling fraction F, one should expect that, eventually, the region would extend in the negative θ-direction beyond $\theta = -\pi/2$. But this cannot happen according to equation (2.2) because v is everywhere positive when θ lies outside the range $-\pi/2 \leq \theta \leq 0$. It is clear therefore that, in order to overcome this limitation of the analysis referred to above, the expression for v should include another term which will remain negative

when θ falls below $-\pi/2$.

The purpose of this paper is to show that, by means of a simple modification to equation (2.1), we are able to capture all the salient features of this problem and to obtain film thickness profiles in close agreement with those obtained both experimentally as well as via the numerical solution to the full Stokes equations over the whole range of β.

2.2 A simple extension to the lubrication analysis

It is apparent on physical grounds that the discontinuous increase with increasing θ in the thickness profile across θ^*, predicted by the lubrication analysis for $\beta > 1.4142$, creates a corresponding positive jump in the hydrostatic pressure within the film at a given value of z. Consequently, the existence of a positive, and in fact infinite, pressure gradient along θ is thereby predicted which will enhance the strength of the reverse flow. To see whether this suffices to allow the puddle to extend beyond $\theta = -\pi/2$ (in the negative θ direction) we therefore consider the expression for the pressure which, to leading order in the thin film approximation is still hydrostatic,

$$p = \alpha(z - \eta)\sin\theta \tag{2.6}$$

where p refers to the pressure rendered dimensionless with $\rho g R$ with ρ being the density of the liquid. When equation (2.6), which corresponds to the exact expression for the dimensionless hydrostatic pressure, is inserted into the θ-momentum equation of the lubrication theory (which, in addition to the terms in eq.(2.1), now contains the θ-component of ∇p) it gives rise to two additional terms : a term $-\alpha(z-\eta)\cos\theta/(1-\alpha z)$, which modifies the leading order gravitational term $-\cos\theta$, and a second term, $\alpha\eta'\sin\theta/(1-\alpha z)$ which can become particularly significant, even if α is small, in regions where η' is large. Consequently the sum of the component of the gravitational term in the θ-direction minus the corresponding θ component

of ∇p becomes

$$-\frac{1}{1-\alpha z}\{(1-\alpha\eta)\cos\theta - \alpha\eta'\sin\theta\}$$

which, as we shall see below, vanishes exactly for any F, as it should, when the fluid is stagnant. On substituting the above in the θ-momentum balance equation (cf. equation (2.1)), we therefore obtain, in the thin film approximation $\alpha\eta \equiv h/R \ll 1$,

$$v = 1 - \left(\eta z - \frac{z^2}{2}\right)\{(1-\alpha\eta)\cos\theta - \alpha\eta'\sin\theta\} \tag{2.7}$$

in lieu of equation (2.2), as well as

$$q = \eta - \frac{1}{3}\eta^3\{(1-\alpha\eta)\cos\theta - \alpha\eta'\sin\theta\} \tag{2.8}$$

which replaces equation (2.4). Also the exact condition of volume conservation becomes

$$F = \frac{1}{\pi R}\int_{-\pi}^{\pi} h(\theta)\,\mathrm{d}\theta - \frac{1}{2\pi R^2}\int_{-\pi}^{\pi} h^2\mathrm{d}\theta \tag{2.9}$$

from which it follows that

$$\beta \equiv \frac{F}{\alpha} = \frac{1}{\pi}\int_{-\pi}^{\pi}\eta\,\mathrm{d}\theta - \frac{\alpha}{2\pi}\int_{-\pi}^{\pi}\eta^2\mathrm{d}\theta \tag{2.10}$$

Clearly, in the thin film approximation $h/R \ll 1$, equation (2.9) and, therefore, equation (2.10) reduces to equation (2.5).

We note parenthetically that eq.(2.8) is similar to the expression

$$q = \eta - \frac{1}{3}\eta^3\cos\theta + \alpha\left\{\frac{1}{2}\eta^4\cos\theta - \frac{1}{2}\eta^2 + \frac{1}{3}\eta^3\eta'\sin\theta\right\} \tag{2.11}$$

obtained by Benjamin et. al([32]) (cf. also Hosoi and Mahadevan ([37])) by retaining all the $\mathcal{O}(\alpha)$ correction terms to the lubrication analysis and requiring that $Ca \gg \alpha^3$, where $Ca(\equiv \Omega R\mu/\sigma)$ is the capillary number, μ is the viscosity and σ is the surface tension. Hence, since eq.(2.8) cannot be derived from a formal perturbation expansion in α, it should be viewed as a model equation, albeit a very useful one as we shall see.

Before looking in more detail at the predictions of this extended lubrication analysis which now involves the two independent parameters α and F, rather than the single parameter $\beta \equiv F/\alpha$, it is instructive to examine the asymptotic structure of eq.(2.8), subject to (2.10), in the two limiting cases $\alpha \to \infty$ and $\alpha \to 0$ for fixed F.

In the former, the liquid is in solid body rotation and its thickness becomes independent of θ. In view of eq.(2.10), $F = 2H - H^2$, with $H \equiv h/R = \alpha\eta$, which is exact for any F. The same result of a constant film thickness and its relation to F is obtained from eq.(2.8) subject to eq.(2.10).

Turning next to the case $\alpha \to 0$, one might be tempted to construct([34]) an asymptotic solution to eq.(2.8) using the well-known technique of inner and outer expansions in which all terms of $\mathcal{O}(\alpha)$ are neglected to first order except for the term $\frac{1}{3}\alpha\eta^3\eta'\sin\theta$ within an inner $\mathcal{O}(\alpha)$ region near $\theta = \theta^*$ where the solution to the outer problem, eq.(2.4) with $q = 2/3$ and $\eta \sim \mathcal{O}(1)$, leads to a discontinuous change in η, at $\theta = \theta^*$, for $\beta > 1.4142$. This method fails in the present case, however, since, as was pointed out earlier, a physically acceptable solution to the outer equation no longer exists if $\alpha < F/2.2135$. In fact, as we shall see presently, even for the case of $\alpha > F/2.2135$, the solution of eqs.(2.8) & (2.10) differs from that of the standard lubrication equation over a region which is much greater than $\mathcal{O}(\alpha)$ and that, with decreasing α, this region widens, with the corresponding value of η becoming $\mathcal{O}(1/\alpha)$. The failure of this conventional approach is not surprising given that, as $\alpha \to 0$, which corresponds to large g and/or small Ω, one would expect that the major portion of the fluid would be confined to an almost stagnant puddle, symmetric about $\theta = -\pi/2$ and extending from $\theta = -\pi/2 - \phi$ to $\theta = -\pi/2 + \phi$ where, as seen below, ϕ is given implicitly by the value of F. Thus, we should anticipate that, as $\alpha \to 0$, and with $\eta \equiv H/\alpha$ as before, we should have that, to

leading order in α for F fixed and provided that $\phi < \pi/2 (F < 1/2)$,

$$H = 1 + \frac{\cos\phi}{\sin\theta} \qquad \text{for } -\frac{\pi}{2} - \phi < \theta < -\frac{\pi}{2} + \phi \tag{2.12}$$

and $H = \mathcal{O}(\alpha)$ otherwise, where ϕ is given implicitly by

$$F = \frac{1}{\pi} \int_{-\pi/2}^{-\pi/2+\phi} \left(1 - \frac{\cos^2\phi}{\sin^2\theta}\right) \mathrm{d}\theta = \frac{1}{\pi} \left(\phi - \frac{1}{2}\sin 2\phi\right) \tag{2.13}$$

For $\phi > \pi/2 (F > 1/2)$, eq. (2.12) becomes,

$$H = 1 - \frac{\cos\phi}{\sin\theta} \qquad \text{for } \phi - \frac{\pi}{2} < \theta < \frac{3\pi}{2} - \phi \tag{2.14}$$

where again

$$F = \frac{1}{\pi} \left(\phi - \frac{1}{2}\sin 2\phi\right)$$

It is easy to show that, as $\alpha \to 0$, the solution to eq.(2.8), but not that of eq.(2.11), subject to (2.10) conforms to the exact expressions given above.

Thus, given that the solution of eq.(2.8) subject to (2.10) reduces to the exact asymptotic results as $\alpha \to \infty$, as well as $\alpha \to 0$, we would expect that the thickness profiles thereby computed over the whole range of α for given F which is fairly small, say $F \lesssim 0.15$, would be in close agreement with those obtained via the numerical solution of the full Stokes equations. As we shall see presently, this is indeed the case.

2.3 Numerical Procedure

Within the range of interest, $F \lesssim 0.15$ and $\beta > 1.4142$, α is 0.1 or less, hence, as already pointed out in [32], the numerical solution of the form of eq.(2.8), requires some care because the coefficient multiplying the highest derivative, in this case $\alpha/3$, is numerically very small. In addition, (2.8) is singular at $\theta = 0$ and at $\theta = \pm\pi$, which in turn precludes the use of a straightforward marching procedure

for integrating eq.(2.8) over the whole domain $-\pi < \theta < \pi$. Instead we found it convenient to expand $\eta(\theta)$ in a power series about the midpoint,

$$\eta(\theta) = \sum_{0}^{\infty} a_n \theta^n \tag{2.15}$$

which, when substituted into eq.(2.8) leads to recursion relations among the coefficients a_n that were obtained using Maple V software. The first three terms give

$$q = a_0 - \frac{1}{3}a_0^3 + \frac{\alpha}{3}a_0^4 \tag{2.16}$$

$$a_1 \left\{ 1 - a_0^2 + \frac{5\alpha}{3}a_0^3 \right\} = 0 \tag{2.17}$$

$$a_2 \left(1 - a_0^2 + 2\alpha a_0^3\right) - a_1^2(a_0 - 3\alpha a_0^2) + \frac{1}{6}a_0^3(1 - \alpha a_0) = 0 \tag{2.18}$$

In view of eq.(2.17), either $a_1 = 0$, which leads to the symmetric solution already discussed, or

$$1 - a_0^2 + \frac{5\alpha}{3}a_0^3 = 0 \qquad \text{with } a_1 \text{ left undetermined.}$$

Consequently, $a_0 = 1 + 5\alpha/6 + \mathcal{O}(\alpha^2)$ and, from eq.(2.16), $q = 2/3 + \alpha/3 + \mathcal{O}(\alpha^2)$. Also, because of eq.(2.18), $a_1 = \pm 1/\sqrt{6} + \mathcal{O}(\alpha)$ but since, as was said earlier, the branch of solutions corresponding to $a_1 > 0$ is unstable when $\theta > 0$, we shall take a_1 to be negative. We therefore proceeded as follows: For a given value of α, we let

$$a_1 = -\frac{1}{\sqrt{6}} - \epsilon$$

where ϵ is a positive $\mathcal{O}(\alpha)$ number, computed the first ten coefficients a_n of eq.(2.15), summed the series for a small value of θ, say θ_1, and, with $\eta(\theta_1)$ thus known, solved eq.(2.8) as an initial value problem for $\theta < 0$ if $\theta_1 < 0$ and for $\theta > 0$ if $\theta_1 > 0$. F was then calculated from eq.(2.10) for any α and ϵ.

We found that for a given value of $\alpha (\alpha \leq 0.1)$ the film profile in the region $0 \leq \theta \leq \pi$ remained essentially unchanged for different values of ϵ (or $\eta(\theta_1)$). For example, for $\alpha = 0.0333$, a change in the 2^{nd} decimal place in the value of ϵ resulted

in film profiles in which the numerical values of $\eta(\theta)$ differed in only the 6^{th} decimal place in the region $0 \leq \theta \leq \pi$. On the other hand, the profile for $\theta < 0$ was found to be very sensitive to the chosen value of ϵ. For example, for $\alpha = 0.0333$, a change in the 10^{th} decimal place in ϵ led to numerical values of $\eta(\theta)$ which differed by almost an order of magnitude somewhere within the interval $-\pi < \theta < 0$. This, however, is not surprising given the fact that, for a given α, the numerical value of the slope, and consequently the value of $\eta(\theta)$ (for $\theta < 0$), for different profiles($F \leq 0.15$) are almost identical close to $\theta = 0$. But far from $\theta = 0$ (in the negative θ-direction), the profiles $\eta(\theta)$ for different values of F vary significantly. As a result, for small α, we were forced to perform calculations with almost 20 floating point digits. In order to circumvent this difficulty in the region $-\pi < \theta < 0$, we therefore chose a value of $\eta(\theta_1)$, where θ_1 was far from $\theta = 0$, say $\theta_1 = -1.0$, solved eq.(2.8) and then obtained F from eq.(2.10).

We also solved the full two-dimensional Stokes equations using the NEKTON software (Fluent Inc.), for corresponding values of α and F. The time-dependent form of these equations is:

$$\frac{\partial u_i}{\partial t} = -\frac{\partial p}{\partial x_i} + \frac{\partial^2 u_i}{\partial x_k^2} + \frac{g_i}{g\alpha^2}, \quad \text{for } i = 1, 2 \tag{2.19}$$

where the velocity $\hat{u}_i$ was rendered dimensionless with ΩR, the Cartesian coordinates $\hat{x}_i$ with R, the pressure $\hat{p}$ with $\Omega\mu$ and the time $\hat{t}$ with ν/R^2. Along the surface of the cylinder, the dimensionless velocity components are set equal to unity and zero along respectively, the tangential and radial directions, while, at the free surface, the stress balance conditions are given by,

$$pn_i - \left(\frac{\partial u_i}{\partial x_j} + \frac{\partial u_j}{\partial x_i}\right) n_j - \frac{n_i}{Ca} \nabla_s . \mathbf{n} = 0, \tag{2.20}$$

where ∇_s is the surface gradient and $\mathbf{n}(n_i)$ is the unit normal from the liquid to the air. A coupled velocity pressure solution method utilising a direct banded solver was

used to solve the momentum and continuity equation simultaneously and at the end of each time step, the resulting velocities on the free surface were used to update the mesh coordinates. This process was continued until steady state was reached.

While solving these equations we found that the aforementioned algorithm diverged for the case of $Ca = \infty$ due to the extreme deformation of the mesh in a small region of high film thickness gradient. We therefore performed our computations using the values of Ca encountered in the experiments to be described shortly.

We also conducted mesh refinement studies to ensure that an accurate solution had been reached. For example, for the case of $\beta = 4.76$, F=0.1625 ($\alpha = 0.0341$) and Ca=1.08, two meshes containing 1890 and 3360 nodes yielded essentially identical film thickness profiles. Also in some cases, local mesh refinement was performed in order to capture the high gradients in the film thickness. One of the checks for ensuring a steady state solution is that the free surface form a closed streamline and this was confirmed in all our computations.

2.4 Experimental measurements

Using the technique described by Melo([30]), the film thickness was measured along the circumference of the cylinder as a function of α and F in order to ascertain whether the 2-D film profiles determined theoretically could also be reproduced experimentally in the central portion of a cylinder of finite length inspite of the fact that, strictly speaking, the overall flow is three dimensional.

Our experiments were performed in a 27.0 *cm* long circular Plexiglas cylinder, of radius 5 *cm* and fitted with end plates. The cylinder was supported horizontally by axial shafts, one coupled directly to a variable speed motor (0 to 120 rpm), the other hollow, allowing the filling and emptying of the vessel. The liquid used in our experiments was prepared from the same combination of TritonX-100, $ZnCl_2$ and water used earlier([38]) and had a viscosity of 4000 cP (at 23°C), a density of 1.172

gm/cm^3 and a surface tension of 31 dynes/cm (at 24°C). Since the viscosity of the Triton mixture was found to be sensitive to temperature fluctuations, we maintained a constant temperature(with a deviation of ± 0.5°C) throughout the experiments. The Reynolds number $Re \equiv (\Omega h_o^2)/\nu$, with h_o being the mean thickness of the film, was always less than 10^{-2} in all the experiments, hence inertial effects were undoubtedly negligible.

The film thickness was measured ([30]) by a needle attached to the end of a rod that was introduced into the cylinder through the hollow shaft. The rod, in turn, was attached to a series of radial and angular traverses which allowed us to move the needle with a precision of 10^{-2} mm in the radial direction and 2^o in the angular direction. In addition, the measuring system was mounted on an axial traverse such that the film thickness could also be measured at different axial positions along the length of the cylinder. However, all film thickness measurements presented here were made at distances of 7 *cm* to 13 *cm* from the end wall. It should be noted that the local fill fraction at a given axial position was obtained by integrating the experimentally measured film thickness over the circumference of the cylinder. In general, the value of F thereby obtained was found to differ slightly(by less than 5%) from the nominal fill fraction equal to the volume of fluid added divided by $\pi R^2 L$, where L is the length of the cylinder. This small difference could be attributed to the presence of small amounts of liquid which were sticking to the two end walls and also to small misalignments of the cylinder axis from the horizontal. In comparing our theoretical predictions for the film thickness profiles, as obtained via the solutions to the Stokes equations as well as those of eqs.(2.8) and (2.10), with those measured experimentally, we used the value of F as determined from the film thickness measurements rather than its nominal value.

2.5 Results and Discussion

A comparison of the dimensionless film thickness, as obtained from the experimental measurements and from the solution to the Stokes equations as well as from eqs.(2.8) and (2.10) is plotted in figure 2.3 for $\beta = 4.76, F = 0.1625(\alpha = 0.0341), Ca = 1.08$ and in figure 2.4 for $\beta = 3.19, F = 0.1198(\alpha = 0.0376), Ca = 1.31$. Clearly, the agreement is excellent among the three sets. Recall that eq.(2.8) which does not take into account the effects of surface tension, requires that $Ca \gg \alpha^3$, a condition which is here clearly satisfied for Ca as low as 10^{-2}. We also compared the streamline patterns as obtained from the solution of eqs. (2.8) and (2.10) with those computed numerically from the Stokes equations and again found excellent agreement between the two.

A similar comparison of the dimensionless film thickness, is plotted in figure 2.5 for $\beta = 1.98, F = 0.1126(\alpha = 0.0568), Ca = 2.99$. Again, the agreement between the experimental and theoretical results is very good although, due to the increase in the value of α, the solution of eq.(2.8) has deviated somewhat from that of the Stokes equations, at least in comparison to the two cases shown in figures (2.3) and (2.4).

We also compared the experimentally measured non-dimensional film thicknesses (rendered dimensionless with the film thickness at $\theta = \pi/2$) presented by Melo([30]) with the corresponding solution of the Stokes equations and that of the extended lubrication approximation (eqs.(2.8) & (2.10)). Melo([30]) performed experiments for $F = 0.0796$ at $\beta = 1.77$ and $\beta = 1.82$ and for $F = 0.1299$ at four values of β ranging from 1.60 to 1.84. Figure 2.6 shows the profile for $\beta = 1.84(F = 0.1299)$ and $\alpha = 0.0707$ which corresponds to the case of $\omega = 4.9$ in Figure 9(b) in Melo's([30]) paper. Here, $Re = 0.103$ (which is 2 orders of magnitude higher than that in our experiments) and $Ca = 5.66$. Again there is good agreement overall among

all the three sets. On the other hand the experimental points and the theoretical prediction are in slight disagreement in the region of the bump. It appears that this discrepancy could well be due to the local fill fraction being lower (by about 4%) in Melo's([30]) experiment as compared to the stated nominal value of 0.1299. We could not confirm this, however, since Melo([30]) did not report the dimensional film thickness at $\theta = \pi/2$.

In conclusion, we have shown that, by merely adding the hydrostatic pressure gradient term to the standard lubrication approximation we have been able to capture, over the range of parameters considered in this study, the essential features of the film profile, e.g. the maximum thickness of the film and the region of its sharp variation, observed both experimentally and from the numerical solution of the two dimensional Stokes equations, for fill fractions even as high as 0.16.

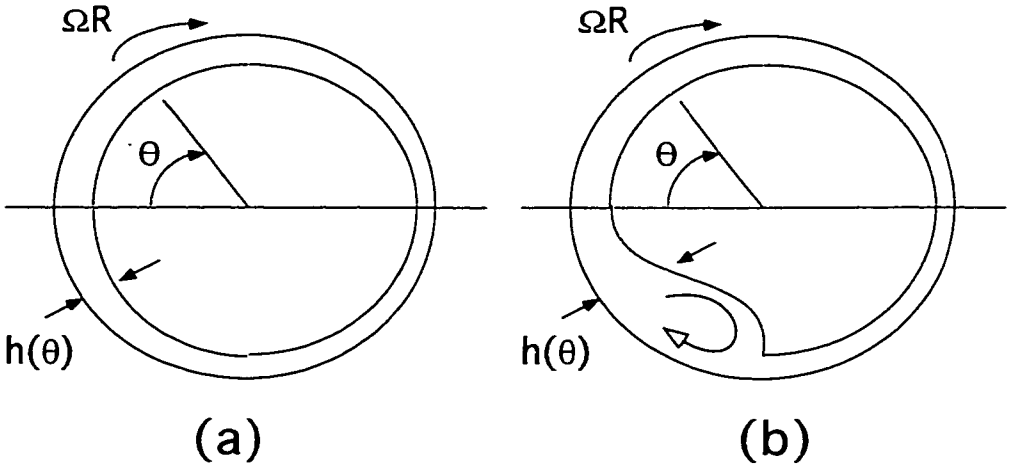

Figure 2.1: A sketch of the film profile for (a) a homogeneous film, $\beta < 1.4142$ (b) a film with with rapid variation in thickness ($\beta > 1.4142$).

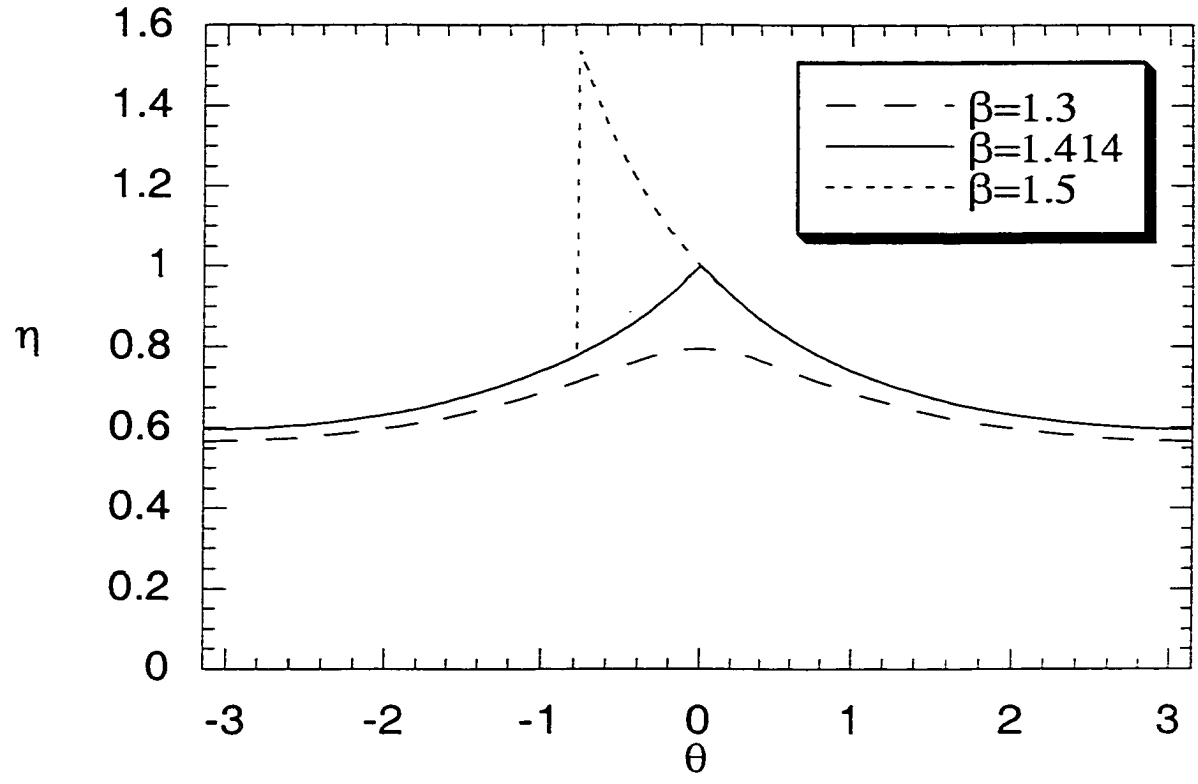

Figure 2.2: The film thickness $\eta(\theta)$ as obtained from solving eq.(2.4) for β=1.3. 1.414(critical) and 1.5.

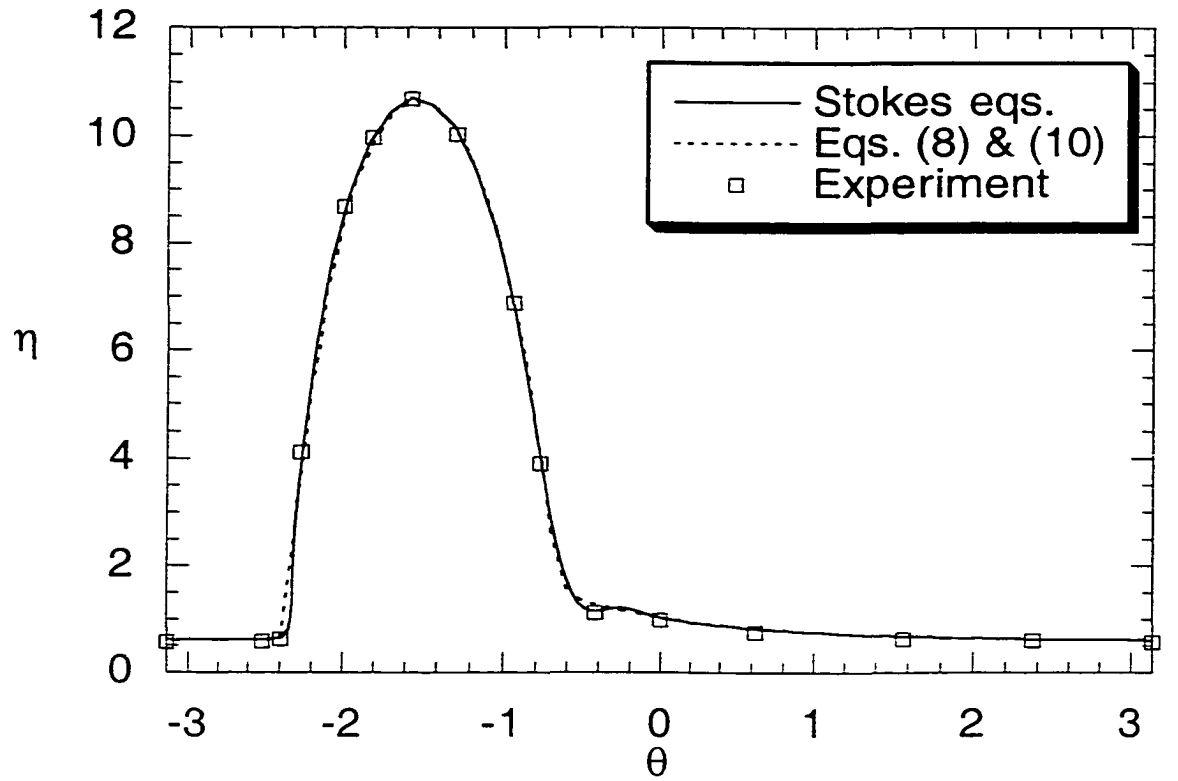

Figure 2.3: The film thickness $\eta(\theta)$ for $\beta = 4.76$, $\alpha = 0.0341 (F = 0.1625)$ as obtained from the experiments and from the solution to the Stokes equations as well as that of eqs.(2.8) & (2.10).

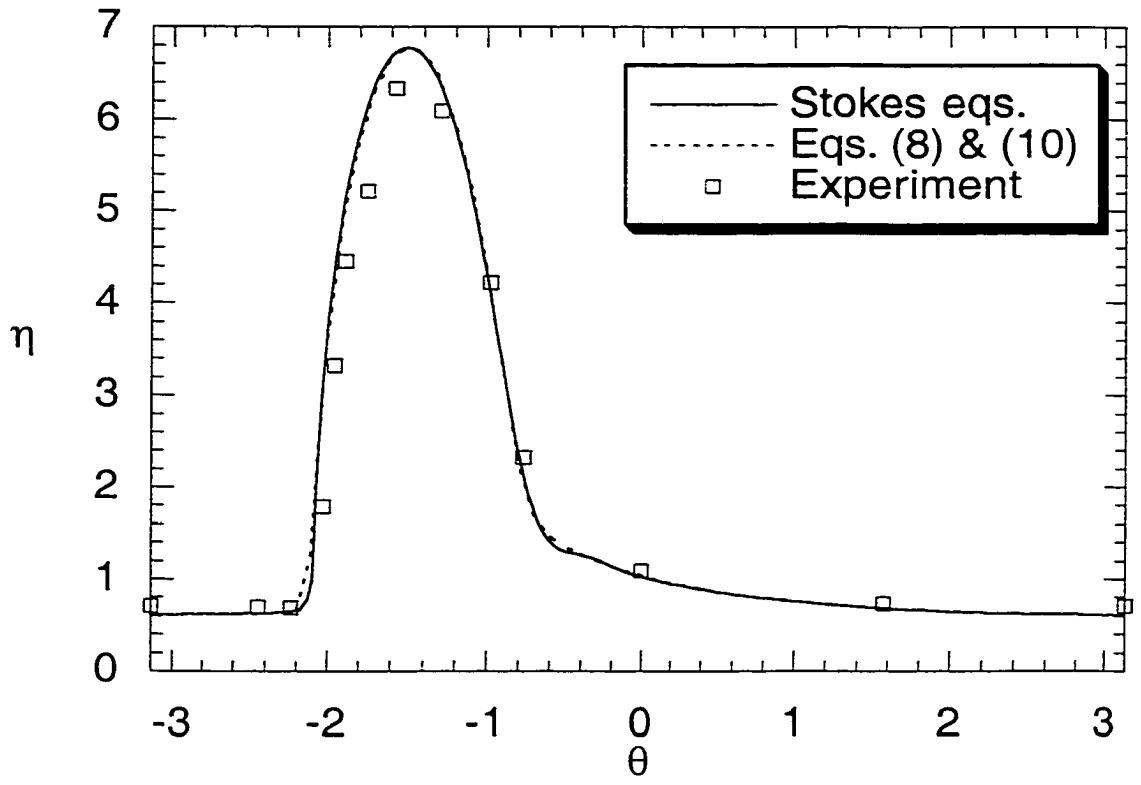

Figure 2.4: The film thickness $\eta(\theta)$ for $\beta = 3.19$, $\alpha = 0.0376(F = 0.1198)$ as obtained from the experiments and from the solution to the Stokes equations as well as that of eqs.(2.8) & (2.10).

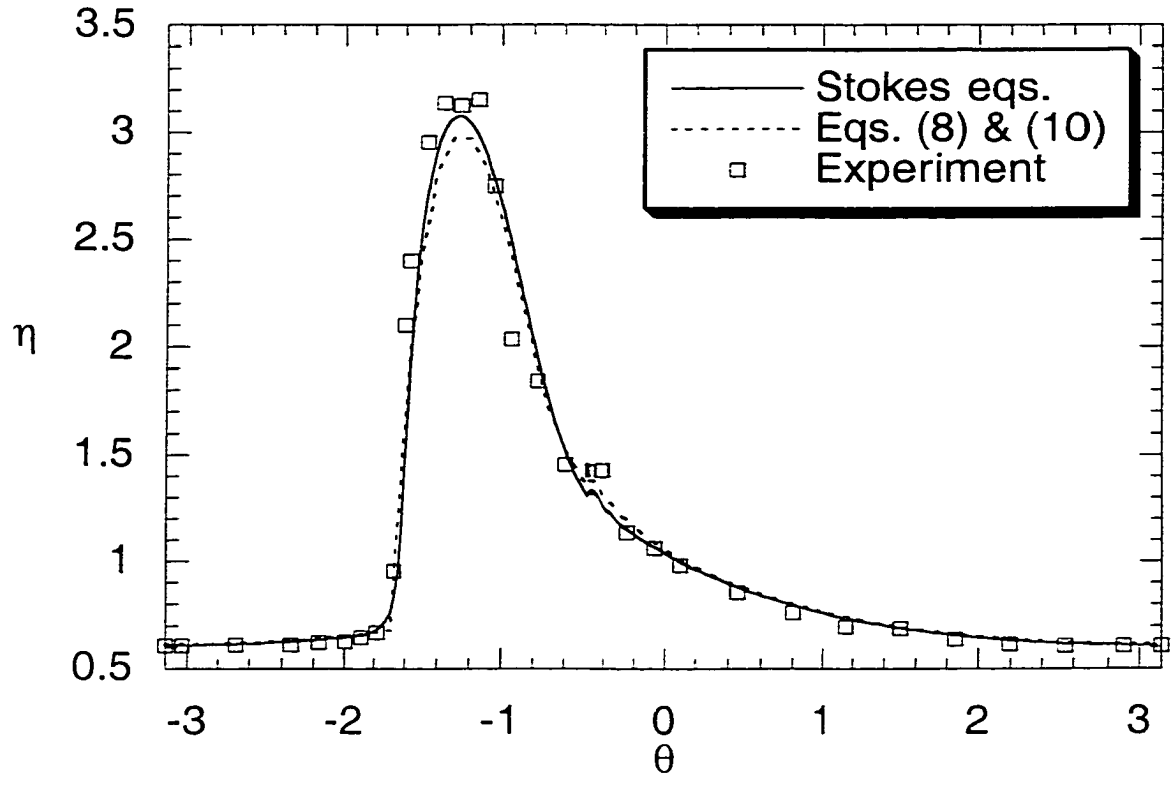

Figure 2.5: The film thickness $\eta(\theta)$ for $\beta = 1.98$, $\alpha = 0.0568(F = 0.1126)$ as obtained from the experiments and from the solution to the Stokes equations as well as that of eqs.(2.8) & (2.10).

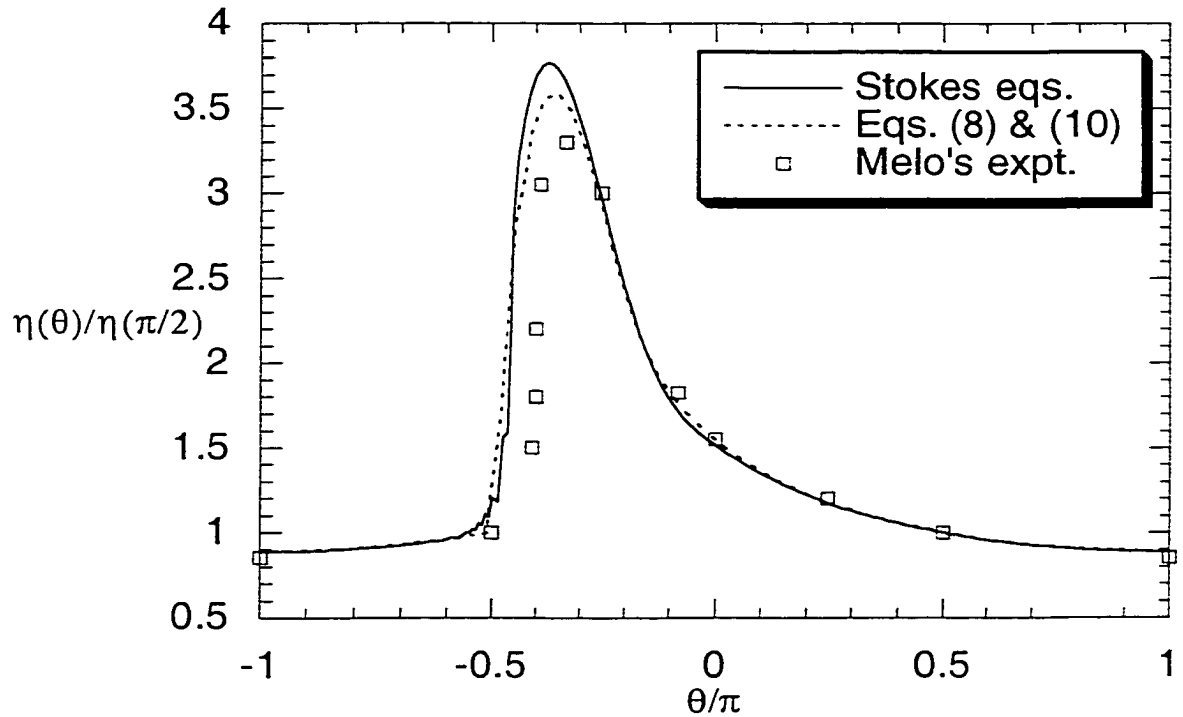

Figure 2.6: The normalized dimensionless film thickness $\eta(\theta)/\eta(\pi/2)$ for $\beta = 1.84$. $\alpha = 0.0707(F = 0.1299)$ as obtained from Melo's ([30]) experiment and from the solution to the Stokes equations as well as that of eqs. (2.8) & (2.10).

Chapter 3

Particle segregation in sheared suspensions: Partially filled rotating horizontal cylinder

Abstract

Experiments in a partially filled horizontal Couette device (Tirumkudulu et al., *Phys. Fluids* **11**, 507 (1999) and also described later in Chapter 4) have revealed a new instability in the flow of suspensions containing narrow-sized neutrally buoyant particles in a very viscous Newtonian liquid where the suspension under shear segregates into regions of high and low particle concentration along the length of the cylinder. We conducted similar experiments but in a different geometry, viz. a horizontal cylinder, in which the cylinder was partially filled with that same suspension and rotated about its horizontal axis. We found that, within a certain range of parameter space, the initially uniform suspension divided into cylindrical bands of high particle concentration separated by regions of essentially particle-free liquid. Although it seems likely that this instability is initiated by particle concentration fluctuations which, in turn, lead to fluctuations in the effective viscosity of the suspension, we have been unable to provide a quantitative explanation for this phenomenon.

3.1 Introduction

Over the years, a rich variety of flow patterns have been observed within a rotating horizontal cylinder partially filled with a particle-free liquid which completely coats the cylinder surface([25]-[32]). These experiments show that, at sufficiently low angular velocities, most of the liquid recirculates at the bottom of the rotating cylinder and that a small amount travels around with, and wets, the inner wall. In addition, the flow is essentially two-dimensional everywhere. However, as the rotation rate is increased, the flow becomes unstable and gives rise to a variety of flow instabilities. Thoroddsen and Mahadevan([31]) have recently performed an extensive study of the various flow states encountered in this flow regime. Though there have been recent attempts([37]) to explain some of the instabilities, a general understanding remains elusive.

Here, we describe yet another curious phenomenon, similar to that reported earlier([38] and described further in chapter 4), but with viscous suspensions containing narrow-sized neutrally buoyant non-colloidal rigid spheres rotated in a partially filled horizontal cylinder. It is observed that when such a suspension, which is initially homogeneous, is rotated in a horizontal cylinder at fractional filling levels varying from 0.15 to 0.75 such that a region of recirculating flow is present at the bottom, the particles also segregated into regions of high and low concentration. In fact, in some cases, the segregation was found to be complete in that the low concentration regions contained a few or even no particles.

The preliminary results of the cylinder experiments, which forms a part of this chapter, have also appeared in a recent publication([39]).

3.2 Experiments with particle-free liquid

We begin by briefly dicussing our experiments with a particle-free viscous liquid. These were performed using two 30 *cm* long circular Plexiglas cylinders, having radii 5 *cm* and 1.27 *cm*, respectively, each of which was fitted with end plates. Each cylinder was supported horizontally by axial shafts, one coupled directly to a variable speed motor (0 to 120 rpm), the other hollow, allowing the filling and emptying of the vessel(fig 3.1(a)). The particle-free fluid was prepared from the same combination of TritonX-100, $ZnCl_2$ and water used earlier([38], c.f chapter 4) and had a viscosity of 4000 cP (at 23°C) and a density of 1.172 gm/cm^3. Since the viscosity of the Triton mixture was found to be sensitive to temperature fluctuations, we maintained a constant temperature(with a deviation of $\pm 0.5^o$C) throughout the experiments. The Reynolds number $Re \equiv (\Omega h_o^2)/\nu$, with Ω being the angular velocity of the cylinder(in radians/sec), h_o the mean thickness of the film and ν the kinematic viscosity of the fluid, was always less than 0.1 in all the experiments, hence inertial effects were undoubtedly negligible.

When the film is thin relative to the cylinder's inner radius, R, and in the absence of inertia and surface tension effects, the dimensionless film thickness profile, $\eta(\theta)$ $(\equiv h(\theta)/(\Omega R\nu/g)^{\frac{1}{2}})$ for a particle-free liquid depends, according to a standard lubrication analysis (chapter 2,[32],[33]-[34]), on the value of a single dimensionless group $\beta = F(gR/\Omega\nu)^{\frac{1}{2}}$ where h is the film thickness, θ is the angular coordinate, F is the filling fraction of the fluid and g is the gravitational acceleration. Furthermore, according to the lubrication analysis referred to above, a continuous film without any sharp variations in its thickness, i.e. a homogeneous film, can exist at steady-state only if $\beta \leq 1.414$. For $\beta > 1.414$, a first order correction to the lubrication analysis is needed([32]) with the result that $\eta(\theta)$ now depends on two dimensionless parameters, β and F, rather than on β alone. On solving the appropriate equation

for $\eta(\theta)$ numerically for $F \leq 0.15$ and $\beta > 1.4$, we obtained a family of profiles([24], chapter 2) which, although continuous, varied sharply over a restricted range of the angle θ (fig 3.1(b)). Such profiles will henceforth be referred to as having a "bump".

In our experiments with the particle-free Triton mixture, and for $\beta > 1.6$ and $0.10 \leq F \leq 0.15$, a bump always formed having a well-defined and perfectly straight front parallel to the axis of the cylinder(fig 3.1(b)). However, for lower values of β, a multiplicity of steady and time dependent flows were encountered which depended on extremely small deviations of the cylinder's axis ($\leq 0.1°$) from the horizontal. In most cases, a straight front was observed but only along a portion of the cylinder while the rest was coated with a homogeneous film. These experimental results were in good agreement with those observed earlier for another very viscous liquid(10,000 cP)([32]) where the transition to these states was observed at $\beta = 1.52$. It should be noted, however, that in none of the states referred to above did the front become wavy. This is contrary to the flows observed for fluids of lower viscosity (of the order of 100 cP) where, for certain values of β (e.g. for the case of a 500 cP liquid ([30]) at $F = 0.136$, $\Omega = 7.3$ rad/s, $\beta = 1.58$, $Re = 0.17$) the bump was found to develop a wavy front along the length of the cylinder([30],[31]). Finally at $\beta \approx 0.7$ and below, a homogeneous film coated the entire cylinder. In what follows we shall restrict our attention to the case $\beta > 1.6$, since, in this regime, the flow of the particle-free liquid was essentially two dimensional except close to the two end walls.

3.3 Experiments with suspensions

Next we performed experiments using an uniformly mixed monodisperse suspension of neutrally buoyant spherical acrylic particles in the same mixture of Triton X-100, $ZnCl_2$ and water as referred to above. Particles of two different sizes viz. 463 ± 37.5 μm and $60+15-35\mu m$ were used and the density and refractive index(1.49) of the suspending liquid was matched with those of the particles. In all the experiments,

5% to 15% of the particles were colored red for visibility.

We found that, when a uniform suspension containing monodisperse spheres was rotated in a partially filled rotating horizontal cylinder such that a distinct bump was present at the bottom of the cylinder, the particles collected in bands separated by regions containing few and in many cases, no particles. Also, the front which was initially straight, developed a regular wavy profile along the length of the cylinder (fig. 3.2). In addition to the axial segregation, however, we found that the particles also segregated radially in the high concentration region (fig. 3.3), in that, for fill fractions below 0.52 and within a certain range of β ($1.6 \leq \beta \lesssim 2.3$), the particles collected in the outer thin film region which travelled around with the moving wall whereas the bottom recirculating region contained very few particles.

Before going into the details of the experiments, it is important to identify the physical parameters relevant to the observed dynamics. The parameters associated with the present flow are :

1. The length, L, and the inner radius, R, of the cylinder.

2. The fractional filling level, F, the angular speed of the cylinder, Ω and the gravity constant, g.

3. The properties of the suspension, namely, the density, ρ, the effective viscosity of the homogeneous suspension, μ, which was computed on the basis of a standard correlation ([1]), the suspending liquid surface tension, σ, the initial average particle concentration, ϕ, and the average particle diameter, $2a$.

These physical quantities can be arranged in the following seven dimensionless groups : $Re \equiv \Omega\rho h_o^2/\mu$, $\alpha \equiv \sqrt{\Omega\mu/\rho g R}$, F, $Ca \equiv \Omega R\mu/\sigma$, L/R, $h_m/2a$ and ϕ. Here, α measures the ratio of the viscous to the gravitational forces while the capillary number (Ca) refers to the relative importance of the viscous to the surface

tension forces. The minimum film thickness ($h_m \sim 0.6\alpha R$) was calculated on the basis of the standard lubrication approximation (chapter 2, [32], [33]-[34]).

In our experiments, Re was always less than 10^{-2} (except in two cases, #20 and #21 in table 3.1) and hence it appears safe to assume that the inertial effects were negligible. The capillary number ranged from 0.05 to 7.3 and α from 0.03 to 0.26. The suspension concentration was varied from 1% to 15% and the fill fraction from 0.15 to 0.75. The experiments were performed in cylinders with the following inner radii and aspect ratios (L/R): 5 cm (6.0), 1.27 cm (6.0, 22.4) and 0.635 cm (6.0, 45.6).

3.3.1 Influence of the various dimensionless numbers on the particle segregation

Experiments were conducted over a broad range of parameters to study their affect on the particle segregation phenomenon. Here, for each experiment, we recorded the time (t) required to achieve particle segregation, the average center to center distance (Z) between the neighboring high concentration bands (henceforth referred to as the wavelength), the average width (W) of the high concentration bands (henceforth referred to as the bandwidth) and the total number of high concentration bands (N). The time required for achieving complete segregation was rendered dimentionless with Ω ($\tau \equiv \Omega t$) and the wavelength and the bandwidth were non-dimensionalized with the radius of the cylinder. The parameter values and the corresponding results for all the experiments have been listed in table 3.1.

In the following subsections, we report the results of experiments where we systematically varied one of the dimensionless parameters while keeping the rest constant. The goal of these experiments was to identify the important variables that affect the process of particle segregation.

It should be noted that, in many experiments, the high concentration bands

moved along the axis of the cylinder due to small misalignments of the cylinder about its horizontal. As a result, even though we report the values of the wavelengths in tables 3.1-3.4, it is difficult in some cases to make a rigorous quantitative comparison between experiments.

Effect of varying α and F

When α was increased while keeping all the other dimensionless variables, except for Ca, constant, it was observed that on an average, the dimenionless time(τ) required for the particles to segregate decreased (Table 3.1). For example, when a 5% suspension was sheared at $\alpha = 0.12$ (#34), the suspension remained homogeneous for a long time ($\tau > 100$) whereas at $\alpha = 0.22$ (#33), the suspension had completely segregated by $\tau = 15$. But, when the fill fraction was increased for a given α, it was found that the value of τ also increased. For example, for $F = 0.16$ and $\alpha = 0.09$ (case #75), complete segregation was achieved by $\tau = 54$, whereas for $F = 0.40$ and at a higher value of α (α=0.12, #78), segregation was achieved at $\tau = 98$. In fact in most cases, whereas a clear segregation (very few particles in the low concentration region) was observed at low fill fractions, a significant number of particles were present in the low concentration region when the suspension was sheared at the same value of α but at higher fill fractions.

The effect of varying both α and F on the degree of segregation can be captured on a single plot which is shown in figure 3.4. Here, the closed circles represent cases of complete segregation in which the bands were separated by regions of particle-free liquid (or regions containing few particles), whereas the open circles represent flow states where a considerable number of particles were present in the low concentration region. The plot seems to indicate that there is a critical value of $\beta(\equiv F/\alpha)$ above which the particles do not segregate completely. For experiments with fill fractions lying between 0.10 and 0.40, the slope of the line demarcating the two regimes has

a value of 0.43 which corresponds to a critical β of 2.3. In our discussion concerning the particle-free fluid experiments, it was pointed out that, for $0.7 \lesssim \beta < 1.6$, a number of complicated flow states were observed which depended on extremely small deviations of the cylinder's axis from the horizontal. As a result, in our suspension experiments with $0.7 \lesssim \beta < 1.6$ ($F \sim 0.15$), the initial straight front and the consequent segregation appeared in only a part of the cylinder with the rest of the region containing a homogeneous film of uniform suspension. Although we did not perform experiments for $\beta < 0.7$, we do not expect any particle segregation in this case since the cylinder would then be covered with a homogeneous film (i.e. without a recirculation flow at the bottom).

For F =0.5, the number of experiments were insufficient to allow an accurate determination of the critical value of β.

We also performed a few experiments at fill levels of 0.75. For ϕ =1% and for values of α of 0.15 (#22) and 0.19 (#21), we found that the nature of the particle segregation pattern was quite different from that in all the previous cases in that the high concentration satellite bands appeared on either side of the main high concentration band (fig. 3.5). Interestingly, whereas the particles in the main band were present in the outer thin film region, the particles in the satellite bands were present in the recirculation region at the bottom of the cylinder. The alternating pattern of the main and the satellite bands was extremely stable and persisted till the end of the experiment. At higher values of α or ϕ (cases #20, #42 and #43), we found that the fluid flow itself became unstable in the sense that, upon start-up, when the suspension was still homogeneous, the film at the top of the cylinder thickened at a few equally-spaced locations in the axial direction. Such flow states at similar fill fractions have also been observed for particle-free liquids ([25],[28],[29]). But since our primary interest is in flow regimes where the motion of the particle-free liquid is essentially two-dimensional, particle segregation in the presence of such

complex flows will not be considered here.

Effect of varying ϕ

On increasing the total particle concentration, we found that the suspension took less time to segregate (Table 3.2) and as expected, the average bandwidth increased with increasing particle concentration.

Effect of varying L/R

From our results, it seems that the aspect ratio does not have a significant effect on the time required for complete segregation (table 3.3). However, the experiments do indicate that the secondary flow induced by the end walls could play an important part in inducing particle segregation in that, in almost all experiments with low particle concentrations ($\phi < 0.05$), the first high concentration bands were always formed next to the two end walls.

When an experiment that had been performed in the cylinder of aspect ratio 22.8 (#29) was repeated in another cylinder having identical radius but a smaller aspect ratio, namely 6.0 (#29a), Z/R decreased from 2.6 to 1.7. Similarly, in the case of the cylinder with radius 0.635 *cm*, Z/R was 3.2 for $L/R = 45.6$(#80) but became equal to 2.4 when L/R was reduced to 6.0(#80a). The results show that the aspect ratio affects the wavelength when the secondary flow generated by the end walls extends over a region that is comparable to the length of the cylinder. The extent of the end wall's influence is approximately equal to the distance of the end wall from the closest high concentration band. This distance was usually the same as the distance between subsequent high concentration bands (wavelength). It would appear that the end walls do not affect the wavelength when the cylinder length is more than 5 to 6 wavelengths.

We did not observe any significant variation in the dimensionless bandwidth (W/R) with changes in L/R.

Effect of varying Ca

In experiments #63 and #80, all the dimensionless numbers are the same except for the capillary number and the aspect ratio (table 3.2) but since the secondary flow induced by the end walls was restricted to a small region, the segregation should not have been affected by the changes in L/R. In both cases the dimensionless time required for segregation was approximately the same and so was the dimensionless width of the bands. A similar trend is observed on comparing cases #60 and #75. These results seem to suggest that both W/R and τ are independent of Ca. However, since the value of Z/R is not the same in the two cases, it would appear that the wavelength is influenced by changes in Ca. Both sets of experiments (i.e. #63 & #80 and #60 & #75) show a decrease in the wavelength with an increase in the capillary number.

Effect of varying particle size relative to film thickness

To gain a better understanding of the segregation phenomenon, we performed experiments for $1.6 < \beta < 2.5$ in the 1.27 cm radius cylinder and with a transparent suspension in which all the acrylic particles were refractive index matched with the liquid. Then, as the particles began to segregate (something which could be easily ascertained from the developing waviness of the front), we introduced a few red acrylic particles into the low concentration region and tracked their motion with a video camera. The suspension also contained a few small dust particles of size approximately 50 μm the motion of which revealed the existence of a secondary flow between the low and the neighboring high concentration regions in the sense that these dust particles were convected from the low to the high concentration region at the bottom of the cylinder and back to the low concentration region on the rising side of the rotating cylinder. But, in contrast to the motion of the dust particles, the red tracer particles did not return to the low concentration region after having

entered the high concentration region. It would appear then that, as the particles depleted the low concentration region and moved into the high concentration region, the film thickness of the former along the rising part of the cylinder decreased owing to an increase in the local value of β, and became comparable to the particle size thereby preventing the acrylic particles from re-entering the low concentration region. In contrast, the dust particles being much smaller than the film thickness, did not experience such resistance. At the bottom of the cylinder, however, the film thickness in both regions was significantly larger than the diameter of the acrylic particles, hence the latter could follow the fluid streamlines.

In order to test this hypothesis, we next performed experiments in the same cylinder at a nominal fill fraction $F = 0.40$ and $\beta = 1.9$ (#82, see also table 3.4) with a suspension containing spherical acrylic particles of mean diameter 60 μm. Here the film thickness was everywhere greater than the particle size and the minimum film thickness (h_m) was about 25 particle diameters. Although the particles did segregate into regions of high and low concentration, the particle concentration in the latter was still appreciable even though the cylinder was kept rotating for more than 48 hrs.

These results suggest that the observed particle segregation is initiated by some as yet unknown mechanism, perhaps a fluctuation in the local particle concentration which modifies the local effective viscosity and thereby the local value of β. But, once the particles start collecting in the region of high concentration, the degree of segregation appears to be determined by the ratio of the film thickness to the particle size.

It was observed that, in a few cases, the bandwidth increased on decreasing $h_m/2a$ (table 3.4). This can be seen on comparing experiments #60, #75 and #1. Here, since the secondary flow induced by the end walls was restricted to a small region near the walls, its effects should have been negligible. We find that, in case

#1, the dimensionless bandwidth is much greater than that observed in cases #60 and #75. A similar observation can be made for case #29 when compared with cases #63 and #80. However, contrary results are found in cases #52 and #77 where, no significant variation in the bandwidth could be observed even though the value of $h_m/2a$ was varied over an order of magnitude.

Thus it is not at all clear as to how the bandwidth is affected by changes in particle size for a given film thickness profile.

Comparison with Boote and Thomas ([40])

Before closing this section it would be interesting to compare our results with those of Boote and Thomas([40]) who conducted similar experiments in a cylinder of radius 5 cm but with heavy particles ranging in size from 250μm to 425μm in a comparatively low viscosity liquid(500 cP). These authors first repeated the particle-free liquid experiments conducted by Melo([30]) and showed that, over a narrow range of β between 1.54 and 1.60 (for 0.135< F <0.145 and $Re \approx 0.18$), the initial straight front developed into a wavy pattern along the length of the cylinder. This, as mentioned before, is in direct contrast to the observations made for higher viscosity liquids (as in our case) where, irrespective of the value of β, the front always remained straight. They then added heavy particles to the particle-free fluid and found that, for particle concentrations above 5% and for high fill levels(F >0.15), the particles collected in bands separated by regions containing only pure liquid. Also the front had a wavy pattern very similar in appearance to that observed for the particle-free fluid. As a result, Boote & Thomas([40]) were unable to conclude definitively whether, in their case, the particle segregation was due to the pre-existing wavy front in the particle-free fluid or whether it was a consequence of a mechanism initiated by the particles. In the light of our experimental results with the particle-free fluids where the front always remained straight and became wavy only in the presence of particle

segregation within the suspension, it is clear that, for the viscous fluids studied here, the formation of the wavy front when bands are present is the result of an instability initiated by the presence of the particles.

3.4 Importance of the secondary flow

As was mentioned already, in the case of the low concentration suspension, the bands formed first close to the end walls due to the secondary flow induced by these walls. We therefore performed a few experiments where we artificially induced a secondary flow in the central portion of the cylinder.

One way of achieving this was to induce an axial variation in the viscosity of the suspension by initially cooling a small region (of width 2 cm) at the center of the cylinder by placing a piece of ice on the outer wall. Here the experiment was performed in the cylinder of radius 1.27 cm and aspect ratio 22.8 containing a 5% suspension of particle size 463 μm. The values of α and F were respectively, 0.17 and 0.30. On rotating the cylinder, we found that, in the initial stages, the particles remained uniformly distributed throughout the cylinder (fig. 3.6(a)). But, within 8 min, the particles started to accumulate within the cooled region where they created a suspension having a concentration distinctly higher than that within the rest of the cylinder where the particles remained uniformly distributed (fig. 3.6(b)). Thus, by locally modifying the system properties (viscosity in this case), we were able to induce segregation in that region. After 20 min, bands started to appear at other locations along the cylinder (fig. 3.6(c)). The ice was then removed and the cylinder was left to rotate for over 15 h. Several bands eventually formed along the cylinder but, interestingly enough, one of them spanned the region that had been cooled initally for the first 20 min of the experiment (fig. 3.6(d)).

We performed similar experiments but with a particle free liquid containing only about 10 to 15 red particles of size 463 μm, in the 1.27 cm radius cylinder at $F \sim 0.25$

and $\alpha \sim 0.1$. Again, the cylinder was cooled in a small region at the center of the cylinder. The motion of the red particles revealed a secondary flow induced by the axial variation of viscosity that convected the particles from the neighboring regions to the cooled region. Surprisingly, after entering the cooled region, the particles became trapped and did not return to their original axial positions. Although it appears that by cooling a section of the cylinder, we were able to simulate flow conditions that were similar to those present in a segregrating suspension, the particles returned to their original axial positions when the piece of ice was removed and the liquid warmed up to the room temperature.

We were also able to induce a secondary flow in the central section of the 1.27 *cm* radius cylinder by tightly fitting within the cylinder a circular ring of aluminium whose outer radius was slightly less than the inner radius of the cylinder(fig. 3.7(a)). The cross section of the ring was an equilateral triangle of length 5 *mm*. In this experiment, the particle concentration, the fill fraction and the value of α were respectively, 5%, 0.35 and 0.18. On rotating the cylinder we found that within 10 minutes low concentration regions developed close to and on either side of the ring(fig. 3.7(b)). After 40 min, high concentration bands had formed on both the sides (fig. 3.7(c)) and at the end of 70 minutes high concentration bands had appeared at other locations along the cylinder (fig. 3.7(d)).

All the above experiments clearly demonstrate the fact that a secondary flow along the axial direction is required for initiating the particle segregation. This could be induced either by particle concentration fluctuations leading in turn to viscosity fluctuations in the suspension or by a disturbance such as that induced by the end-wall or the aluminium ring. However, what is not clear is the mechanism that traps the particles in the high concentration band once they are carried into this region by the secondary flow.

3.5 Measurement of film thickness

In addition to the experiments described above, we also measured the film thickness in the high and the low concentration regions. Here, the experiments were performed in the 5 cm radius cylinder with an aspect ratio of 6.0. The cylinder containing 10% concentration suspension of 463 μm size particles at a fill fraction of 0.12 was sheared such that the value of α calculated using the effective viscosity of the initial homogeneous suspension was 0.055. After segregation had been established, the film thickness in both the high and low concentration regions in the central portion of the cylinder were measured using the experimental setup similar to that described in Chapter 2.

The dimensional film thickness, h, in the center of the high and the low concentration regions is plotted as a function of the angular coordinate θ in fig. 3.8. It is seen that surprisingly, the film in the high concentration region is thicker than that in the low concentration region everywhere except for a small region at the edge of the bump. Even more intriguing is the fact that the local fill fraction in the region of the high concentration band ($F = 0.14$) is much higher than that in the low concentration region ($F = 0.10$).

In light of our tracer (dust particles) experiments, it is important to note the difference in the film profiles for $-\pi/2 < \theta < 0$ (fig. 3.8). At the bottom of the cylinder ($-\pi/2 < \theta < -1.1$), due to a relatively thicker film in the low concentration region as compared to the high concentration region, the hydrostatic pressure gradient drives the flow from the low to the high concentration region whereas on the rising side of the rotating cylinder ($-1.1 < \theta < 0$), due to a relatively thicker film in the high concentration region, the suspension flows in the reverse direction. This is consistent with the secondary flow observations made in the tracer experiment.

Also, the film thickness on the rising side of the low concentration region varied

from about 4 to 16 particle diameters which seems to be sufficiently large for the particles to move freely from the high to the low concentration region. This confirms our earlier finding that the relative size of the particles and the film is not the primary cause for particle segregation.

3.6 Conclusions

The main conclusions of this study are the following :

- It appears that the particle segregation occurs only when a region of recirculating flow is present at the bottom of the cylinder.
- The degree of particle segregation depends primarily on α, F and $h_m/2a$.
  - For $F < 0.40$, clear segregation was achieved for $1.6 < \beta < 2.3$ and $h_m/2a < 15$.
  - For $F \sim 0.15$ and $0.7 < \beta < 1.6$, particles segregated in only a part of the cylinder while the rest of the cylinder was coated with a homogeneous suspension.
  - For large values of $h_m/2a$ (~ 25), a significant number of particles remained in the low concentration region even for $\beta < 2.0$(#82).
- Increasing the total particle concentration (ϕ) led to shorter segregation times.
- The wavelength (Z/R) seems to decrease with an increase in the capillary number (Ca).
- The aspect ratio (L/R) was found to have a significant affect on the wavelength for cylinders of small aspect ratio (relative to the dimensionless wavelengths).
- The bandwidth seems to scale with the radius of the cylinder.

  - The dimensionless bandwidth (W/R) was independent of the capillary number and increased with increasing particle concentration.
  - Experiments conducted on cylinders of different radii but having identical dimensionless parameters (except for Ca) yielded similar values of W/R.
  - No correlation appeared to exist between W/R and $h_m/2a$.

- A secondary flow exists between the high and the low concentration regions.
- Film thickness measurements showed that the local fill fraction in the high concentration region was considerably higher than that in the low concentration region.

The most curious aspect of this phenomenon is the fact that, for $1.6 < \beta \lesssim 2.3$ and $h_m/2a \lesssim 15$, the low concentration region became completely devoid of particles. Shear-induced particle migration theory([1]), which deals with the migration of particles in a concentrated suspension under shear, cannot describe this phenomenon for essentially the following three reasons. First, particle segregation occurs for suspension concentrations as low as 1% when the interparticle interactions are negligible. Secondly, such a theory seems incapable of explaining the presence of regions that are completely devoid of particles because their existence would lead to infinitely high concentration gradients at the boundaries of the bands which cannot be sustained owing to the presence of a diffusive mechanism, such as shear induced particle migration from regions of high concentration to low. Finally, if the segregation was indeed caused by shear induced particle migration, then the time required for the particles to segregate completely from the initial homogeneous state (or for the system to reach steady state) should be proportional to the square of the particle size given that the diffusion coefficient is proportional to the square of the particle size and the local shear rate. From table 3.4 we can see that even when the particle

size was increased by an order of magnitude (e.g. #52 & #77), the time required to achieve completely segregation did not change significantly.

Clearly, this phenomenon requires further study.

#	R	2a	ϕ	Ω	α	F	β	L/R	2a/R	Ca	hm/2a	Re	τ	Z/R	N	W/R	Comment
	(cm)	(micron)	(%)	(rpm)													
1	1.27	463	1	2.9	0.1	0.16	1.6	22.8	0.036	0.6	1.67	8.30E-05	41	2.5	9	0.4	complete
2	1.27	463	1	2.4	0.09	0.16	1.9	22.8	0.036	0.4	1.42	7.90E-05	58	2.7	10	0.4	complete
3	1.27	463	1	1	0.06	0.16	2.8	22.8	0.036	0.2	1	2.70E-05					incomplete
4	1.27	463	1	7.9	0.16	0.28	1.7	22.8	0.036	1.5	2.67	7.90E-04	25	2.4	6		complete
5	1.27	463	1	5.8	0.14	0.28	2	22.8	0.036	1.1	2.33	5.60E-04	81		4	0.3	complete
8	1.27	463	1	2.5	0.09	0.28	3.3	22.8	0.036	0.4	1.42	2.80E-04		2.1	4	0.4	incomplete
9	1.27	463	1	16.4	0.24	0.4	1.7	22.8	0.036	3.3	4	3.40E-03	36	2.4	7	0.5	complete
11	1.27	463	1	8.5	0.17	0.4	2.4	22.8	0.036	1.7	2.83	1.80E-03	30	2.8	7		complete
13	1.27	463	1	4.1	0.12	0.4	3.4	22.8	0.036	0.8	2	8.40E-04		2.4			incomplete
14	1.27	463	1	19.5	0.26	0.52	2	22.8	0.036	3.9	4.33	7.50E-03	20	2.5	6		complete
16	1.27	463	1	15	0.23	0.52	2.3	22.8	0.036	3.1	3.83	5.70E-03	38	2.4	6	0.3	complete
19	1.27	463	1	6.34	0.15	0.52	3.5	22.8	0.036	1.3	2.5	2.40E-03				0.4	incomplete
20	1.27	463	1	18.6	0.22	0.75	3.2	22.8	0.036	2.8	3.67	2.50E-02					unstable
21	1.27	463	1	11	0.19	0.75	3.9	22.8	0.036	2.1	3.17	1.20E-02	33	2.6	6	0.2	complete
22	1.27	463	1	6.5	0.15	0.75	5	22.8	0.036	1.3	2.5	6.70E-03	52	1.9	8	0.2	complete
23	1.27	463	3	9.1	0.18	0.35	1.9	22.8	0.036	1.9	3	1.40E-03	18		7	0.4	complete
24	1.27	463	3	9.1	0.18	0.4	2.2	22.8	0.036	1.9	3	1.80E-03	23			0.4	complete
25	1.27	463	3	9.1	0.17	0.5	3	22.8	0.036	1.7	2.83	3.50E-03				0.4	incomplete
28	1.27	463	5	1.15	0.06	0.1	1.6	22.8	0.036	0.2	1	1.40E-05	36	2.8		0.6	complete
29	1.27	463	5	2.4	0.09	0.15	1.7	22.8	0.036	0.5	1.5	6.10E-05	11	2.6	8	0.6	complete
29a	1.27	463	5	2.8	0.1	0.16	1.7	6	0.036	0.6	1.67	7.80E-05	<33	2.5	2		complete
30	1.27	463	5	1.54	0.07	0.15	2.1	22.8	0.036	0.3	1.17	4.20E-05	<19	1.9	9	0.5	complete
31	1.27	463	5	0.9	0.06	0.15	2.5	22.8	0.036	0.2	1	1.90E-05					incomplete
33	1.27	463	5	14.6	0.22	0.4	1.8	22.8	0.036	2.8	3.67	3.20E-03	14.6	2.2	8	0.6	complete
33a	1.27	463	5	15.4	0.22	0.4	1.8	6	0.036	2.8	3.67	3.20E-03	15	0	1		complete
34	1.27	463	5	4.3	0.12	0.4	3.3	22.8	0.036	0.8	2	9.30E-04		1.65	10	0.5	incomplete
34a	1.27	463	5	4.3	0.12	0.4	3.3	6	0.036	0.8	2	9.30E-04		2.3	2	0.5	incomplete
35	1.27	463	5	5	0.13	0.75	5.8	22.8	0.036	1	2.17	5.30E-03		2.1	8		incomplete

Table 3.1: This table lists the various dimensional and dimensionless parameters for all the experiments. Here, R is the radius (in cm) of the cylinder, $2a$ is the average particle diameter (in μm), ϕ (in %) is the initial homgeneous suspension concentration, Ω (in rpm) is the rotation rate of the cylinder, $\alpha \equiv \sqrt{\Omega\mu/\rho g R}$, F is the fill fraction, $\beta \equiv F/\alpha$, $Ca \equiv \Omega R\mu/\sigma$ is the capillary number, $Re \equiv \Omega\rho h_o^2/\mu$ is the Reynolds number, $h_m \sim 0.6\alpha R$ is the minimum film thickness calculated by means of the standard lubrication approximation (chapter 2,[32],[33]-[34]), $\tau \equiv t\Omega$ is the dimensionless time required for the particles to segregate completely, Z/R is the dimensionless wavelength, W/R is the dimensionless bandwidth, N is the number of bands and the comments column indicates qualitatively the extent of particle segregation for each experiment.

#	R	2a	ϕ	Ω	α	F	β	L/R	2a/R	Ca	hm/2a	Re	τ	Z/R	N	W/R	Comment
	(cm)	(micron)	(%)	(rpm)													
36	1.27	463	10	8.2	0.18	0.35	1.9	22.8	0.036	2	3.07	1.10E-03	16.4			0.7	complete
38	1.27	463	10	10.1	0.22	0.4	1.8	22.8	0.036	2.8	3.67	1.50E-03	<10.1	2	9	0.6	complete
43	1.27	463	10	5.9	0.17	0.75	4.5	22.8	0.036	1.7	2.83	4.30E-03					unstable
44	1.27	463	10	3	0.12	0.75	6.4	22.8	0.036	2	2	2.20E-03					unstable
45	1.27	463	15	0.73	0.06	0.1	1.7	22.8	0.036	0.2	1	5.50E-06	5	2	9	1	complete
46	1.27	463	15	0.5	0.05	0.1	2	22.8	0.036	0.1	0.83	3.70E-06		2.4			incomplete
47	1.27	463	15	0.25	0.04	0.1	2.9	22.8	0.036	0.1	0.58	1.90E-06					incomplete
49a	1.27	463	15	1.5	0.09	0.15	1.7	6	0.036	0.5	1.5	2.40E-05		1.81	2		complete
49	1.27	463	15	1.45	0.08	0.15	1.8	22.8	0.036	0.4	1.33	2.80E-05	7.2	2	10	1.1	complete
50	1.27	463	15	1.1	0.07	0.15	2.1	22.8	0.036	0.3	1.17	2.10E-05		2.3	10	0.8	incomplete
51	1.27	463	15	0.7	0.06	0.15	2.6	22.8	0.036	0.2	1	1.20E-05					incomplete
52	0.64	463	1	7.4	0.23	0.39	1.7	45.6	0.072	0.8	1.92	3.50E-04	51.8	4.72	7,8	0.4	complete
53	0.64	463	1	2.7	0.12	0.39	3.2	45.6	0.072	0.2	1	1.70E-04		4.4	7	0.7	incomplete
54	0.64	463	1	1.38	0.09	0.39	4.3	45.6	0.072	0.1	0.75	8.00E-05		3.1	11	0.8	incomplete
58	0.64	463	5	7	0.22	0.4	1.8	45.6	0.072	0.7	1.83	3.70E-04	7	3.3	13	0.5	complete
59	0.64	463	5	2.5	0.13	0.4	3.1	45.6	0.072	0.2	1.08	1.30E-04		2.8	15		incomplete
60	5	463	1	10.2	0.09	0.16	1.8	6	0.009	7.3	6	5.00E-03	30	0.72	6	0.2	complete
61	5	463	1	2.8	0.05	0.16	3.5	6	0.009	1.9	3.07	1.40E-03	22	0.54	9	0.2	complete
62	5	463	1	1.2	0.03	0.16	5.3	6	0.009	0.8	2	6.20E-04		0.45	11	0.2	incomplete
63	5	463	5	9.1	0.09	0.16	1.8	6	0.009	7.3	6	4.00E-03	9	0.7	7	0.4	complete
64	5	463	5	1.9	0.04	0.16	4	6	0.009	1.4	2.67	8.80E-04		0.5	10		incomplete
65	5	463	15	2.8	0.06	0.1	1.7	6	0.009	3.2	4	3.20E-04	2.8	1	8		complete
66	5	463	15	2.3	0.05	0.1	1.9	6	0.009	2.2	3.33	3.10E-04	>16	0.7	9	0.5	complete
67	5	463	15	1.16	0.04	0.1	2.6	6	0.009	1.4	2.67	1.20E-04		0.5	14	0.6	incomplete
68	5	463	15	3.1	0.07	0.13	1.8	6	0.009	4.2	4.53	4.80E-04	3	0.76	8	0.5	complete
69	5	463	15	2.8	0.07	0.13	1.9	6	0.009	3.9	4.4	4.20E-04	<5.6	0.76	7,8	0.5	complete
70	5	463	15	1.3	0.05	0.13	2.7	6	0.009	1.9	3.07	1.90E-04		0.65	9,10	0.3	incomplete
72	5	463	15	4.8	0.08	0.15	2	6	0.009	5.1	5	1.40E-03		0.9	7	0.6	complete

Table 3.1 (Contd.)

#	R	2a	ϕ	Ω	α	F	β	L/R	2a/R	Ca	hm/2a	Re	τ	Z/R	N	W/R	Comment
	(cm)	(micron)	(%)	(rpm)													
73	5	463	15	1.2	0.04	0.15	3.9	6	0.009	1.4	2.67	3.10E-04		0.4	13	0.3	incomplete
74	5	463	15	0.58	0.03	0.15	5.6	6	0.009	0.8	2	1.30E-04		0.4	13	0.3	incomplete
75	0.64	60	1	1.5	0.09	0.16	1.7	45.6	0.009	0.1	6	1.40E-05	54	3.6	10	0.2	complete
76	0.64	60	1	0.7	0.06	0.16	2.5	45.6	0.009	0.1	4	6.70E-06					incomplete
77	0.64	60	1	8.2	0.22	0.39	1.8	45.6	0.009	0.7	14.67	4.70E-04	57.4	3.6	11	0.7	complete
78	0.64	60	1	2.7	0.13	0.4	3.2	45.6	0.009	0.2	8.33	1.70E-04		4.7	9	0.8	incomplete
79a	0.64	60	5	7.1	0.22	0.4	1.8	6	0.009	0.7	14.67	3.80E-04					unstable
79	0.64	60	5	7.1	0.22	0.4	1.8	45.6	0.009	0.7	14.67	3.80E-04	14	2.8	14		complete
80	0.64	60	5	1.3	0.09	0.16	1.7	45.6	0.009	0.1	6.27	9.50E-06	<15	3.2	13	0.3	complete
80a	0.64	60	5	1.2	0.1	0.16	1.7	6	0.009	0.1	6.4	7.70E-06	<18	2.4	2	0.4	complete
81	1.27	60	1	2.8	0.11	0.22	1.9	22.8	0.005	0.7	13.56	1.10E-04		2.2	5,7	0.4	complete
82	1.27	60	1	15.2	0.21	0.4	1.9	22.8	0.005	2.6	25.2	3.80E-03		2.4	7	0.5	incomplete
83	1.27	60	1	4.1	0.11	0.4	3.6	22.8	0.005	0.7	13.2	1.00E-03		2	7		incomplete

Table 3.1 (Contd.)

#	R	2a	ϕ	Ω	α	F	β	L/D	2a/R	Ca	hm/2a	τ	Z/R	N	W/R
	(cm)	(micron)	(%)												
29	1.27	463	5	2.4	0.09	0.15	1.7	22.8	0.036	0.47	1.5	11	2.6	8	0.6
49	1.27	463	15	1.45	0.08	0.15	1.8	22.8	0.036	0.37	1.33	7	2	10	1.1
60	5	463	1	10.2	0.09	0.16	1.8	6	0.009	7.27	6	30	0.72	6	0.2
63	5	463	5	9.1	0.09	0.16	1.8	6	0.009	7.27	6	9	0.7	7	0.4
75	0.635	60	1	1.5	0.09	0.16	1.7	45.6	0.009	0.12	6	54	3.6	10	0.2
80	0.635	60	5	1.3	0.09	0.16	1.7	45.6	0.009	0.13	6.27	<15	3.2	13	0.3

Table 3.2: A comparison of experiments where all the dimensionless parameters *except* for the total particle concentration was kept constant.

#	R	2a	ϕ	α	F	β	L/R	2a/R	Ca	hm/2a	τ	Z/R	N	W/R
	(cm)	(micron)	(%)											
29	1.27	463	5	0.09	0.15	1.7	22.8	0.04	0.47	1.5	11	2.6	8	0.6
29a	1.27	463	5	0.1	0.16	1.7	6	0.04	0.58	1.67	6	1.7	3	0.4
33	1.27	463	5	0.22	0.4	1.8	22.8	0.04	2.8	3.67	15	2.2	8	0.6
33a	1.27	463	5	0.22	0.4	1.8	6	0.04	2.8	3.67	15	0	1	0.5
79	0.64	60	5	0.22	0.4	1.8	45.6	0.01	0.7	14.7	14	2.8	14	
79a	0.64	60	5	0.22	0.4	1.8	6	0.01	0.7	14.7				
80	0.64	60	5	0.09	0.16	1.7	45.6	0.01	0.13	6.27	<15	3.2	13	0.3
80a	0.64	60	5	0.1	0.16	1.7	6	0.01	0.13	6.4	<18	2.4	2	0.4

Table 3.3: A comparison of experiments where all the dimensionless parameters *except* for the aspect ratio was kept constant.

#	R	2a	ϕ	α	F	β	L/R	2a/R	Ca	hm/2a	τ	Z/R	N	W/R
	(cm)	(micron)	(%)											
1	1.27	463	1	0.1	0.16	1.6	22.8	0.036	0.58	1.67	41	2.5	9	0.4
60	5	463	1	0.09	0.16	1.8	6	0.009	7.27	6	30	0.7	6	0.2
75	0.635	60	1	0.09	0.16	1.7	45.6	0.009	0.12	6	54	3.6	10	0.2
29	1.27	463	5	0.09	0.15	1.7	22.8	0.036	0.47	1.5	11	2.6	8	0.6
63	5	463	5	0.09	0.16	1.8	6	0.009	7.27	6	9	0.7	7	0.4
80	0.635	60	5	0.094	0.16	1.7	45.6	0.009	0.13	6.27	<15	3.2	13	0.3
52	0.635	463	1	0.23	0.39	1.7	45.6	0.072	0.77	1.92	52	4.7	7,8	0.7
77	0.635	60	1	0.22	0.39	1.8	45.6	0.009	0.7	14.67	57	3.6	11	0.8
9	1.27	463	1	0.24	0.4	1.7	22.8	0.036	3.34	4	36	2.4	7	0.5
82	1.27	60	1	0.21	0.4	1.9	22.8	0.005	2.55	25.2		2.4	7	0.5

Table 3.4: A comparison of experiments where the ratio of the particle size to the cylinder radius was varied.

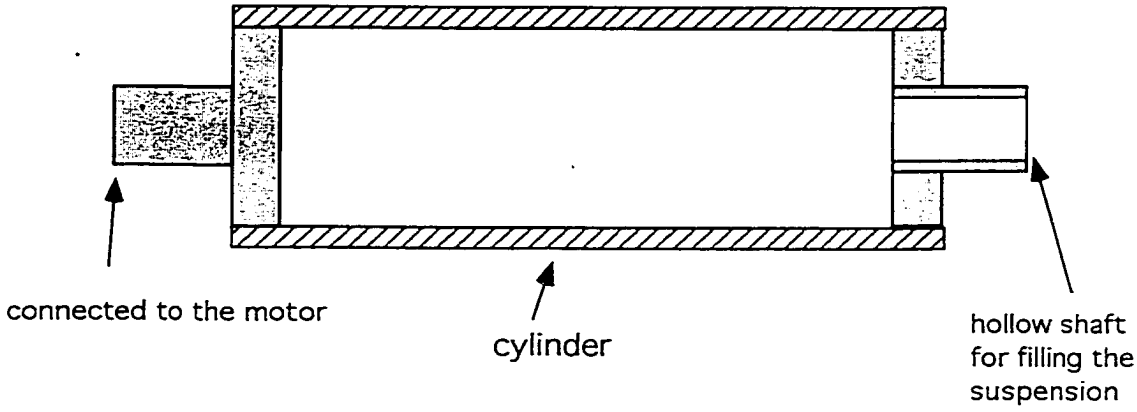

(a)

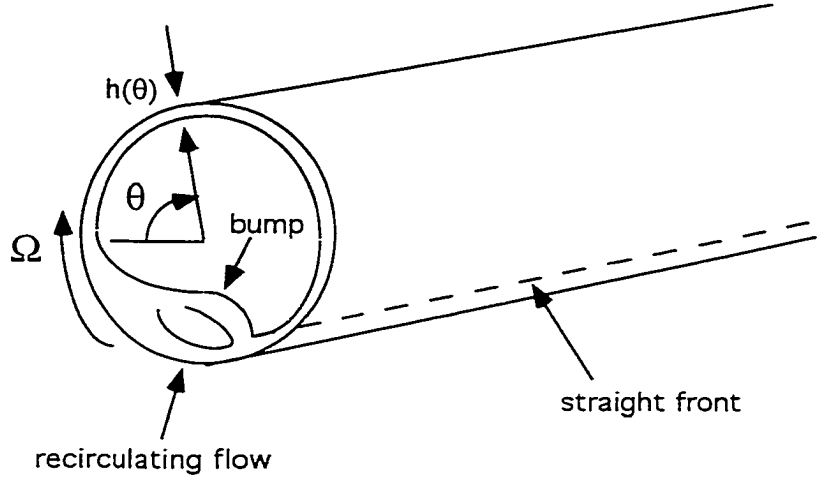

(b)

Figure 3.1: A sketch showing (a) the horizontal cylinder, (b) the free surface shape in the presence of a bump.

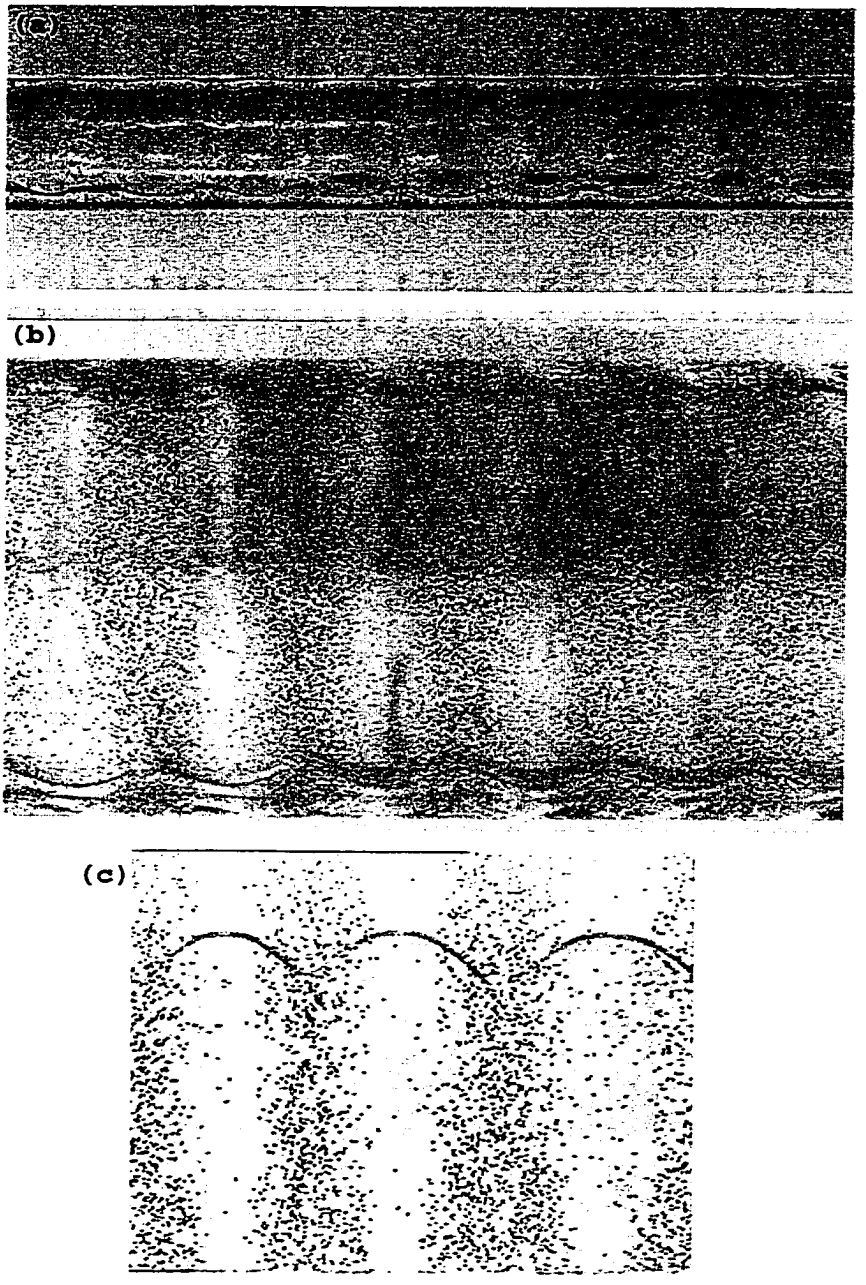

Figure 3.2: Segregation and band formation for a 15% suspension (a) at 1.4 rpm and F=0.15 in a 1.27 cm radius cylinder ($\mu(23^oC)$=4000 cP, β=1.8) and, (b) at 2.8 rpm and F=0.125 in a 5.0 cm radius cylinder ($\mu(21.5^oC)$=4900 cP, β=1.9). (c) A close-up of the wavy front observed in case (b) when viewed from the bottom of the cylinder.

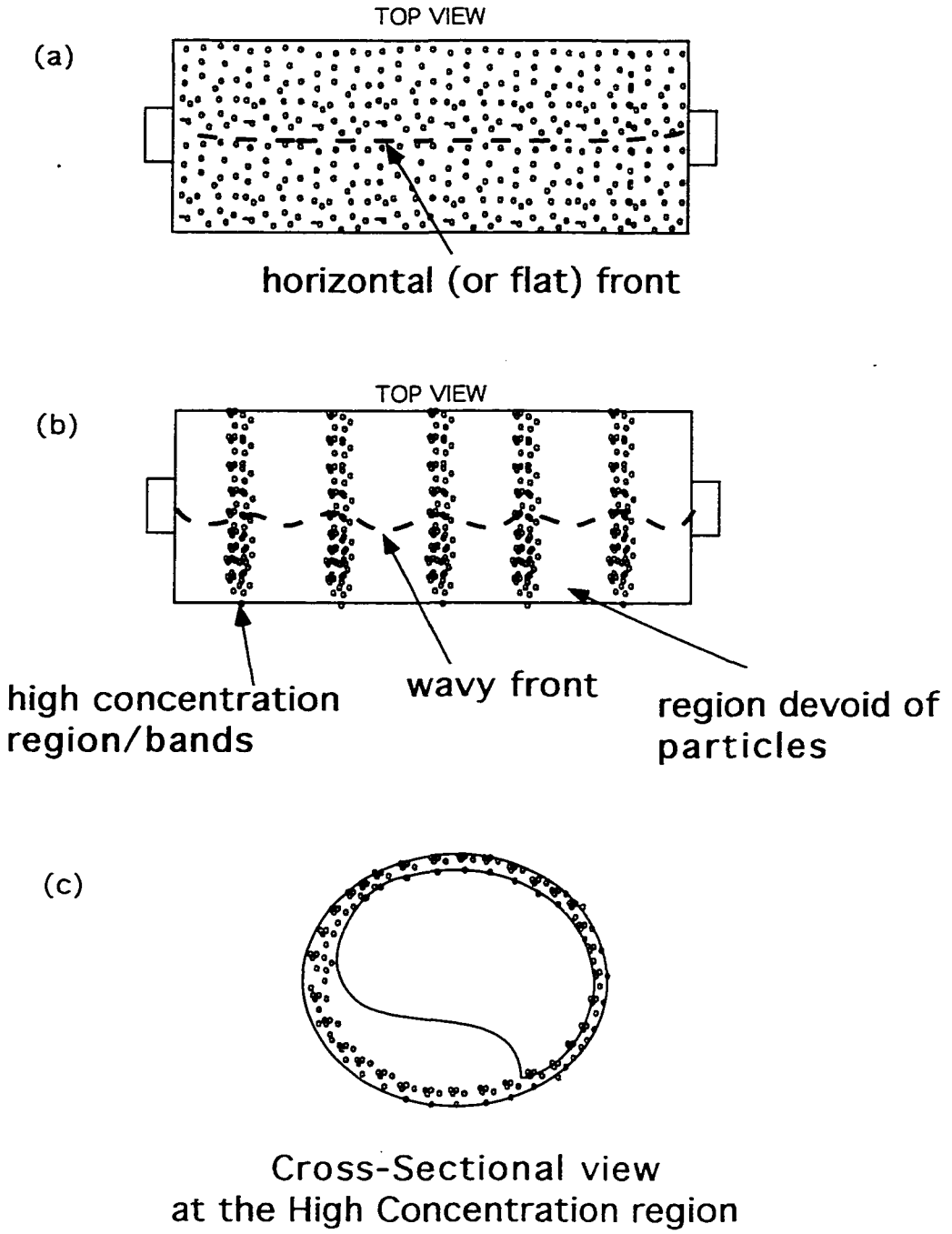

Figure 3.3: A sketch showing (a) the initial horizontal front, (b) the wavy front upon particle segregation and, (c) the radial particle distribution in the high concentration band region.

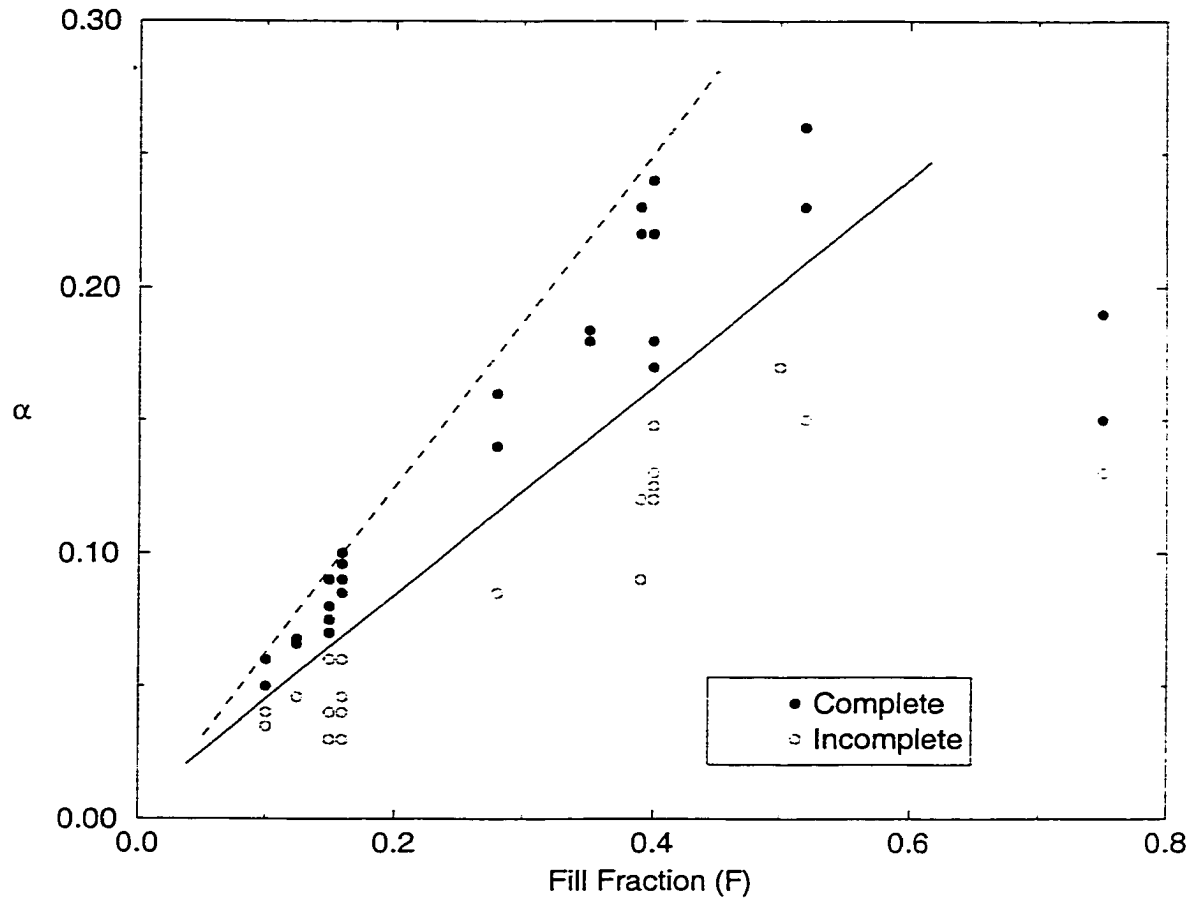

Figure 3.4: The extent of particle segregation achieved for the various experiments is plotted here. The filled circles denote complete segregation in which the bands were separated by regions of essentially particle-free liquid whereas the empty circles represent experiments where a significant number of particles were present in the low concentration region. The slope of the solid line demarcating these two regimes is approximately 0.43 which leads to a value of $\beta \approx 2.3$. The dashed line represents $\beta = 1.6$.

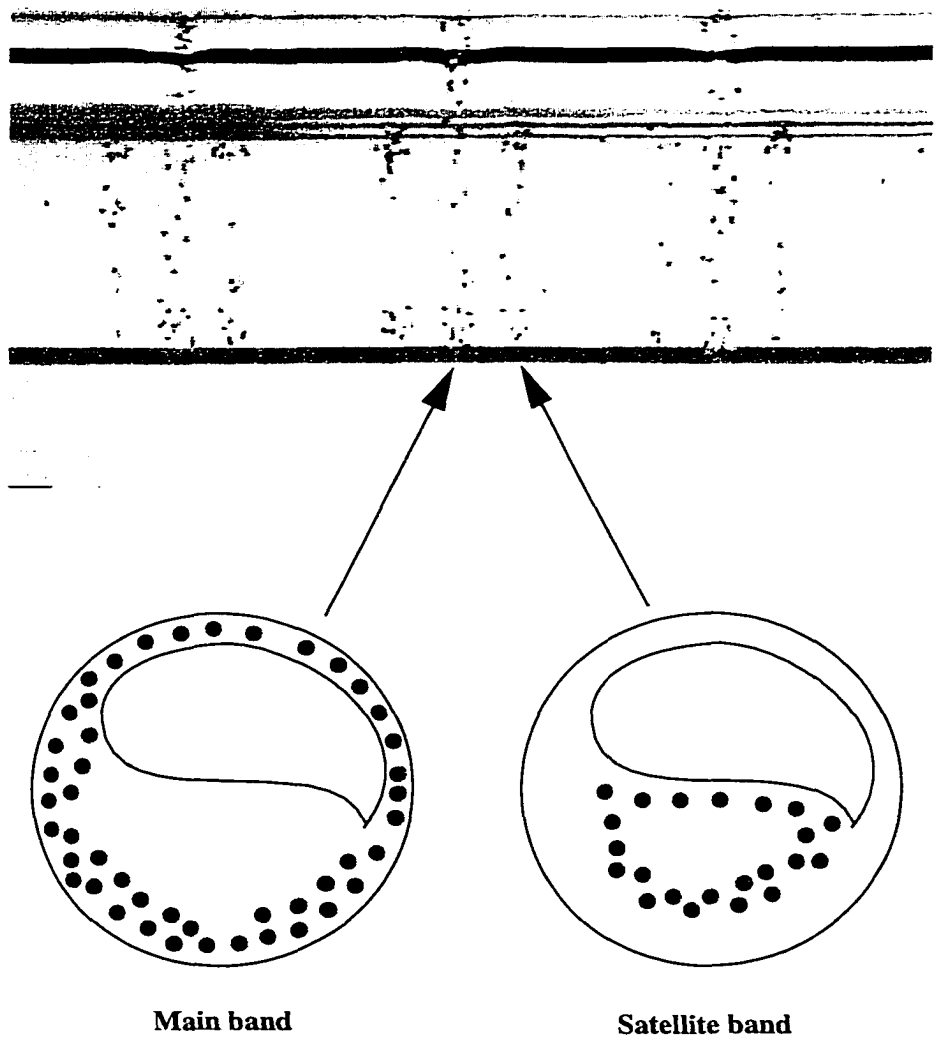

Figure 3.5: Segregation and band formation for 1% suspension at 6.5 rpm and F=0.75 in a 1.27 cm radius cylinder (μ(22°C)=4600 cP, β=5.0). The corresponding sketch shows the radial particle distribution in the main and the satellite bands.

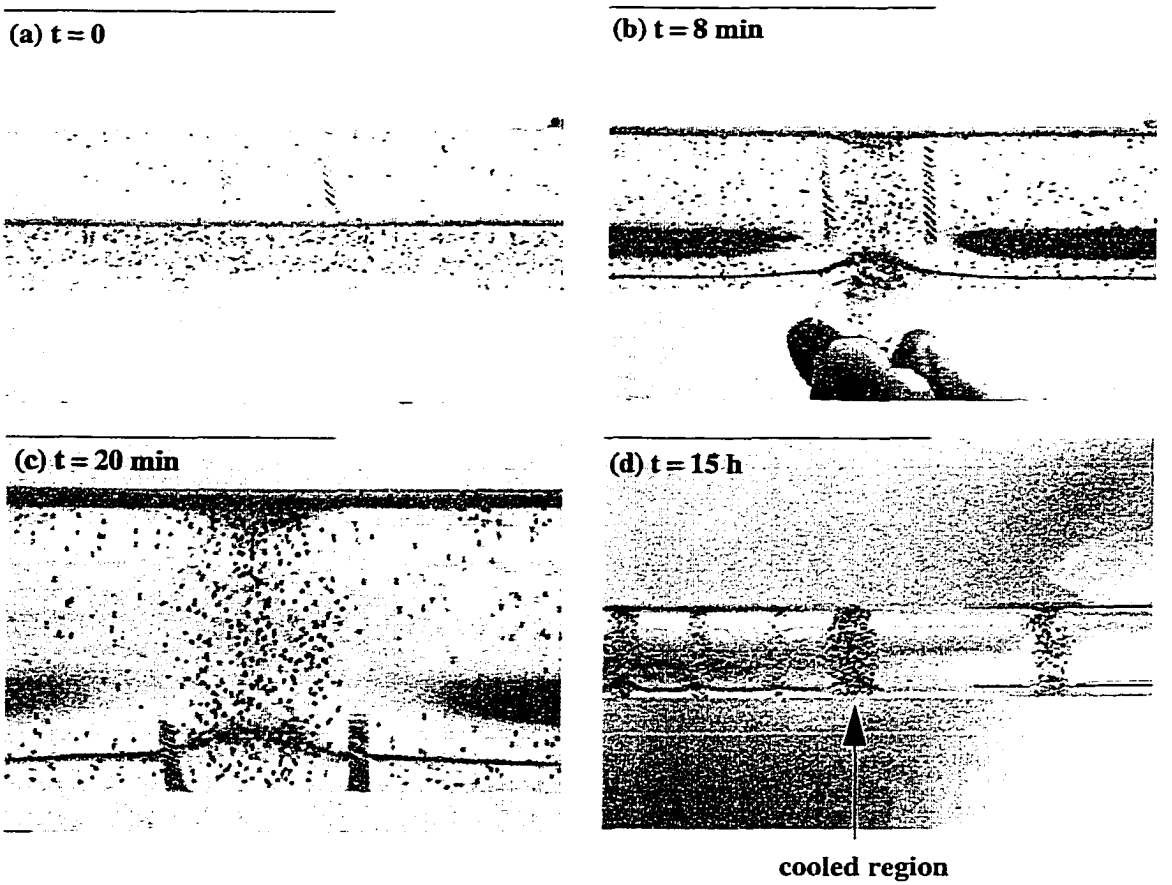

Figure 3.6: The set of photographs show particle segregation being induced artificially by placing a piece of ice on the outer wall. The region being cooled is demarcated by a set of stickers stuck to the outer wall. (a) Homogeneous suspension at the start of the experiment. (b) Particle segregation after 8 min of starting the experiment. The photograph also shows the piece of ice placed on the wall. Segregation (c) after 20 min and , (d) after 15 h.

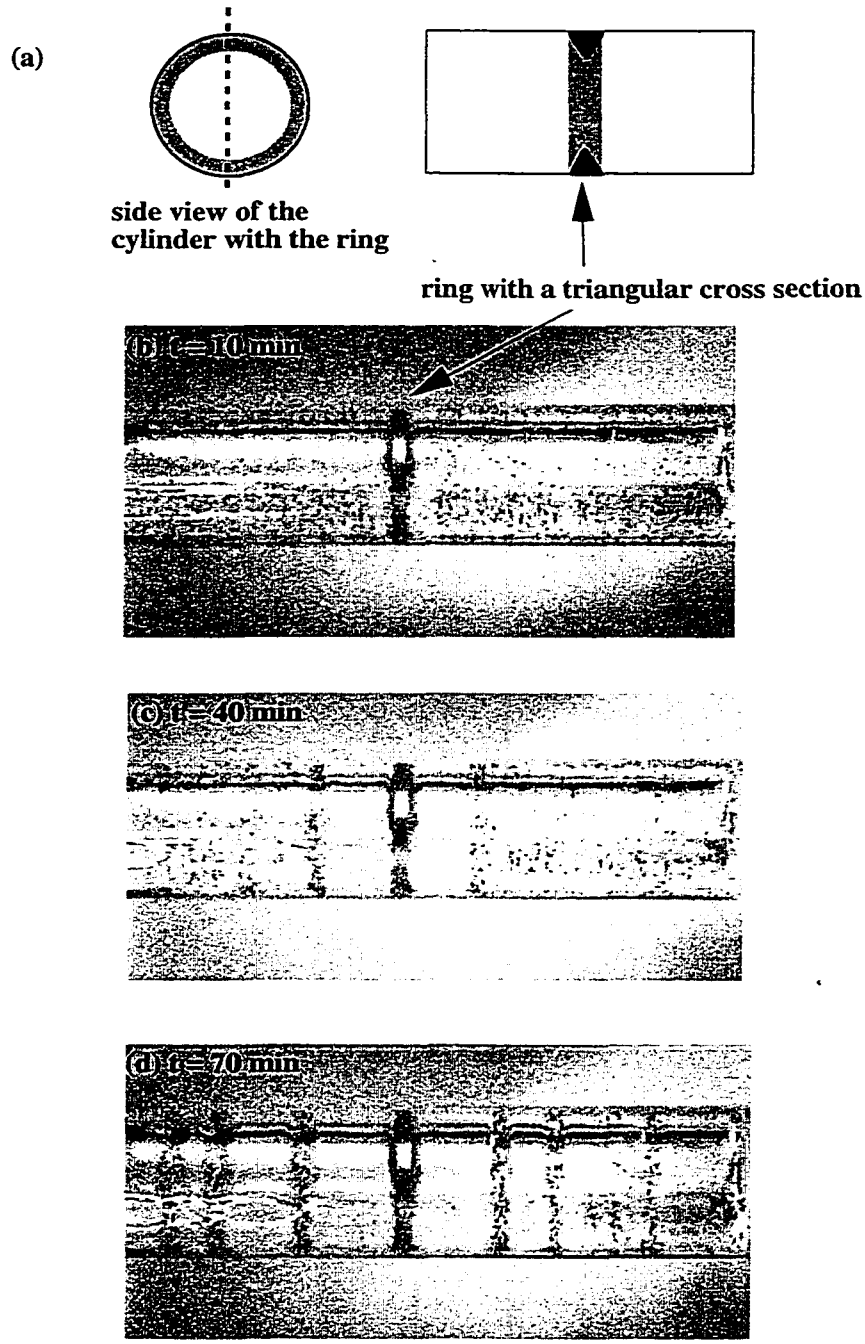

Figure 3.7: The set of photographs show particle segregation being induced artificially by placing an aluminium ring inside the cylinder. (a) A sketch of the ring inserted inside the cylinder. Particle segregation and band formation at the end of (b) 10 min, (c) 40 min, and (d) 70 min

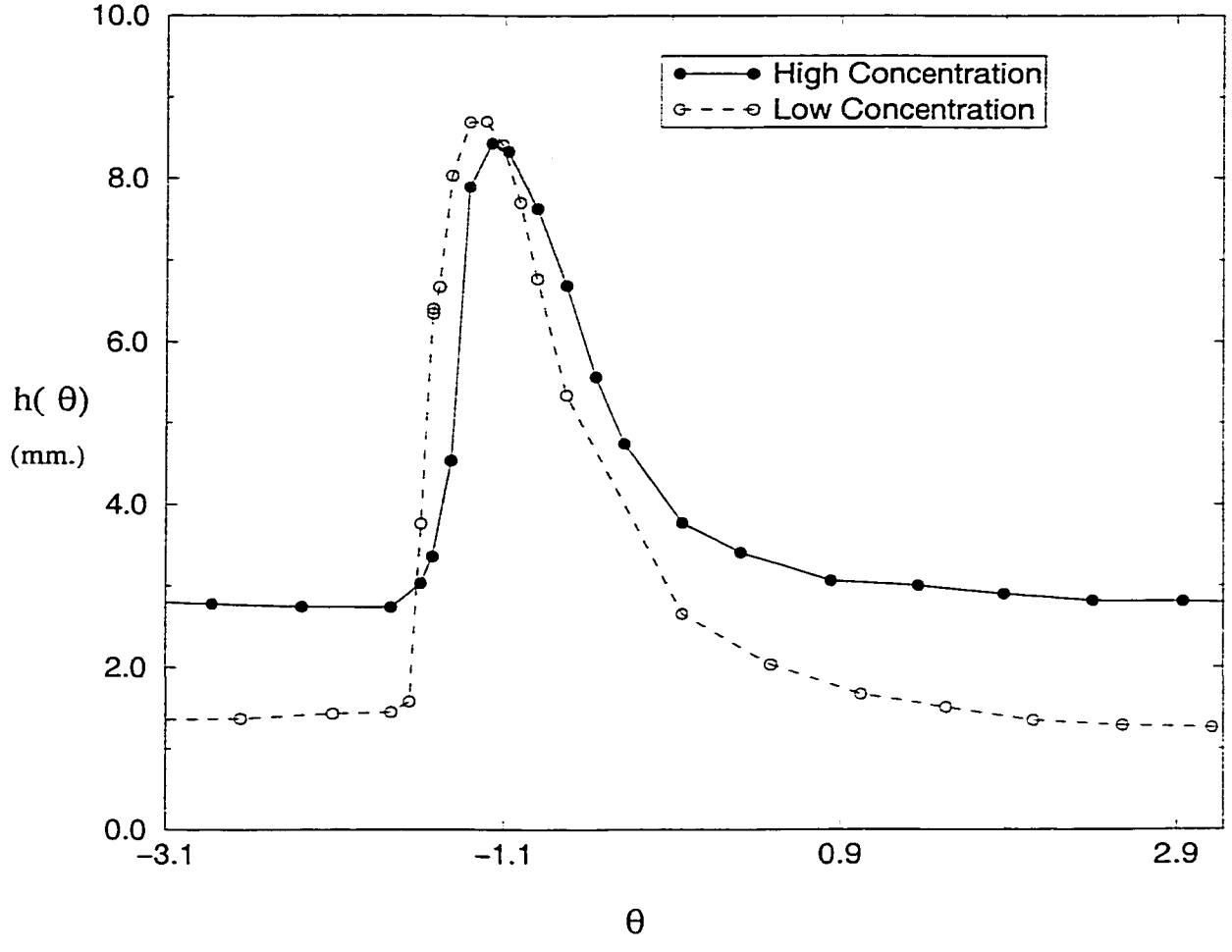

Figure 3.8: The plot shows the film thickness profile measured at the center of the high and low concentration regions in the 5 cm radius cylinder for a 10% suspension containing particles of size 463 μm and sheared at $\alpha = 0.055$ and $F = 0.119$.

Chapter 4

Particle Segregation in Monodisperse Sheared Suspensions: Flow in a Partially Filled Horizontal Couette Device

Abstract

It has been known for a long time that many mixtures of granular materials tend to segregate when tumbled in a rotating horizontal cylinder, with the different components separating into bands of relatively pure single concentration along the rotational axis([41]). Here we report a phenomenon([38]) that seems to be analogous, but in suspensions of monodisperse neutrally buoyant spherical particles in a Newtonian liquid medium being sheared in a partially filled horizontal Couette device in which the suspension separates itself into alternating regions of high and low particle concentration along the length of the tube. The experiment is mostly qualitative, the aim at this stage being primarily to provide photographic evidence of a curious and as yet unexplained phenomenon.

4.1 Experimental setup

Our experiments were performed in a horizontal Couette device, shown in Fig. 4.1, consisting of two concentric cylinders (made of Plexiglas) with the outer cylinder fixed and the inner cylinder free to rotate. The radius of the inner cylinder was 1.21 *cm.* and the inner radius of the outer cylinder was 1.90 *cm.* The length of the cylinders was 26.3 *cm.* The presence of bearings at the two ends sealed the gap between the cylinders. Two holes were drilled on the outer cylinder for filling the gap with suspension.

4.2 Experimental results and discussions

We first performed experiments with pure Newtonian liquids (i.e free of particles) of different viscosities which were placed in partially filled horizontal Couette device and then sheared by rotating the inner cylinder at various rotation rates. In these experiments we examined how the shape of the contact line made by the liquid along the surface of the stationary outer cylinder was influenced by the liquid viscosity, the rotation rate of the inner cylinder and the fill level of the fluid.

When a liquid (prepared from a combination of Triton X-100, $ZnCl_2$ and water) of viscosity 3400 *cP* filled 95% of the available volume in the Couette, the contact line was straight for rotation rates between 1 to 10 *rpm*, but became wavy at higher rotation rates. At lower fill levels, e.g. at a 88% fill level, the contact line was straight from 1 to 20 *rpm*. With a higher viscosity fluid, viz. Dow Corning-510 fluid of viscosity 18,000 *cP*, and at a 90% fill level, the contact line was straight at 4.5 *rpm* but wavy at 16 *rpm*. On decreasing the fill level to 80%, the contact line reverted to being straight at 16 *rpm*. When the viscosity of the Dow Corning-510 fluid was increased to 26,000 *cP*, we found that, although the contact line was wavy at 10 *rpm* and at 95% fill, it became straight at the same rotation rate but at a

lower fill level(90%). These results indicate that, in the case of the pure newtonian fluids, the shape of the contact line depends on the rotation rate, the fill level and the viscosity of the fluid. Also, from these experiments we conclude that for all the fluids having a viscosity below 26,000 cP, the contact line remains straight for fill levels upto 90% and rotation rates between 1 and 10 rpm.

Next we repeated our experiments using a uniformly mixed suspension of spherical acrylic particles of mean diameter 462.5±37.5μm dispersed in the same combination of Triton X-100, $ZnCl_2$ and water referred to above. The density (1.174 gm/cc) and the refractive index (1.491) of the liquid were matched with that of the particles. In all the experiments, 5-15% of the suspended particles were colored red for visibility. We found that, as shown in fig. 4.2, when a uniformly mixed suspension of 10% particle concentration having an effective suspension viscosity of about 4800 cP, as computed using a standard correlation[1], was rotated at 9 rpm under conditions where the fill level was 95%, the contact line developed a regular wavy pattern. But, more importantly, the suspension separated itself into alternating regions of high and low particle concentration along the length of the Couette device with the high concentration regions located underneath the crests and the low concentration regions underneath the troughs of the wavy interface (as sketched in Figure 4.3). No segregation was observed when the Couette was completely filled with the suspension implying that a free surface is required for this to occur.

The experiments were performed with suspensions having particle concentrations 5%, 10%, 15% and 30% and for Reynolds numbers $Re \equiv (U\rho d/\mu) \ll 1$, where ρ and μ are the density and viscosity of the suspension, U is the tangential speed of the inner cylinder and d is the gap width between the inner and outer cylinder. In all cases, the rotation rates were varied from 1-20 rpm for fill levels of 50%, 90% and 95%.

Particle segregation occurred beyond a critical rotation rate whose value de-

pended on the fill ratio and the particle concentration. For example, for the 15% suspension at 50% fill level, segregation was observed at 4.6 *rpm* but not at 3.3 *rpm* even when the suspension was sheared for more than 24 hours. However, when the fill level was increased to 95%, the particles segregated even at 2 *rpm*. For a 10% suspension at 95% fill level, we found segregation at 9 *rpm* but not at 5 *rpm*. Similar observations were made for the 5% and the 30% suspensions (the latter had an effective viscosity of 12800 *cP*). As mentioned before, no segregation was observed when the Couette was completely filled (100% fill level).

For a given rotation rate, the width of the high concentration region/band was found to increase with an increase in the suspension concentration. Figure 4.4 shows the segregation and band formation at 9 *rpm* for the 5% and 15% suspensions and at 90% and 95% fill levels respectively. We also compared the segregation for the 15% suspension at 50%(figure 4.5(b)) and 95% fill levels. In the former case, and at 9 *rpm*, the segregation seems to be less distinct as compared to the 95% fill level at 9 *rpm* (fig. 4.4(b)). It is interesting to note that, at the 50% fill level, the bands are smaller in width and more in number than for the 95% fill level. In all the cases, the suspension was well mixed before being sheared in order to maintain the same initial conditions.

For a given suspension concentration, the segregation was enhanced at higher rotation rates and the demarcation between the high and low concentration regions became more distinct. Figure 4.5(a) shows segregation at rotation rates 2.5 *rpm* for a 15% suspension filling 95% of the available gap volume. On comparing this to the case of 9 *rpm* at a similar concentration and fill level(figure 4.4(b)), it can be seen clearly that at 2.5 *rpm* the bands are much thinner but more in number while, at the higher rotation rate, the number of bands has decreased but the degree of segregation has been enhanced. Here, in contrast to the other cases, the contact line of the suspension is straight without any evidence of waviness.

Next, we performed similar experiments with neutrally buoyant suspensions in fluids of much lower viscosities.The particles were monodisperse polystyrene spheres having a density of 1.045 gm/cc and a mean diameter of 465.5μm, suspended in two Newtonian fluids, viz. UCON 50-HB-660 of viscosity 250 cP(24°C) and Dow Corning 556(40.9% by volume)+Dow Corning 775(59.1% by volume) of viscosity 57.2cP(24°C), both of density 1.045 gm/cc. In both the suspensions, 25% of the particles were colored red for visibility.

In case of the UCON suspension, we performed experiments with a 15% suspension (having an effective viscosity of 680 cP) at two different fill levels, 50% and 95%. At the 95% fill level, the rotation rate was varied from 2 to 13 rpm. Similar to the observations made with the Triton-acrylic suspension, we found a critical rotation rate of 3.5 rpm for the 95% fill level below which there was no segregation. Further, at a given concentration and fill level, we observed that the time required for segregation decreased with an increase in the rotation rate. Figure 4.6(a-c) shows how the bands develop in time in a 15% UCON suspension (95% full gap volume) when the rotation rate is maintained at 9.3 rpm. As can be seen, 5 minutes after the rotation has began (fig. 4.6(a)) the particle concentration within the suspension remained uniform with no sign of segregation. However after 11 minutes(figure 4.6(b)), the particles are seen to have segregated and, after 29 minutes(figure 4.6(c)), the high concentration bands have increased in thickness and are more distinct than before. The suspension had reached steady state at this time. Figure 4.7 shows the contact line viewed from the top of the Couette when a 15% concentrated suspension and 95% fill level is sheared at 13 rpm. From all these experiments with the UCON fluid it can be seen that, unlike in the case of the Triton-acrylic suspension, the contact line was straight without the presence of troughs and crests. These observations seems to indicate that the shape of the free surface is a consequence and not a driving mechanism for the particle segregation. The presence of the wavy contact line

in case of the Triton-acrylic system may be attributed to the large differences in the relative viscosity of the high and the low concentration regions. This difference is much lower for the the UCON suspension since the viscosity of the UCON oil is an order of magnitude lower than that of the Triton suspending fluid. Unlike in the case of the Triton-acrylic suspension, we found that the width of the high and the low concentration regions did not vary with the rotation rate.

When the fill level of the UCON suspension was reduced to 50%, there was no segregation even after the inner cylinder was rotated at rotation rates as high as 18 *rpm*. This is indeed surprising since for the Triton+Acrylic suspension, segregation was achieved at around 6 rpm at similar fill levels.

For the Dow Corning suspension, we performed a single experiment at a 95% fill level and for a 15% concentration at 3.5 *rpm*. After 24 *hrs*, good segregation had been achieved. The contact line in this case was again straight.

4.3 Conclusions

In conclusion, we have identified a new instability when a horizontal Couette device is partially filled with a suspension of monodisperse particles suspended in a viscous liquid for particle concentrations as low as 5% in which the particles within the initially uniform suspension segregate into alternating bands of high and low concentration. Experiments with high viscosity particle free liquids indicate that, although the waviness of the contact line at high fill levels ($\geq$90%) could play a role in initiating the particle segregation for the Triton suspension at similar fill levels, the fact that segregation took place even when the contact line remained straight either in suspensions with liquids of low viscosities(see figures 4.6, 4.7), or, at low fill levels (see fig 4.5(b)), with high viscosity particle free liquids under similar conditions, would seem to provide strong evidence in support of the notion that the particle segregation is a new phenomenon which does not result from the presence

of a waviness in the contact line referred to above.

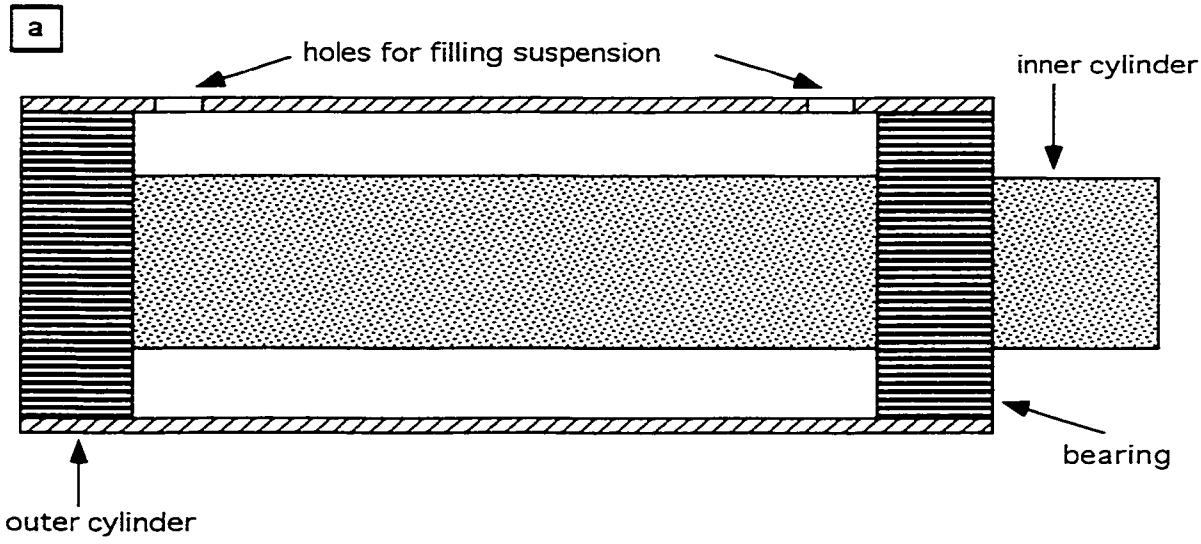

Figure 4.1: A sketch showing the Couette device

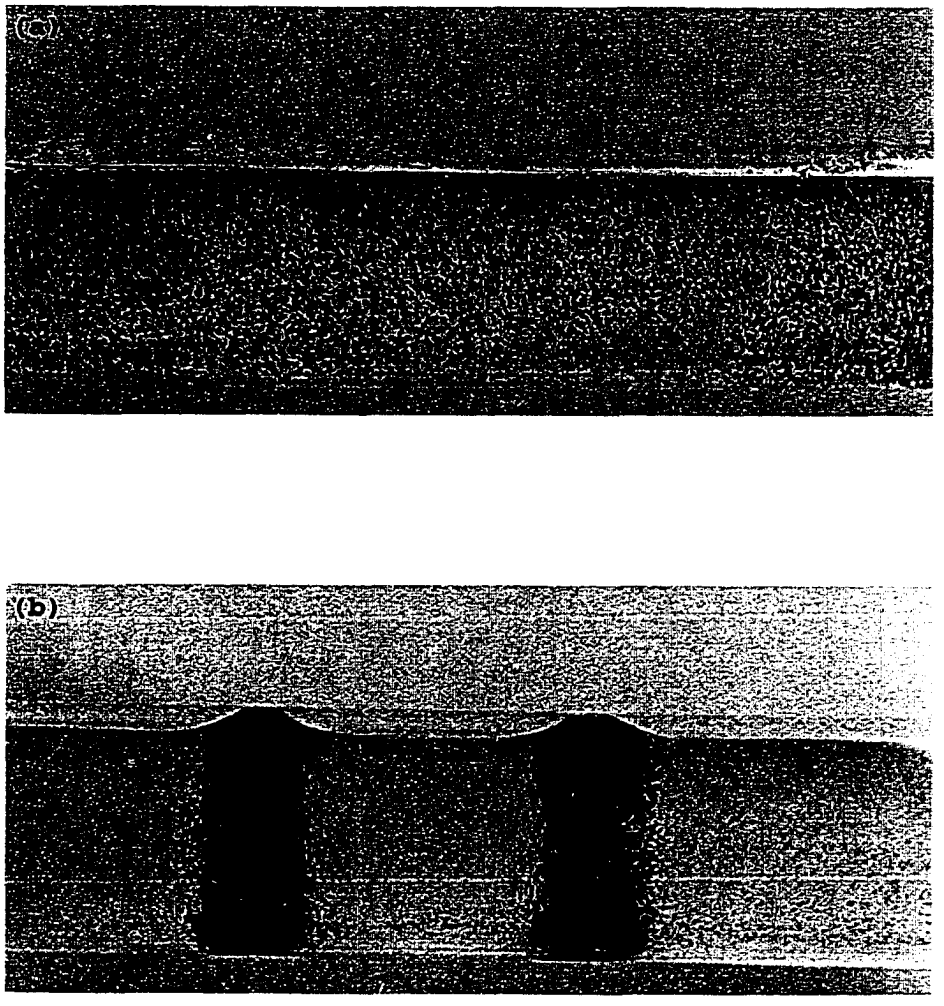

Figure 4.2: A well mixed 10% suspension before and after shearing the inner cylinder at 9.0 rpm when the Couette is filled up to 95% of the available gap volume

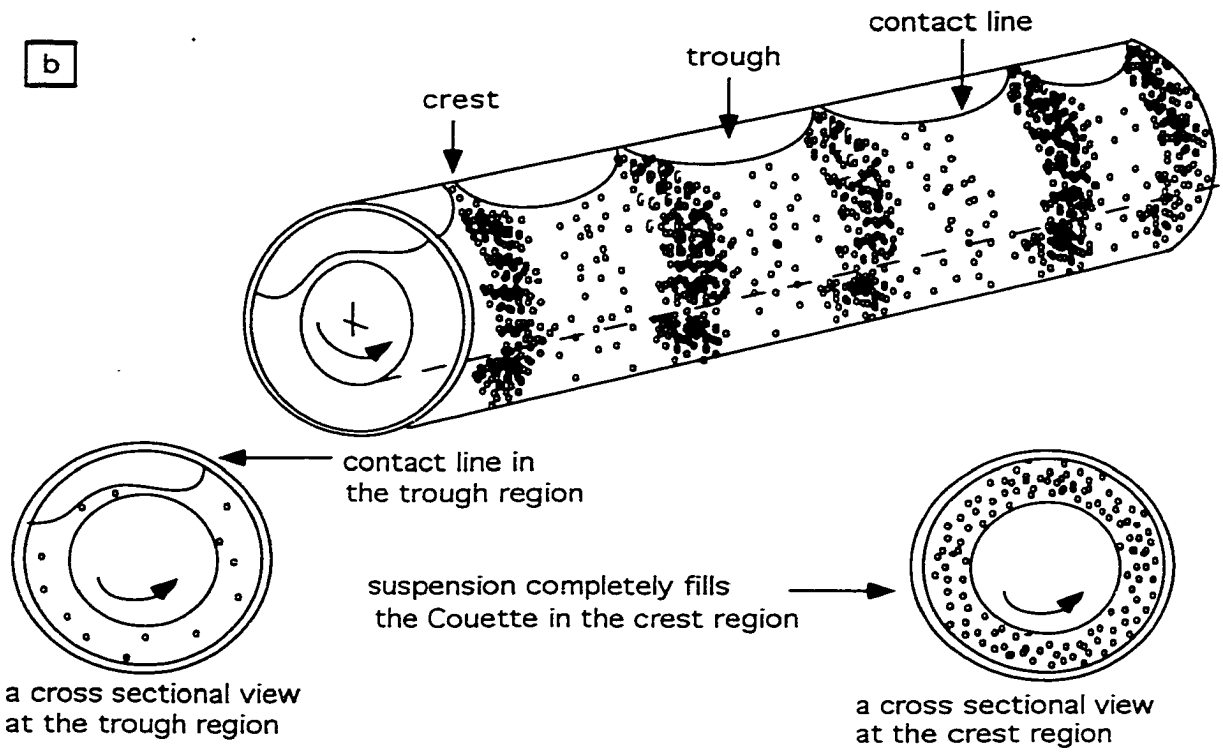

Figure 4.3: A sketch showing a suspension being sheared in the Couette device.

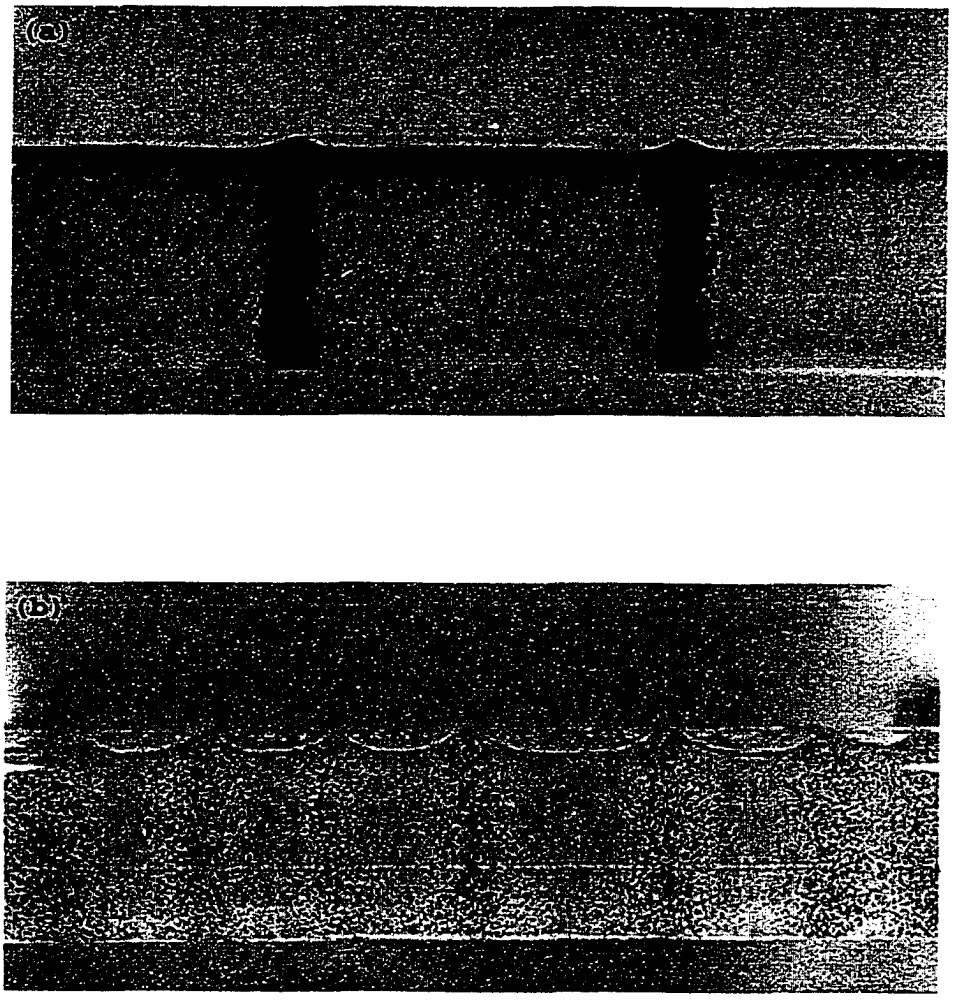

Figure 4.4: Segregation and band formation at 9 *rpm* for (a) 5% suspension, 90% fill level, and (b) a 15% suspension, 95% fill level.

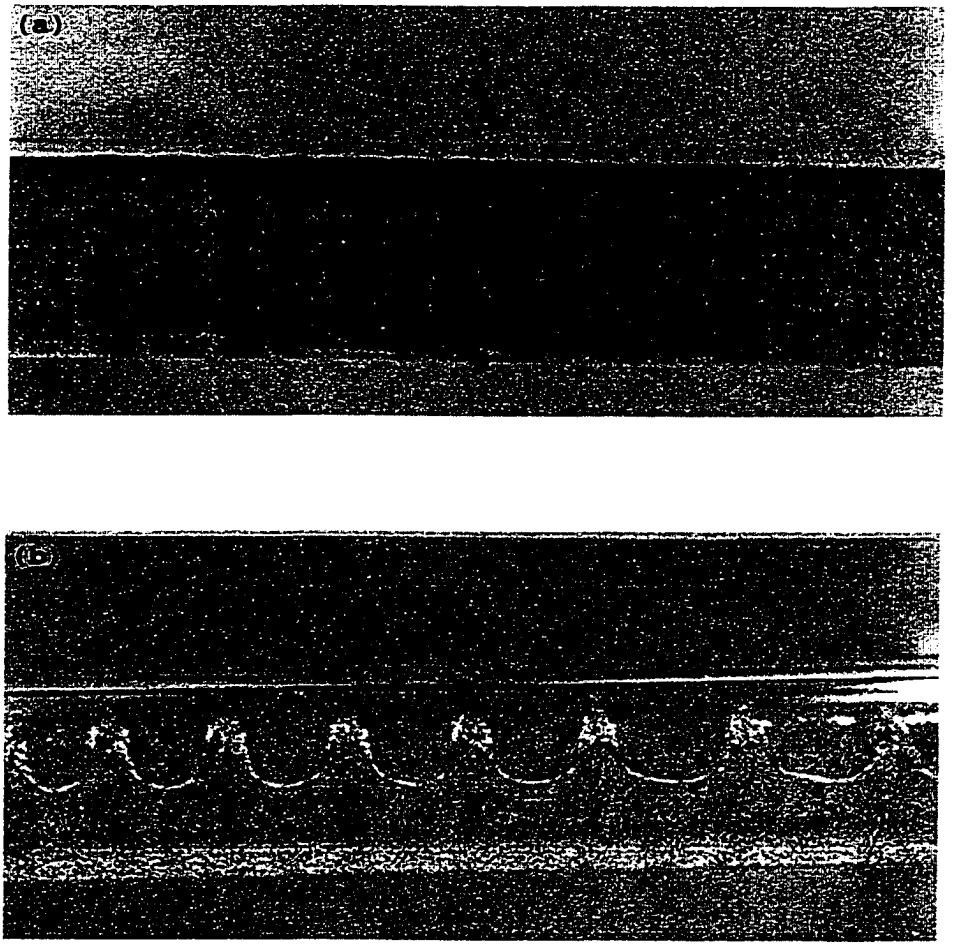

Figure 4.5: 15% suspension at (a) 95% fill level is sheared at 2.5 *rpm* and, (b) 50% fill level is sheared at 9.0 *rpm*. Compare these to 15% suspension at 95% fill level sheared at 9 *rpm*(figure4.4(b))

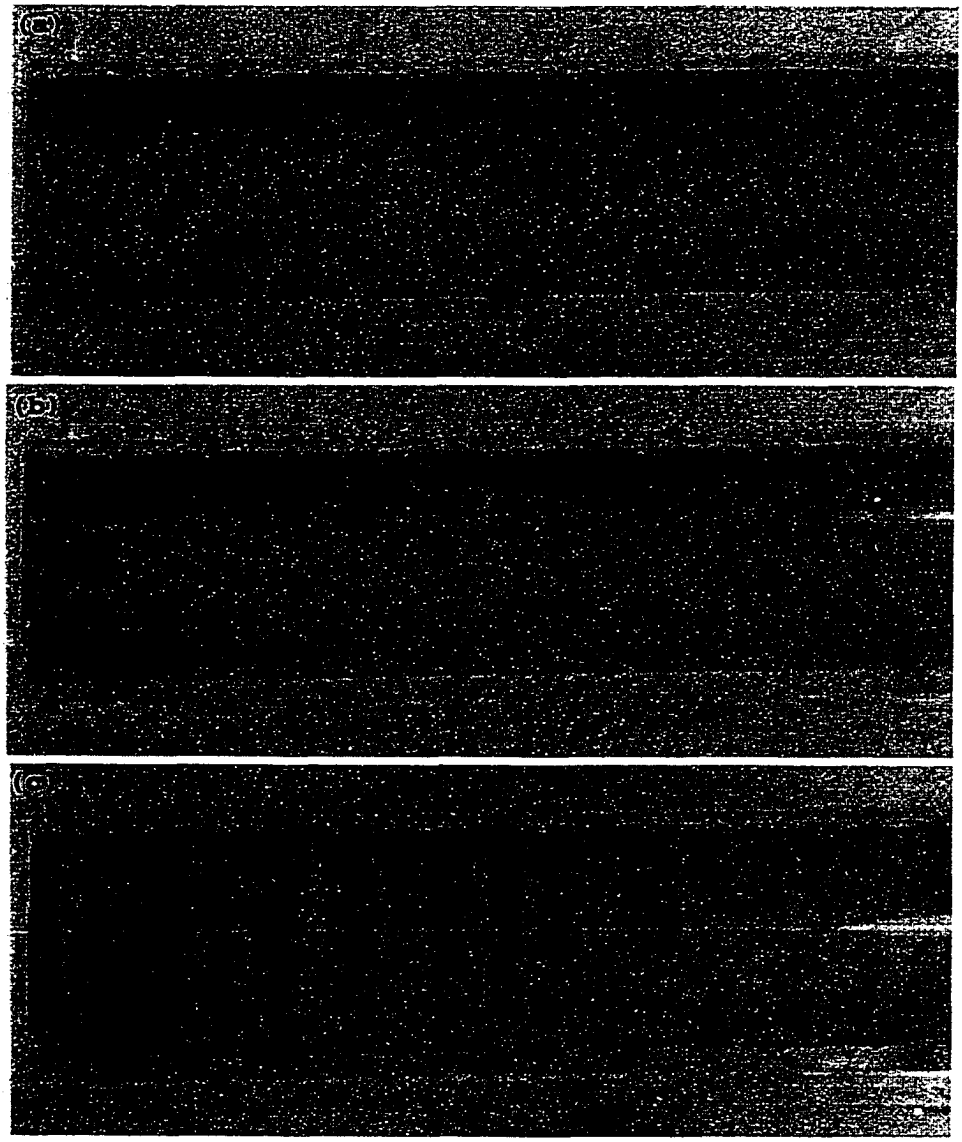

Figure 4.6: Segregation and time-dependent band formation for a 15% UCON suspension at a 95% fill level sheared at 9.3 *rpm* after (a) 5 min (b) 11 min (c) 29 min

Figure 4.7: The contact line viewed from the top of the Couette when a 15% UCON suspension at 95% fill level was sheared at 13 *rpm*.

Appendix A

Dimensionless numbers for the resuspension problem

Definition for the various dimensionless variables

Pressure: $$K = \frac{\Delta P}{l}\frac{R^4}{\mu_f Q}$$

Reynolds no., $$Re = \frac{Q\rho_f}{R\mu_f}$$

Froude no., $$Fr = \frac{Q\mu_f}{gR^4}\frac{1}{(\rho_p - \rho_f)}$$

Resuspension ht, $$H_{resp} = \frac{\tilde{y} - R}{R}$$

Maximum velocity, $$U_{max} = \frac{\tilde{U}_{max}R^2}{Q}$$

Axial velocity, $$u_3 = \frac{\tilde{u}_3 R^2}{Q}$$

Bibliography

[1] D. Leighton and A. Acrivos, "The shear-induced migration of particles in concentrated suspensions of spheres" J. Fluid Mech. **181**, 415 (1987)

[2] K. Zhang and A. Acrivos, "Viscous resuspension in fully developed laminar pipe flows," Int. J. Multiphase Flow **20**, 579 (1994)

[3] E.C. Eckstein, D.G. Bailey and A.H. Shapiro, "Self-diffusion of particles in shear flow of a suspension," J. Fluid Mech. **79**, 191 (1977)

[4] S.W. Sinton and A.W. Chow, "NMR flow imaging of fluids and solid suspension in Poiseuille flow," J. Rheol. **35**, 735 (1991)

[5] D. Leighton and A. Acrivos, "Viscous Resuspension," Chem. Eng. Sc. **41**, 1377 (1986)

[6] A. Acrivos, R. Mauri and X. Fan, "Shear-Induced resuspension in a Couette device," Int. J. Multiphase Flow **19**, 797 (1993)

[7] C.J. Koh, P. Hookman and L.G. Leal, "An experimental investigation of concentrated suspension flows in a rectangular channel," J. Fluid Mech. **266**, 1 (1994)

[8] U. Schaflinger, A. Acrivos and H. Stibi, "An experimental study of viscous resuspension in a pressure-driven plane channel flow," Int. J. Multiphase Flow **21**, 693 (1995)

[9] A. Nir and A. Acrivos, "Sedimentation and sediment flow on inclined surfaces," J. Fluid Mech. **212**, 139 (1990)

[10] R.J. Phillips, R.C. Armstrong, R.C. Brown, A.L. Graham and J.R. Abbot, "A constitutive equation for concentrated suspensions that accounts for shear-induced particle migration," Phys. Fluids. **A 4**, 30 (1992)

[11] P.R. Nott and J.F. Brady, "Pressure-driven flow of suspensions: simulation and theory," J. Fluid Mech. **275**, 157 (1994)

[12] S.A. Altobelli, R.C. Givler and E. Fukushima, "Velocity and concentration measurements of suspensions by Nuclear Magnetic Resonance Imaging," J. Rheol. **35**, 721 (1991)

[13] R.E. Hampton, A.A. Mammoli, A.L. Graham and N. Tetlow, "Migration of particles undergoing pressure-driven flow in a circular conduit," J. Rheol. **41**, 621 (1997)

[14] I.M. Kreiger, "Rheology of monodisperse lattices," Adv. Colloid Interface Sci. **3**, 111 (1972)

[15] D. Leighton and A. Acrivos, "Measurement of shear-induced self diffusion in concentrated suspensions of spheres" J. Fluid Mech. **177**, 109 (1987)

[16] U. Schaflinger, A. Acrivos and K. Zhang, "Viscous resuspension of a sediment within a laminar and stratified flow," Int. J. Multiphase Flow **16**, 567 (1990)

[17] A.N. Brooks and T.J.R. Hughes. "Streamline-upwind/Petrov-Galerkin formulations for convection dominated flows with particular emphasis on the incompressible Navier-Stokes equations," Comput. Meth. Appl. Mech. Engng **32**, 199 (1982)

[18] T.J.R. Hughes, M. Mallet and A. Mizukami, "A new finite element formulation for computational fluid dynamics: II. Beyond SUPG," Comput. Meth. Appl. Mech. Engng **54**, 341 (1986)

[19] A.J. Baker, *Finite Element Computational Fluid Mechanics*, Hemisphere, New York (1983)

[20] T.R.J. Hughes, W.K. Liu and A. Brooks, "Review of Finite Element Analysis of Incompressible Viscous Flows by the Penalty Function Formulation," J. Comp. Phys. **30**(1), 1 (1979)

[21] J.N. Reddy, *An Introduction to the Finite Element Method*, McGraw-Hill, New York (1984)

[22] H.P. Langtangen, *Computational Partial Differential Equations*, Springer-Verlag, Berlin (1999)

[23] S.R. Subia, M.S. Inger, L.A. Mondy, S.A. Altobelli and A.L. Graham, "Modelling of concentrated suspensions using a continuum constitutive equation," J. Fluid Mech. **193**, 193 (1998)

[24] M. Tirumkudulu and A. Acrivos, "Coating flows within a rotating horizontal cylinder: Lubrication analysis, numerical computations and experimental measurements," Phys. Fluids, Jan(2000).

[25] R.T. Balmer, "The Hydrocyst - a stability phenomenon in continuum mechanics," Nature **227**, 600 (1970)

[26] M.J. Karweit and S. Corrsin, "Observation of cellular patterns in a partly filled, horizontal, rotating cylinder," Phys Fluids **18**, 111 (1975)

[27] J. A. Deiber and R. L. Cerro, "Viscous Flow with a free surface inside a horizontal rotating drum. 1. Hydrodynamics," Ind. Eng. Chem., Fundam., **15**, 102 (1976)

[28] A. Aitta, "Nonlinear phenomenon at an air-fluid interface in a horizontal, rotating cylinder," Eur. J. Mech., B/Fluids, **10**, 175 (1991)

[29] T. B. Benjamin and S. K. Pathak, "Cellular flows of a viscous liquid that partly fills a horizontal rotating cylinder," J. Fluid Mech. **183**, 399 (1987)

[30] F. Melo, "Localized states in a film-dragging experiment," Physical Review E **48**, 2704 (1993)

[31] S. Thoroddsen and L. Mahadevan, "Experimental study of coating flows in partially-filled horizontal rotating cylinder," Exp. In Fluids **23**, 1(1997)

[32] T.B. Benjamin, W.G. Pritchard and S.J. Tavener, "Steady and unsteady flows of a highly viscous liquid inside a rotating horizontal cylinder," Preprint (1995)

[33] H.K. Moffatt, "Behaviour of a viscous film on the outer surface of a rotating cylinder," J. Mechanique **16**, 651 (1977).

[34] R.E. Johnson, "Steady-state coating flows inside a rotating horizontal cylinder," J. Fluid Mech. **190**, 321 (1988)

[35] S.B.G. O'Brien and E.G. Gath, "The location of a shock in rimming flow," Phys Fluids **10**, 1040 (1998)

[36] S. D. R. Wilson and J. Williams, "The flow of a liquid film on the inside of a rotating cylinder, and some related problems," Phys. Fluids **9**, 2184 (1997).

[37] A.E. Hosoi and L. Mahadevan, "Axial instability of a free-surface front in a partially filled horizontal rotating cylinder," Phys. Fluids **11**, 97 (1999)

[38] M. Tirumkudulu, A. Tripathi and A. Acrivos "Particle segregation in monodisperse sheared suspensions," Phys. Fluids **11**, 507 (1999). Corregendum *ibid* **11**, 1962 (1999)

[39] M. Tirumkudulu, A. Mileo and A. Acrivos "Particle segregation in monodisperse sheared suspensions in a partially filled rotating horizontal cylinder," Phys. Fluids **12**, 507 (2000).

[40] O.A.M. Boote and P.J. Thomas, "Effects of granular additives on transition boundaries between flow states of rimming flows," Phys. Fluids **11**, 2020(1999)

[41] S. S. Weidenbaum, "Mixing of Solids," *Advances in Chemical Engineering* (Edited by T. B. Drew and J. W. Hoopes), **2**, 211 (1952).